Near-Infrared Observations of Compact Binary Systems

by

Juthika Khargharia

M.S., University of Colorado, 2009

M.S., University of Kansas, 2006

B.Tech., NIT Calicut, 2002

A thesis submitted to the

Faculty of the Graduate School of the

University of Colorado in partial fulfillment

of the requirements for the degree of

Doctor of Philosophy

Department of Astrophysical and Planetary Sciences

2012

This thesis entitled:
Near-Infrared Observations of Compact Binary Systems
written by Juthika Khargharia
has been approved for the Department of Astrophysical and Planetary Sciences

Cynthia S. Froning

James C. Green

John T. Stocke

Thomas R. Ayres

Scott E. Palo

Date

The final copy of this thesis has been examined by the signatories, and we find that both the content and the form meet acceptable presentation standards of scholarly work in the above mentioned discipline.

Khargharia, Juthika (Ph.D. Astrophysical and Planetary Sciences)

Near-Infrared Observations of Compact Binary Systems

Thesis directed by Dr. Cynthia S. Froning

Low mass X-ray binaries (LMXBs) are a subset of compact binary systems in which a main-sequence or slightly evolved star fills its Roche lobe and donates mass to a neutron star or a black hole (BH) via an accretion disk. Robust estimates of compact object masses in these systems are required to enhance our current understanding of the physics of compact object formation, accretion disks and jets. Compact object masses are typically determined at near-infrared (NIR) wavelengths when the system is in quiescence and the donor star is the dominant source of flux. Previous studies have assumed that any non-stellar contribution at these wavelengths is minimal. However, this assumption is rarely true. By performing NIR spectroscopy, we determined the fractional donor star contribution to the NIR flux and the compact object masses in two LMXBs: V404 Cyg and Cen X-4. In our analysis, it was assumed that the light curve morphology remains consistent throughout quiescence. It has now been shown in several systems that veiling measurements from non-stellar sources are meaningful only if acquired contemporaneously with light curve measurements. We accounted for this in the measurement of the BH mass in the LMXB, XTE J1118+480. LMXBs are also considered to be the most likely candidates responsible for the formation of milli-second pulsars (MSP). Here, I present the unique case of PSR J1903+0327 that challenges this currently accepted theory of MSP formation and is a potential candidate for testing General Relativity. Observations in the NIR come with their own set of challenges. NIR detector arrays used in these observations generally have high dark current and readout noise. In an effort to lower the read noise in NICFPS at APO, we present a study done on the Hawaii–1RG engineering grade chip that served as a test bed for reducing the read noise in NICFPS.

To My Best Friend
and
My Family

Acknowledgements

I would like to express my sincere gratitude to my advisor and mentor Dr. Cynthia Froning. Under her guidance, I have learned many valuable skills that has helped me start, grow and evolve as a researcher. She is an excellent research advisor and I thank her immensely for all the effort she has put into my thesis work. Graduate school research started off on a rocky note but thanks to Dr. Jim Green, that I decided to pursue my Ph.D under the guidance of Dr. Cynthia Froning. I would like to thank him for funding me as a Research Assistant for the entire duration of my Ph.D. I am also thankful to Dr. John Stocke for giving me the opportunity to work on the newly discovered milli-seond pulsar PSR J1903+0327 and to Dr. Tom Ayres whose in-depth discussions on various topics related to stellar atmospheres have helped me in my work. I am thankful to the Gemini staff for their promptness in answering all the Gemini IRAF questions.

Being eight thousand miles away from home and not being able to visit as often makes pursing a Ph.D. a difficult journey. I cannot thank my parents and sisters enough for their unconditional love, sacrifices, never losing faith in me and always making sure I was eating enough food! I would like to thank my friends in Boulder for their enormous support during this time: Ting Yan and her family for their love, support and delicious food; Lisa Winter, for helping me professionally in uncountable ways; Martha Hosotani, for the trip to Hawaii.

Finally, and most importantly, many many thanks to my best friend Evan Guarnaccia. He has been an endless source of love, support, inspiration and countless laughs, both from near and far away. Thanks to him for checking on me everyday for the last seven years, always making sure, I had what I needed.

Contents

Chapter

Appendix

Tables

Table

Figures

Figure

Chapter 1

Introduction

1.1 Compact Binary Systems

Compact binary systems are stellar interacting binaries in which a main-sequence or a slightly evolved star transfers material to a compact object such as a black hole, neutron star or white dwarf. X-ray binaries are a subset of compact binaries wherein the primary star (the accreting object) is either a black hole or a neutron star, whereas cataclysmic variables (CVs) are binaries where the primary star is a white dwarf. X-ray binaries are further sub-divided into low mass X-ray binaries (LMXBs) and high mass X-ray binaries (HMXBs) based on the mass of the companion star and the mode of accretion. Typically, the companions in LMXBs have masses $\leq 1M_{\odot}$ and mass transfer takes place via Roche lobe overflow while HMXBs have companions with masses $\geq 10.0M_{\odot}$ and mass transfer takes place primarily via capture of stellar winds from the donor star. This thesis is focused on understanding the physical properties of LMXBs. To understand the structure and behavior of a LMXB, consider two stars orbiting each other due to their mutual gravitational pull. This system can be visualized in the co-rotating frame of the binary where the combined effect of the binary's rotation and gravity due to the two masses gives rise to the effective potential of the system (known as Roche potential) (Frank et al. 1992). Figure 1.1 shows cross-sections of equipotential surfaces for a binary system with mass ratio, q of 0.5 along with a three-dimensional view[1] ; mass–ratio refers to the ratio of the masses of the companion star to

[1] en.wikipedia.org/wiki/Roche_lobe

the primary star. The most interesting features in Figure 1.1 are the lobes connected by the dark solid line via the inner Lagrange point, L1. The L1 point connecting the two lobes is a point of unstable equilibrium where the combined forces of gravity due to the two component masses cancel out. The four other Lagrange points (L2, L3, L4 and L5) are more stable points where the combined forces due to gravity and the centrifugal acceleration are in balance. At these points, objects can orbit the binary in co-rotation. A star can fill its Roche lobe either due to expansion in size as it evolves off the main-sequence or due to shrinkage of the binary separation leading to removal of the outer layers of its envelope (Roche lobe overflow) by the gravitational pull of the other star through the L1 point. In three–dimensional space, the L1 point appears as a "pass" or a "saddle point" connecting the potential wells of the two stars.

Throughout this document, the accreting star will be referred to as the primary star and the mass-losing star will be referred to as the donor/companion star. Matter from the companion star forms an accretion disk around the primary star as it falls into the gravitational potential of the latter and slowly loses its initial angular momentum (Frank et al. 1992). The LMXBs studied within this thesis are transient systems that undergo occasional outbursts followed by long periods of quiescence lasting months to decades. Quiescence of an X-ray binary is identified by a power law dominated X-ray spectrum and low X-ray luminosity compared to the outburst value; during quiescence the X-ray luminosity is around $\sim 10^{30.5}$ – $10^{33.5}$ erg s^{-1} which is about 4–5 orders of magnitude lower than its outburst luminosity (van Paradijs and McClintock 1995).

1.2 Compact Object Masses in LMXBs : Why Do We Need Them?

The nature of the compact object in an LMXB can be determined from a measurement of its mass. An upper bound can be placed on the mass of a neutron star of $\sim 3.2 M_{\odot}$ based on the following assumptions: (i) the star is not rotating; (ii) the equation of state of a neutron star is known up to a density of 4.6×10^{14} g cm^{-3} and (iii) the speed of sound is smaller

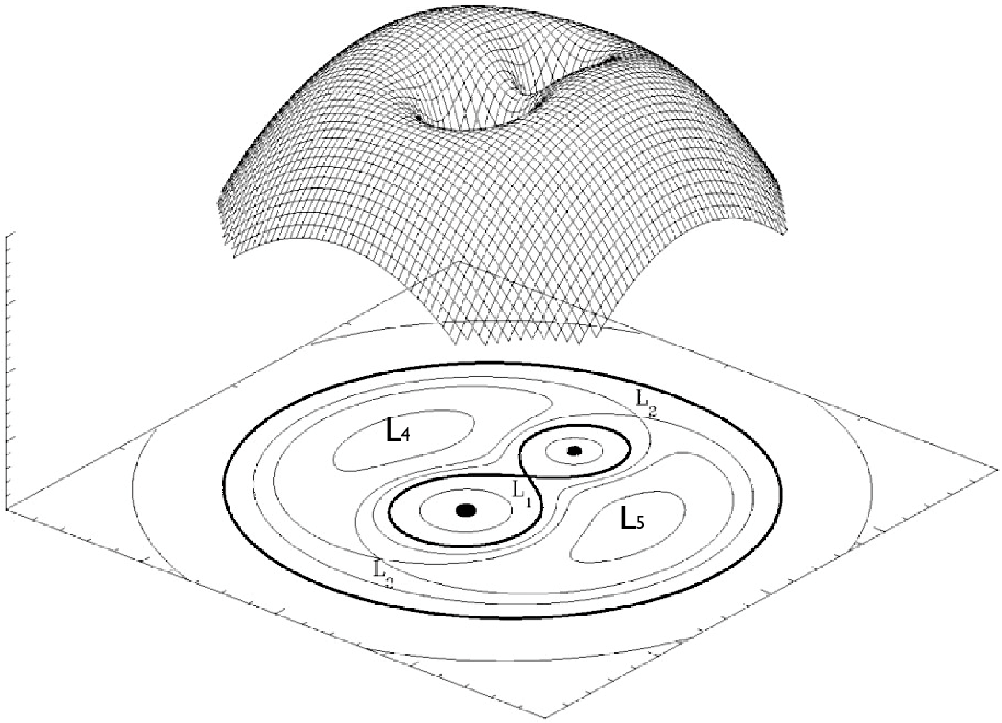

Figure 1.1: Contours of equipotentials in the orbital plane of a binary system calculated for a mass ratio of 0.5 supplemented with a three-dimensional view. The inner Lagrange point L1, formed at the intersection of the Roche lobes of both stars, represents a point of unstable equilibrium and is the gateway for transfer of material from one star to another. The Lagrangian points L2, L3, L4 and L5 are stable equilibrium points. (Source : `en.wikipedia.org/wiki/Roche_lobe`)

than c (Rhoades and Ruffini 1974). Considering rotation will serve to increase the mass of the neutron star by $< 20\%$ but this effect comes into play only if the neutron star is rotating close to break-up speeds (Friedman and Ipser 1987). A compact object mass beyond $3.2M_{\odot}$ is considered strong evidence for a black hole, whereas a mass below $3.2M_{\odot}$ but above 1.44 $M_{\odot}$ accompanied by Type I X-ray bursts are evidence for neutron stars (Psaltis 2006). Type I X-ray bursts are initiated by unstable thermonuclear burning of the accreted material on the neutron star surface and are, therefore, evidence of a solid surface rather than the event horizon of a black hole. Observationally, a Type I X-ray burst can be detected as a sharp rise (lasting ∼1–10 seconds) followed by a gradual and slow decline (lasting $\sim$ 10 s – several minutes) in the X-ray flux (Lewin et al. 1993). Determination of neutron star masses helps to constrain equations of state (EOS) of super dense matter. Different equations of state follow different tracks in the neutron star mass-radius plot. Thus any proposed EOS whose mass-radius track is unable to intersect the mass line of any neutron star can be ruled out. Generally, softer EOS are characterized by a flatter/softer profile beyond a certain nuclear density. For example, radio observations of the binary milli-second pulsar PSR J1614 – 2230 have yielded the most massive neutron star to date ($1.97 \pm .04 M_{\odot}$), thereby ruling out certain softer EOS that predict "exotic" components such as hyperons, bosons and free quarks at nuclear saturation densities in their models (Demorest et al. 2010).

Accurate masses are required to test models of the origin of compact objects in close binaries. While theoretical models of supernova explosions and binary evolution predict a continuous distribution of compact object masses from neutron star masses up to $10 - 15 M_{\odot}$, there appears to be a statistically significant dearth of black holes at the lower end of the mass spectrum between 2 – 4.5 $M_{\odot}$ (Farr et al. 2011; Özel et al. 2010). Belczynski et al. (2011) attempted to explain the physical processes involved in the supernova explosion that account for the presence of the mass gap in the observed compact object mass distribution. In their models, they invoke two different kinds of instabilities to trigger the supernova explosion. These two instabilities are characterized broadly by their growth timescales and

can generate different mass distributions of the compact remnants. Specifically, they found that an explosive mechanism driven by Rayleigh-Taylor instabilities within the first ∼100–200 milliseconds of the initial stellar collapse can produce the observed compact object mass gap. Black hole evaporation predicted by multi-dimensional gravity models provide another possible explanation for the absence of lower mass black holes. In these models, the rate of evaporation is inversely proportional to the mass of the black holes, thereby possibly creating a dearth of low mass black holes (Postnov and Cherepashchuk 2003).

However, other questions need to be addressed. Does the gap represent an observational bias that prevents us from detecting the smaller black holes? How accurate are the previously measured black hole masses? To answer the first question, let's consider an example of an observational bias: black hole mass measurements are performed when the system is in quiescence and the donor star can be observed. However, systems with smaller mass black holes will have mass ratios closer to unity (companion masses in LMXBs are typically $\leq 1.0 M_{\odot}$) resulting in steady mass transfer and no quiescent state; this will prevent black hole mass determination in these systems (Fryer and Kalogera 2001). However, the same is not true for the wind-fed HMXB systems (companion masses in HMXBs are typically $> 10 M_{\odot}$) and this bias should not prevent us from measuring masses of the smaller black holes in these systems (Belczynski et al. 2011). Thus, the existence of this observational bias is still debatable. The second question – how accurate are the previously measured masses – leads us to a re-evaluation of previously measured masses and what, if any, corrections are required for these already estimated masses. This question is explored in more detail in Section 1.4.

Accurate and unbiased compact object masses are required in other areas as well. Both supermassive and stellar mass accreting black hole systems have been commonly observed to power relativistic jets (Mirabel and Rodríguez 1999; Zensus 1997). Synchrotron emission from these jets is typically observed in the radio and infrared wavelength bands. However, the process by which these jets are launched is not well understood. One of the popular

theories behind the jet mechanism comes from Blandford and Znajek (1977), who proposed that an accreting and rotating black hole could twist magnetic fields in its vicinity, resulting in transfer of energy from the black hole into an electromagnetically-powered jet. Recently, attempts have been made to measure the spins of black holes in several systems containing stellar mass black holes (e.g Shafee et al. 2006, Steiner et al. 2009) and to investigate further the role of spin in powering jets in these systems (Fender et al. 2010; Narayan and McClintock 2012). Black holes can either acquire spin at birth (natal spin) and/or due to mass accretion from their companion. The two parameters, black hole spin and BH mass, completely characterize a black hole. However, black hole spin estimates need accurate estimates of black hole mass which is obtained independently from optical/infrared observations of these systems in quiescence, thereby requiring us to have reliable black hole mass estimates in hand.

It has also been suggested that if jets are launched in the innermost parts of the accretion disk, then the physics of jets could be tied to the accretion flow (Falcke and Biermann 1995). Radio and X-ray observations probe the jet and innermost regions of the accretion disk respectively. These observations, coupled with independently determined central black hole masses, have revealed a "Fundamental Plane" of black hole activity in which the X-ray luminosity, radio luminosity and black hole masses are correlated both for Galactic BHs and their supermassive counterparts (Merloni et al. 2003). The Fundamental Plane of black hole activity allows an understanding of accretion physics across the entire black hole mass range, spanning over nine orders of magnitude (from X-ray binaries to AGNs), by a mere scaling of the corresponding black hole mass (e.g. Done and Gierliński 2005). Thus, if we know the black hole mass in X-ray binaries, we can scale the other properties to study their supermassive analogs, taking advantage of the shorter timescale of variability in the former systems to probe physical properties. For example, it was shown by Markoff et al. (2012) that the same physical model with system parameters scaled only by the corresponding black hole mass can be used to model the SED of the LMXB A0620-00

as well as the supermassive BH, Sgr A*.

Additionally, compact remnants in LMXBs have been used to infer the stellar initial mass function (IMF) in ultra compact dwarf galaxies (UCDs) (Dabringhausen et al. 2012). As a potential explanation for the high mass-to-light ratios observed in UCDs, these authors have suggested that the stellar initial mass function in these systems could be skewed towards the high mass stars; the neutron stars and black holes in LMXBs could be used to account for the unseen mass in these systems.

In the next sections, I will discuss how masses of compact objects in LMXBs are currently measured and why previously estimated compact object masses should be re-examined.

1.3 Technique of Mass Measurement in LMXBs

Observations of LMXBs during quiescence are used to determine masses of the compact objects in these systems. During this time, the companion star becomes the dominant source of flux in the optical/NIR and the system can be studied to determine key system properties like the spectral type of the companion, the binary period, the radial velocity, and the rotational velocity of the companion. Using Kepler's laws, the minimum mass of the compact object, known as the mass function $f(M)$, can be obtained (Frank et al. 1992):

$$f(M) = \frac{PK^3}{2\pi G} = \frac{M_X \sin^3 i}{(1+q)^2} \tag{1.1}$$

P = binary orbital period.

K = radial velocity amplitude of the donor.

M_X = mass of the compact object.

i = binary inclination (angle between the plane of the binary and plane of the sky).

$q = M_2/M_X$ (mass ratio) ; M_2 is the mass of the donor star.

$$M_X = \frac{(1+q)^2}{\sin^3 i} f(M) \tag{1.2}$$

From Equation (1.1), we find that the mass function can be directly determined from the binary orbital period and the radial velocity curve. It also represents a strict lower limit on the mass of the compact object. From Equation (1.2), $M_X > f(M)$ follows directly from the fact that $\sin^3 i \leq 1$ and $(1+q) > 1$. Once the value of $f(M)$ is obtained, the actual mass of the compact object can be determined if we know the mass-ratio, q, and the binary inclination, i. By assuming that the companion has filled its Roche-lobe and is tidally locked with the primary, the approximate formula given in the form of Equation (1.3) below can be used to determine the mass-ratio of the binary (Gies and Bolton 1986; Wade and Horne 1988) via the companion's projected rotational velocity, $v_{rot} \sin i$. The rotational velocity information is embedded in the absorption features of the companion star's atmosphere and can be calculated by measuring the line broadening in these features.

$$v_{rot} \sin i = K \times 0.462 \; q^{1/3} (1+q)^{2/3} \tag{1.3}$$

The only unknown that remains to be determined towards obtaining the mass of the compact object is the binary inclination, i (from Equation (1.2)). This is determined by modeling the ellipsoidal variations of the donor star in quiescence. The emergent flux from the tidally–distorted Roche lobe-filling donor star depends on the combined effects of its projected surface area as well as the effects of limb darkening and gravity darkening. This is illustrated in Figure 1.2. Limb darkening arises naturally due to the non-uniform brightness of the projected disk of the star as we move from the center to the limb of the disk. The more subtle effect of gravity darkening arises due to the fact that the flux from a non-spherical star is proportional to the local surface gravity with lower flux arising from regions of lower surface gravity (von Zeipel 1924).

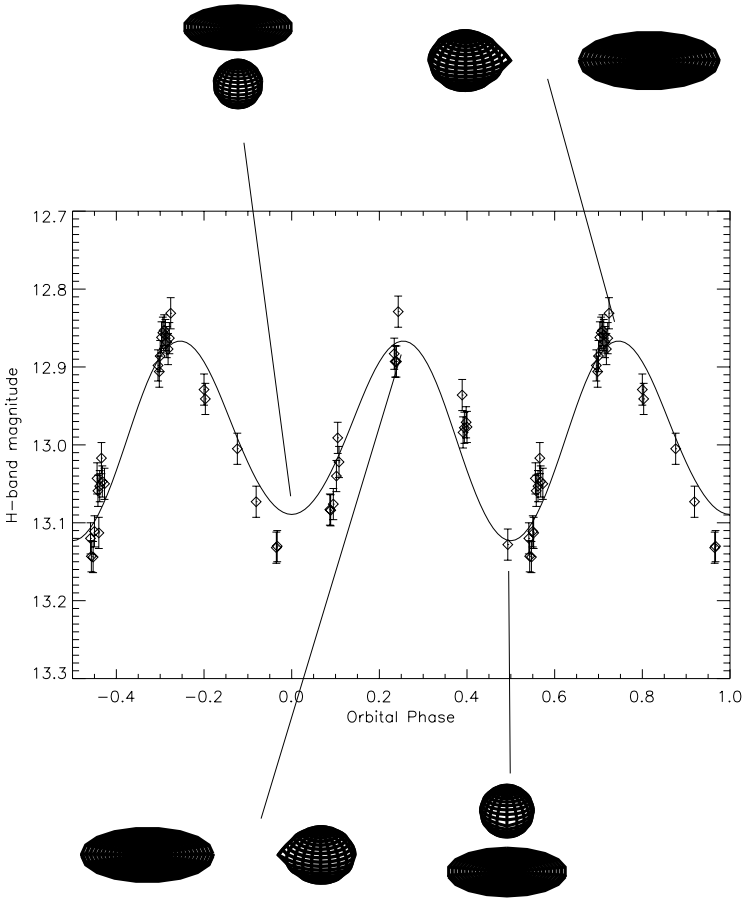

Figure 1.2: Ellipsoidal modulation of the donor star in V404 Cyg. The near-sinusoidal variation in the light curve is caused by variations in the projected surface area, limb darkening and gravity darkening of the donor star. The projected surface areas are the largest at ϕ=0.25 and 0.75 and smallest at ϕ=0.0 and 0.5 which explains the positions of maxima and minima. The unequal minima is due to the effect of gravity darkening. The system orientation at various phases are plotted for the parameters corresponding to V404 Cyg using the light curve code "XRbinary" written by E.L. Robinson. Source: (Khargharia et al. 2010)

The donor star light curve will take on a near-sinusoidal shape with maximum flux occurring at quadrature (at orbital phases, $\phi = 0.25$ and $\phi = 0.75$) and minimum occurring at conjunction (at orbital phases, $\phi = 0.0$ and $\phi = 0.5$) based dominantly on the projected surface area. However, the minimum at $\phi = 0.5$ will be deeper than that at $\phi = 0.0$ owing to lower surface gravity at the tear drop tip of the Roche lobe filling donor star at $\phi = 0.5$. The amplitude of the ellipsoidal variations is most sensitive to the binary inclination with a weaker dependence on the mass-ratio. The mass-ratio is typically fixed from observations of the rotational velocity of the donor star as seen from Equation (1.3). Thus by modeling the light curves of the donor star, we can determine the binary inclination – the last remaining unknown towards computation of the compact object mass.

1.4 Precise Mass Estimates of Compact Objects

Modeling the observed light curves in LMXBs based on pure ellipsoidal models is not always straightforward. For example, the black hole binary A0620-00 has been studied extensively over the past twenty years and its light curve has been shown to vary from time to time (McClintock and Remillard 1986; Haswell et al. 1993; Gelino et al. 2001; Froning and Robinson 2001; Cantrell et al. 2008). Various models have been incorporated to explain the observed asymmetry in the light curve which include: star spots on the donor star, disk asymmetries, grazing eclipses, the bright spot on the accretion disk produced by the mass transfer stream impacting the disk, and state changes during quiescence. In addition, a light curve may also be affected by other non-variable sources (for example, the accretion disk) that will contribute a constant flux to the total observed near-infrared flux. Light curves are often acquired at near-infrared (NIR) wavelengths where the donor star dominates the total observed flux and other non-stellar sources of flux are assumed to be negligible, although this assumption is rarely true (Reynolds et al. 2008; Cantrell et al. 2008, 2010). A consequence of this assumption is that flux sources that have hitherto been ignored will dilute the observed light curve reducing the amplitude of ellipsoidal modulation, thereby

underestimating the binary inclination and in turn, overestimating the mass of the compact object. My collaborators and I have undertaken a study to account for the non-stellar sources of light at NIR wavelengths and to obtain precise and unbiased masses of the compact objects in LMXBs. Other sources of light at these wavelengths can be properly accounted for by measuring the dilution of the absorption features in the donor star spectrum (also called veiling) by comparing these features to field stars of known spectral types. However, the donor fraction estimate is sensitive to temperature mismatches between the template star and the LMXB, and should be correctly determined (Hynes et al. 2005). Once the spectral type of the donor has been determined, the amount of scaling (f; where $f \leq 1$) by which we must adjust the the spectrum of the known spectral type to match that of the LMXB spectrum gives the fractional contribution of the donor star to the total NIR flux. In Chapters 2 and 3 we have included the contribution from other non-stellar sources from spectroscopy and correctly modeled previously obtained light curves to determine precise masses of the compact object in two LMXBs, V404 Cyg and Cen X-4. The content of these two chapters have been published in the Astrophysical Journal, Volume 716, Issue 2, pp. 1105-1117 (2010) by Khargharia, J., Froning, C.S., & Robinson, E.L. However, the compact object masses obtained in this manner must still be viewed with some caution. Through a comprehensive study of the light curves of the quiescent LMXB A0620–00 over a period of eight years, Cantrell et al. (2008, 2010) have shown that even during quiescence, this black hole binary system displayed state changes characterized by magnitude, color and aperiodic variability. These authors have shown that veiling measurements are truly meaningful only if acquired contemporaneously with light curve measurements. With this motivation, we studied the quiescent black hole LMXB, XTE J1118+480, by obtaining contemporaneous light curve and spectral data to determine a robust mass of its black hole, presented in Chapter 4.

1.5 Evolution of LMXBs : Formation of Milli-Second Pulsars

In this section, I will present a qualitative picture of the evolution of LMXBs (containing neutron stars as the compact accretors) leading up to the formation of milli-second pulsars. This section is derived from the work done by Lorimer (2001); Hynes (1999); Bhattacharya (1995); Verbunt and van den Heuvel (1995).

Milli-second pulsars (MSP) are characterized by their low spin periods (1.5 ms $< P_{spin} <$ 30 ms) and weak magnetic fields ($B \sim 10^8 G$). A large fraction ($\sim$ 80%) of them are members of binary systems. They are seen to orbit low mass companions ($< 0.7 M_\odot$; generally white dwarfs) in almost circular orbits (eccentricity, $e < .001$) and until the discovery of the MSP binary PSR J1903+0327 in 2008, all known Galactic disk MSPs adhered to this picture. On the other hand, MSPs with high mass companions ($> 1 M_\odot$; including high mass white dwarfs, main-sequence stars or other neutron stars as donors) are seen to exist in globular clusters in more eccentric orbits (Lorimer 2001). The high eccentricity for globular cluster MSPs can be explained by considering frequent close encounters of these systems with other stars, thereby disturbing the original circular orbits. Also, the fraction of MSP binaries in globular clusters is smaller than that in the Galactic disk by $\sim$ 50%. MSPs are believed to have acquired their short spin periods via an extended period of accretion from their companion. The duration of mass transfer in HMXBs is much smaller than in LMXBs, making it unlikely for the massive companion to spin up the neutron star to milli-second speeds during that period. The most likely explanation for the origin of MSPs therefore comes from considering the evolution of LMXBs in which the companion star is $< 1 M_\odot$(Bhattacharya 1995). The presence of almost circular orbits, milli-second spin periods, and low mass companions in MSP binaries makes LMXBs the most likely candidates for providing the conditions necessary for their formation. For example, the binary millisecond pulsar PSR J1614–2230 contains a 1.97 $M_\odot$ neutron star around a 0.5 $M_\odot$ white dwarf companion and is considered to be a more evolved version of the LMXB Cyg X-3 (Lin et al.

2011).

An illustration of the various evolutionary paths leading up to the formation of MSPs can be understood from Figure 1.3 via the example of the MSP, PSR J1855+09 (Tauris and van den Heuvel 2006). Starting with a binary system with vastly different component masses, the more massive of the two stars will evolve first and fill its Roche lobe. Soon after the initiation of mass flow the less massive companion will be engulfed in the giant's envelope. At this time, the binary separation will dictate the next set of events to follow. For the formation of an LMXB, the binary is required to be wide enough that the low mass companion spirals in to the giant's core and the more massive companion undergoes a supernova explosion before a complete merger occurs. At the same time, the core of the giant will continue evolving until it explodes in a supernova. The binary will survive the supernova explosion if the total mass lost in the supernova is less than half of the pre-supernova mass, assuming an asymmetric explosion. In the case of neutron star binaries, spin down of the neutron star to a period of $\geq$ several seconds will occur 10^{7-8} years following the supernova explosion, and can be observed as a normal radio pulsar.

The low mass companion will then be left orbiting the neutron star in an eccentric orbit. However, tidal interactions will circularize the orbit and also tidally lock the low mass companion with the binary. Meanwhile, the evolution of the low mass companion will continue and as it evolves away from the main-sequence, it will fill its Roche lobe. Mass transfer will then ensue via an accretion disk onto the neutron star and will result in widening of the binary orbit. Mass accretion over a prolonged period of time will spin up the pulsar to milli-second periods (the term "recycled pulsars" are often used to describe MSPs). However, once the degenerate core is all that is left behind of the initial low mass companion, the binary will detach and mass transfer will stop. The final result is that of a white dwarf orbiting around a milli-second pulsar in an almost circular orbit.

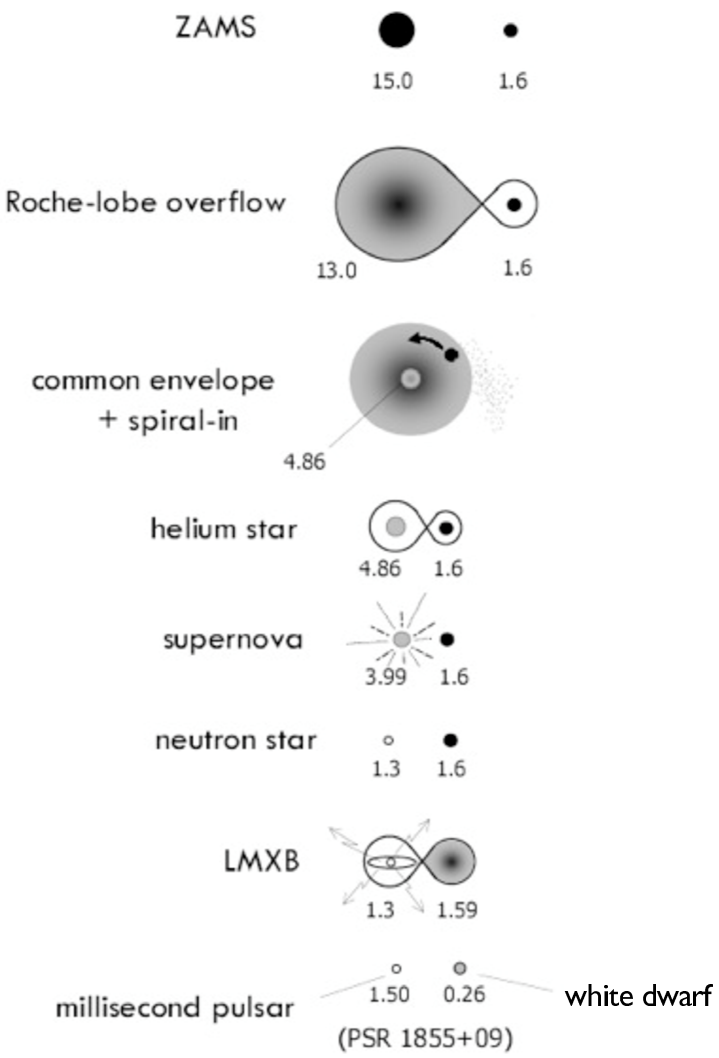

Figure 1.3: Figure showing various evolutionary paths of a binary system leading up to the formation of MSPs. The masses of the individual components have been chosen to depict the specific case of formation of the MSP PSR J1859+09 with individual component masses below each stage of evolution. Binary MSPs have been theorized to evolve from LMXBs owing to their low spin periods and almost circular orbits. However, the discovery of the MSP binary PSR J1903+0327 has led one to revisit the currently accepted theory of MSP formation. Source: (Tauris and van den Heuvel 2006)

1.6 Do all Galactic MSPs originate from LMXBs?

Most MSPs found in the disk of our Galaxy are seen to exist around white dwarf companions with all of them in perfectly circular orbits, thereby confirming the formation theory of MSPs from LMXBs as discussed in the previous section. However, the discovery of the MSP binary PSR J1903+0327 forces one to question the currently accepted theory of MSP formation (Champion et al. 2008). This 2.15 ms pulsar was discovered in the Arecibo L-band Feed Array (ALFA) Galactic plane pulsar survey. Follow-up timing observations obtained with the Greenbank Telescope, Arecibo, and the Westerbork Synthesis Radio Telescope showed that the pulsar was in a highly eccentric orbit ($e = 0.44$) with a 95 day orbital period. Such high eccentricities are not expected based on the currently observed sample of Galactic MSPs. Figure 1.4 shows the unique position occupied by PSR J1903+0327 when compared to the existing sample of MSPs in the Galactic plane. Infrared observations of the pulsar field further revealed a main-sequence star at the position of the pulsar making it a likely companion to the MSP and suggesting that the MSP is part of a primordial hierarchical triple, where a white dwarf orbits the MSP in a 95-day period and the main-sequence star is in a much wider orbit around the MSP-WD binary. However, in the discovery paper by Champion et al. (2008), it was not known with certainty whether the main-sequence star was the actual companion to the MSP. The focus of Chapter 5 is therefore based on a study undertaken to determine the nature of the companion to the MSP that will further enhance our understanding of the theory of MSP formation. The content of this chapter has been published in the The Astrophysical Journal, Volume 744, Issue 2, article id. 183 (2012) by Khargharia, J., Stocke, J.S., Froning, C.S., Gopakumar, A., & Joshi, B.C.

Additionally, by constraining the rotational velocity of the companion to the MSP this system can be potentially be used for testing General Relativity theory. Most binary pulsar systems can be timed using Kepler's laws governing the dynamics of binary systems. These observable Keplerian parameters are the projected semi-major axis a, the longitude

of periastron ω, the time of periastron passage T_0, the orbital period P_b, and the orbital eccentricity e. However, in relativistic binaries, five more parameters known as Post-Keplerian (PK) parameters can be measured, which include: the rate of periastron advance $\dot{\omega}$, orbital period decay $\dot{P}_b$, time dilation and gravitational redshift parameter γ and the Shapiro delay parameters r and s (Lorimer 2001). In General Relativity, each of the five PK parameters are functions of the orbital period, the masses of the components (i.e the pulsar and the companion masses), and the five Keplerian parameters (which can be measured). As the stellar masses are the only unknowns in the equations describing the binary, a measurement of any two of the five PK parameters will lead to precise measurement of the component masses. A measurement of more than two PK parameters gives an over-determined system allowing one to do self-consistency tests of General Relativity. For example, in the double neutron star system J0737–3039, all five PK parameters have been measured allowing a test of General Relativity at the 0.05% accuracy level (Kramer et al. 2006). In Chapter 5, we will discuss whether PSR J1903+0327 can be used as a system for testing General Relativity theory.

1.7 Near-Infrared Observations in Astronomy: Advantages and Challenges.

Near-infrared observations of compact binary systems in astronomy date back to the late 1970's and early 1980's (Szkody 1977). Since then NIR astronomy has advanced in detection capabilities by leaps and bounds, leading to tremendous growth of observations in this wavelength regime. The NIR waveband typically constitutes the wavelength range from 1–5 μm. Observations at NIR wavelengths are ideal for studying the cool (T_{eff} = 4300 – 4700 K) donor star in LMXBs from which accurate spectral types can be established. Most donor stars in LMXBs are either dwarfs or slightly evolved stars falling in the spectral range K-M and their NIR spectra are rich in many atomic and molecular transitions. The NIR light curves of LMXBs can be fitted with models of ellipsoidal modulations of the Roche lobe filling donor star to get the binary inclination. Thus, NIR spectroscopy along with NIR

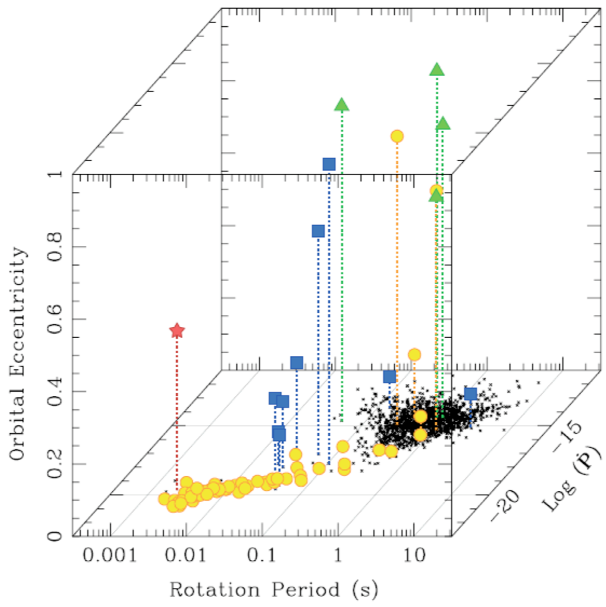

Figure 1.4: The bottom face of the cube shows period vs. period derivative distribution for the observed sample of normal and milli-second pulsars in the Galactic disk. Yellow circles represent white dwarfs, blue squares represent neutron stars and green triangles represent main-sequence stars as companions to the pulsar. Black dots are isolated neutron stars. Galactic disk MSPs are always found around white dwarfs in perfectly circular orbits. PSR J1903+0327 (in red) falls within the description of typical MSPs when looking only at the $P - \dot{P}$ distribution. When eccentricity is also taken into account, PSR J1903+0327 occupies a unique place in the diagram. Source: (Champion et al. 2008)

light curves are used to obtain precise mass estimates of the compact objects in LMXBs. Moreover, many heavily reddened systems that are opaque at optical wavelengths can be best explored at NIR wavelengths.

NIR observations come with their own set of challenges. Water vapor and carbon dioxide in the Earth's atmosphere absorb infrared radiation at certain wavelength intervals, between which the atmosphere is more transparent. For the majority of the work produced in this thesis, observations were acquired in the J-, H- and K-passbands, with central wavelengths of 1.25μm, 1.65μm and 2.2μm respectively. In addition, night sky emission ("airglow") makes observing challenging at NIR wavelengths. The most dominant contributor to "airglow" is from the hydroxyl (OH) molecule which emits strongly in the 1–2.5 μm wavelength range. At wavelengths $> 2.5\mu$m, another source of noise is thermal emission originating in the warm telescope and optics (McLean 1993).

The advent of IR detector arrays has greatly accelerated the pace of infrared research. IR array construction is based on a "hybrid" structure where the infrared photosensitive component is physically distinct from the multiplexer that relays the resultant electric signal from the pixels to the readout electronics. IR arrays can usually be read out non-destructively in such a way that the charge in each pixel may be read without removing it. Also, when a certain pixel is read, the neighboring pixel remains undisturbed, allowing multiple reads to take place. Due to the high background at NIR wavelengths, the array readout time is required to be fast in IR arrays to avoid saturation of the wells, and therefore shorter exposures are required. Although IR arrays have made rapid improvements, they generally have higher dark current and readout noise than CCDs. Dark current refers to the illumination of the array in the absence of photons caused by thermal generation of electrons in the semiconductor material and is sensitive to the time of the exposure. Shorter exposures and a cryogenically-cooled detector will greatly reduce the dark noise contribution. Readout noise is produced in IR arrays every time the array is read out and this noise is generated in the readout electronics. Read noise is a constant and is independent of the exposure time. The

process of Fowler sampling which incorporates multiple non-destructive reads in IR arrays is often employed to reduce the read noise (Fowler and Gatley 1990). This is explained in more detail in Chapter 6.

In Chapter 6, I will describe the work done at the Astrophysics Research Lab in the University of Colorado under the guidance of Stéphane Béland to characterize a Hawaii–1RG (**H**gCdTe **A**stronomy **W**ide **A**rea **I**nfrared **I**mager with **1**K × 1K resolution, **R**eference pixels and **G**uide mode) engineering grade chip. Several tests were performed on this detector to develop ways to identify the source, and to reduce the contribution of, the read noise component to NIR observations. The results of these tests were intended to be applied towards reducing the read noise in the Near-Infrared Camera and Fabry-Perot Spectrometer (NICFPS) at Apache Point Observatory (APO). The focus of Chapter 6 is to present the various tests that were performed to characterize the H1RG Engineering Grade chip.

Chapter 2

Mass of the Black Hole in V404 Cyg

2.1 Introduction

V404 Cyg went into outburst on May 22, 1989 and was subsequently discovered with the all-sky monitor aboard the Ginga satellite. A high X-ray luminosity of $\approx 10^{38}$ ergs/sec suggested that the system was a close binary system with a black hole or a neutron star as the accretor (Wagner et al. 1989). During the outburst, the visual magnitude of V404 Cyg increased from V=18.3 to V=11.6. One year after its discovery, it had fallen back to V=18.0 (Wagner et al. 1992). Since then, V404 Cyg has been studied in quiescence at optical and infrared wavelengths, establishing most of the system parameters. Casares et al. (1992) established the mass function, the minimum mass of the compact object, as $f(M) = 6.26 \pm 0.31 M_{\odot}$ which was later refined by Casares and Charles (1994) to be $f(M) = 6.08 \pm 0.06 M_{\odot}$. They determined the donor star to be of spectral type K0IV and obtained the binary mass ratio from the rotational broadening of the absorption lines in the donor star spectrum. The ellipsoidal modulation of the donor star has been modeled in the NIR to determine the binary inclination and the black hole mass: in the K-band by Shahbaz et al. (1994) and in H by Sanwal et al. (1996). The resulting black hole mass determinations were 12 $M_{\odot}$ and $<$12.5 $M_{\odot}$, respectively, where one of the key differences between their results was that Shahbaz et al. (1994) assumed that the donor star was the only source of flux in the NIR, while Sanwal et al. (1996) found evidence for accretion disk contamination. Shahbaz et al. (1996) tested this assumption by performing NIR spectroscopy of V404 Cyg. By

comparing the NIR spectrum to scaled template spectra from spectral type standard stars, they determined that the donor star contributes ∼100 % of the K-band flux. However, for this analysis they relied on fits to the ^{12}CO bands in K, which in other LMXBs (and cataclysmic variables) have been found to be affected by metallicity variations in the carbon abundance (Froning et al. 2007). As a result, a broader spectral analysis that examines multiple atomic and molecular species is required to firmly tie down the donor star contribution in the NIR.

Here, we present broadband (0.8–2.42 μm) NIR spectroscopy of V404 Cyg obtained with SpeX on the IRTF. By comparing the spectra to field stars of known spectral type, we determine the donor star contribution to the infrared flux. We use these results to remodel previously obtained light curve data to determine the binary inclinations and to derive precise compact star mass for the black hole.

2.2 Observations

V404 Cyg was observed on June 7–9, 2007 with SpeX at the NASA Infrared Telescope Facility (Rayner et al. 2003). The weather was clear with good seeing conditions ($\leq 0.7''$). All observations were made using the Short XD (SXD) mode through the $0.5''$ slit (R=1200), which covers the entire wavelength range, 0.8–2.4μm, simultaneously in 6 orders. Due to the good seeing conditions and the narrow slit used, the observed spectrum was uncontaminated by an accidental companion star at $1.5''$ from V404 Cyg. An A0V star was observed hourly for the purpose of telluric correction. Observations were taken in ABBA pairs in two positions along the slit with a 300 sec exposure time at each position. The slit was oriented along the parallactic angle throughout the observations, limiting the relative flux calibration uncertainties to $< 2\%$ (Vacca et al. 2003). Table 2.1 lists the observations with the corresponding cumulative exposure times and orbital phases observed.

Data reduction consisted of calibration (sky subtraction, flat-fielding, wavelength calibration), optimal spectral extraction, and telluric correction, all of which were carried out using the idl based package Spextool (Cushing et al. 2004). Each exposure was shifted to the

Table 2.1: Table of Observations

Date	Exposure time(min)	Orbital Phase
06/07/07	100	0.59-0.61
06/08/07	190	0.74-0.76
06/09/07	150	0.89-0.91

rest frame of the donor star, using the orbital ephemeris from Casares and Charles (1994). The individual shifted exposures were median-combined and all 6 orders were merged to obtain the time-averaged spectrum. Using the magnitudes of the A0V star, the telluric correction tool, xtellcor, also flux calibrates the spectra. Given our excellent observing conditions, the absolute fluxes should be fairly accurate, although no attempt has been made to quantify the accuracy of those values, as they are not necessary for this analysis.

Figure 2.1 shows the time-averaged spectrum of V404 Cyg. The spectrum has been boxcar smoothed by 3 pixels, corresponding to one resolution element. Statistical errors were propagated through all the data reduction and processing steps. The spectrum was corrected for interstellar reddening using a dereddening value of E(B-V)= 1.303 (Hynes et al. 2009; Miller-Jones et al. 2009). The spectrum in red in Figure 2.1 is the dereddened spectrum of V404 Cyg. Shown in Figures 2.2, 2.3 and 2.4 are the J-, H-, and K-band spectra. The prominent spectral features have been labeled using line identifications from Wallace and Hinkle (1997), Wallace et al. (2000), Kleinmann and Hall (1986), Meyer et al. (1998), Kirkpatrick et al. (1993), and the Atomic line list[1] . The S/N in the time-averaged spectra of V404 Cyg was obtained by fitting straight lines through various continuum-dominated regions and measuring the scatter around these fits. As the donor in V404 Cyg is likely a giant or sub-giant, there are fewer regions of pure continuum. Therefore, a lower limit to the S/N of ≈ 100 in H and K, and ≈ 50 in J was obtained.

[1] http://www.pa.uky.edu/ peter/atomic

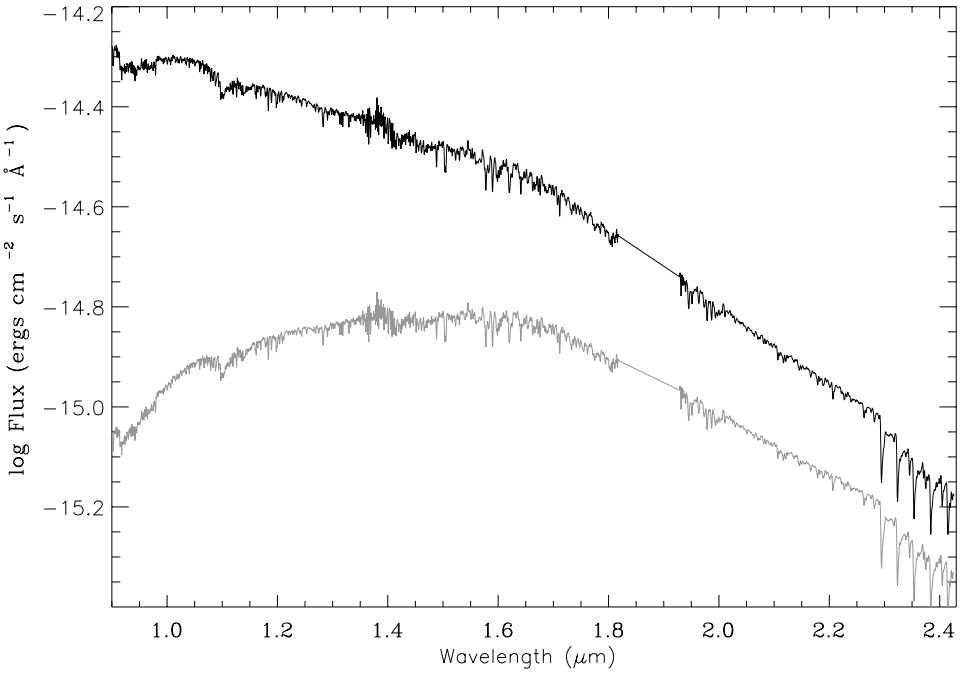

Figure 2.1: The NIR spectrum of V404 Cyg. The time-averaged spectrum, shown in gray, was obtained after correcting for atmospheric absorption and shifting the individual exposures to the rest frame of the donor star. The dereddened spectrum, using E(B-V)=1.303 (Hynes et al. 2009), is shown in black.

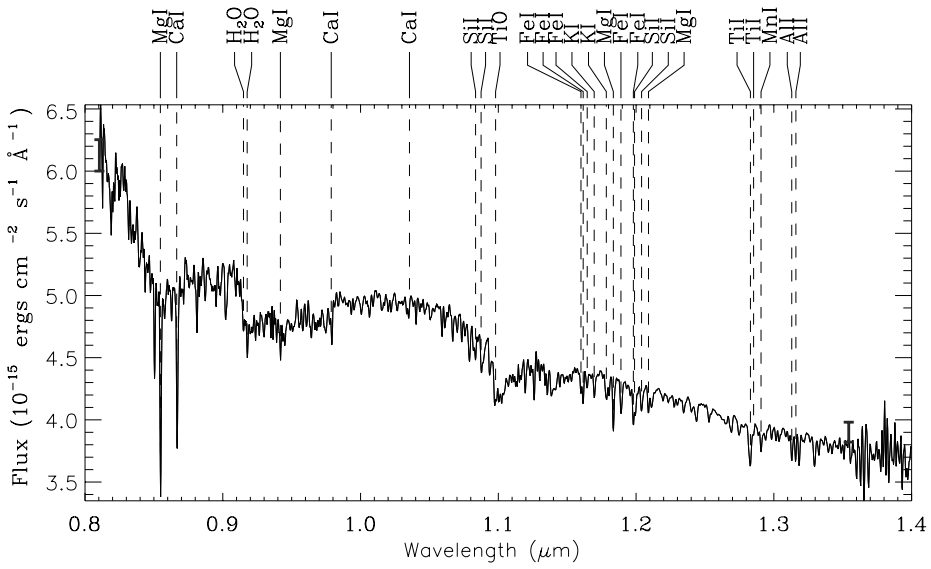

Figure 2.2: The J-band spectrum of V404 Cyg. Prominent spectral features are labeled at the top of the figure and representative error bars are shown near .81μm and 1.35 μm.

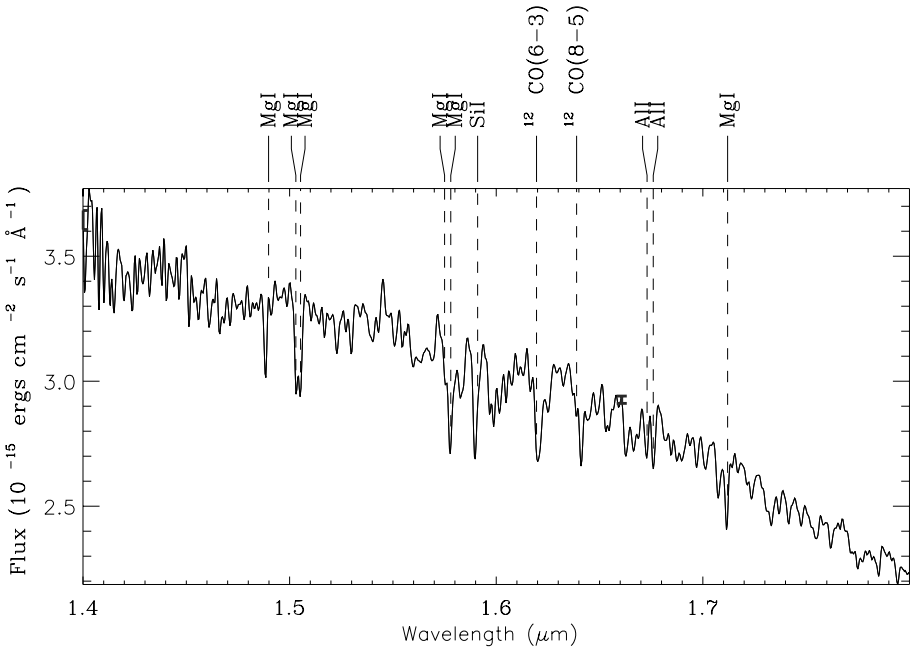

Figure 2.3: The H-band spectrum of V404 Cyg with representative error bars.

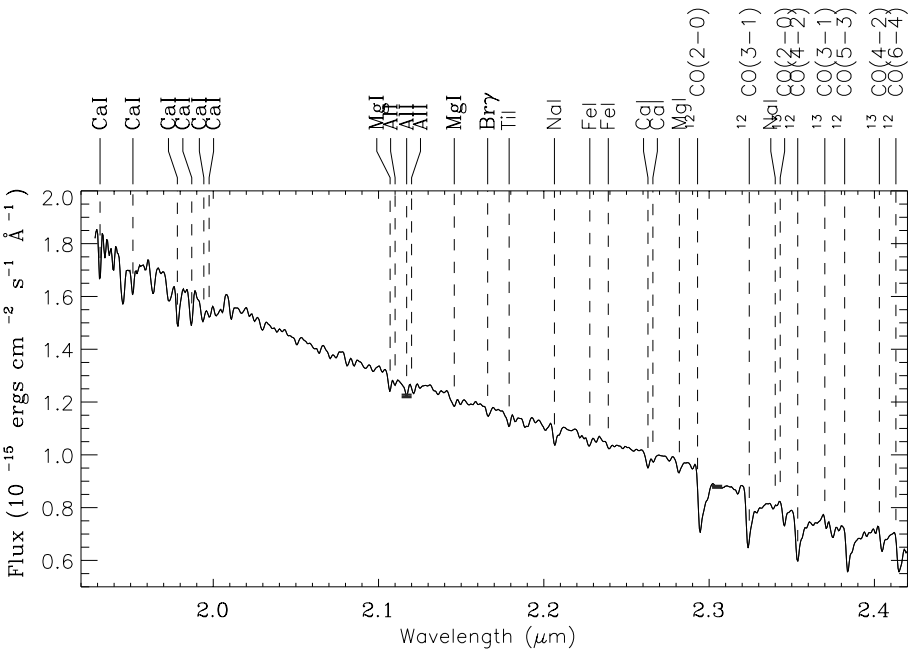

Figure 2.4: The K-band spectrum of V404 Cyg with representative error bars.

2.3 Analysis

The spectrum of V404 Cyg shows prominent narrow absorption lines of neutral metals including Al I, Na I, K I, Mg I, Fe I, Si I, Mg I, Ti I and Ca I. The H-and K-bands also show molecular absorption bands of ^{12}CO and ^{13}CO. The absorption lines originate in the donor star. In contrast to many other X-ray binaries, V404 Cyg does not show any strong emission lines in its infrared spectrum. Shahbaz et al. (1996) performed K-band spectroscopy of V404 Cyg and found no strong emission features either, implying that the non-stellar contribution (e.g. accretion disk) in V404 Cyg in quiescence is probably very low at all times. In the K-band, we see both ^{12}CO and ^{13}CO features which are a strong indication of an evolved donor star. We make use of the entire broadband infrared spectrum to ascertain the spectral type of the donor star and then obtain a precise value for the relative contributions of the donor star and other non-stellar sources (e.g. the accretion disk).

First, the broadband spectrum of V404 Cyg was compared to field stars of different

spectral types. These spectra were obtained from the IRTF Spectral Library[2] which consists of SpeX SXD spectra of stars of known spectral type (Rayner et al. 2009). The template stars used in the analysis have roughly solar metallicities and similar S/N to each other. We only used non-variable stars for our analysis. Earlier work done on the spectral type of the donor star in V404 Cyg suggested a K0IV spectral type (Casares and Charles 1994). In the IRTF spectral library, the closest available spectral type to a K0 IV is a K1 IV. Figure 2.5 compares the spectrum of a K1 IV (HD165438) star to the spectrum of V404 Cyg, normalizing the spectrum to that of V404 Cyg just blueward of 2.29μm. It is evident that the CO bands in the template spectrum are much weaker compared to those in V404 Cyg. Also, if the template is normalized to V404 Cyg in K, its flux exceeds the J-band flux in V404 Cyg flux by $> 30\%$, indicating that a K1 IV spectrum is too blue to match the donor star spectrum in V404 Cyg, unless there is another NIR flux source diluting its contribution.

Hynes et al. (2009) did a multiwavelength study of the spectral energy distribution (SED) of V404 Cyg in quiescence and found no substantial contribution from the accretion disk from near-UV to near-IR. They also found that for the donor, the spectrum of a K0 III star was in agreement with the data from UV to near-IR. At the same time, their multiwavelength SED comparison with a G8 III and a K2 III star could not be distinguished from a K0 III. A K2 III (HD 132935) spectrum was found to exceed most of the J-band (0.8 – 1.1μ m) flux by >7% when normalized in the K-band, indicating that a K2 III donor star spectral type would require a diluting flux source in the NIR. Also, the CO bands in a K2 III appear too weak to match that of V404 Cyg in the K-band. In Figure 2.6, a K3 III (HD 221246) spectrum is compared to that of V404 Cyg. In this case, the match is much closer, both in the broadband shape and spectral fluxes and in the relative depths of the CO bands. When normalized to a 100% in K, we find that the K3 III template exceeds the J-band, near the band edge (.8 – .9 μ m) by at most 5%. On the other hand, the K4 III (HD 207991) spectrum falls below the V404 Cyg spectrum in J by 20%, so that if that spectral

[2] http://irtfweb.ifa.hawaii.edu/ spex/WebLibrary/index.html

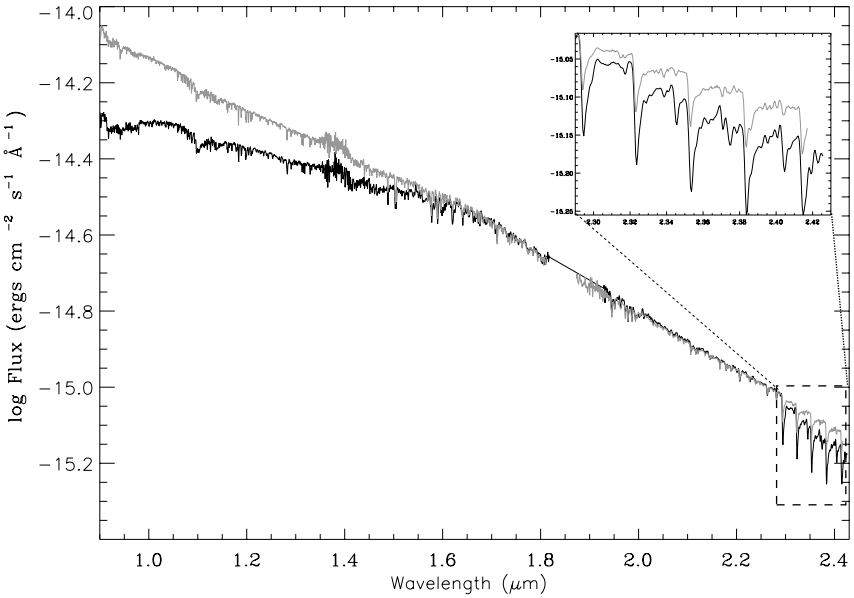

Figure 2.5: Comparison of V404 Cyg (shown in black) with a K1 IV field star (shown in gray). The template has been normalized to the spectrum of V404 Cyg just blueward of the 2.29μm ^{12}CO absorption bandhead. A zoomed–in version of the CO bands (2.29 – 2.42 μm) shows that a K1 IV star does not match the relative depths of the CO bands in V404 Cyg.

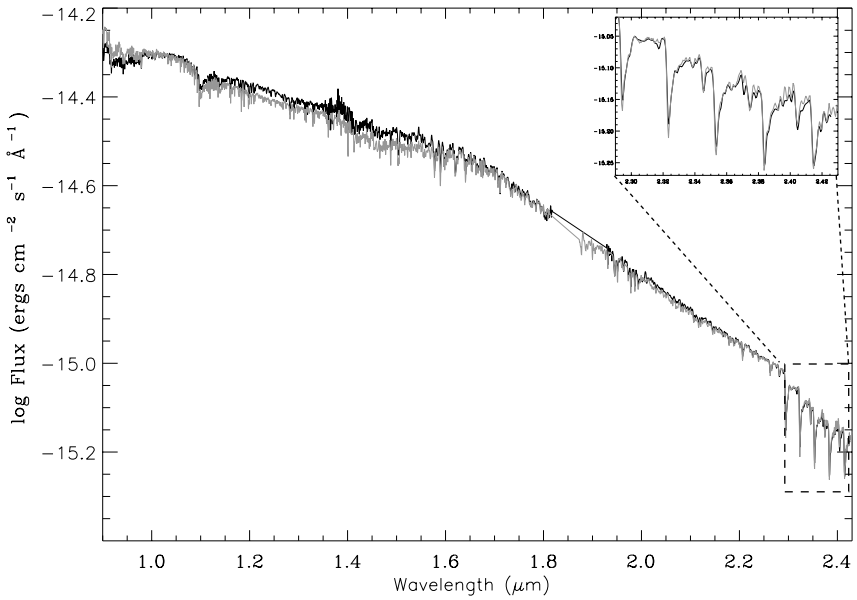

Figure 2.6: Comparison of V404 Cyg (shown in black) with a K3 III field star (shown in gray). The zoomed–in version of the CO bands shows a better match between a K3 III star and V404 Cyg with respect to the depths of these absorption features.

type is correct, the donor star may dominate the NIR flux in H and K, with an increasing non-stellar contribution at bluer wavelengths. In conclusion, both the spectral shape and the strength of the CO bands in V404 Cyg are inconsistent with a K1 IV spectral type for the donor star and indicate that a more evolved spectral type is better match to the donor star. In the next section, we calculate the equivalent widths of various lines of V404 Cyg and compare that to the same features in field star populations to determine the spectral type more precisely.

2.3.1 Equivalent width analysis

Förster Schreiber (2000), hereafter FS, used the equivalent width (EW) ratios of various NIR absorption lines in a population of field giants and supergiants (also a few dwarfs) as indices to determine stellar effective temperature and gravity as well as evidence of dilution from non-stellar sources. Table 2.2 lists the equivalent widths for V404 Cyg for the diagnostic features in FS. The error bars represent uncertainties in continuum placement only. By comparing our EWs to those in Figure 5 of FS, we obtain a donor effective temperature range of 4200–4600 K, implying a spectral type between K2 III and K4 III, assuming that the donor star is the only NIR flux source. FS also demonstrated how the EW ratios of certain lines would change if there was a source of diluting continuum emission. In their Figure 8 they plotted dilution-free indices (ratios of atomic/molecular EWs) and directional indicators to show how the indices would change as the contribution from a diluting source increases. A comparison of the same EW ratios in V404 Cyg to their indices shows that the V404 Cyg ratios fall on their plots for the non-diluted sources, suggesting that the amount of dilution in V404 Cyg in both H and K is negligible.

2.3.2 Field star fits to V404 Cyg

To obtain the fraction of NIR continuum emission originating from the donor star, f, the spectrum of V404 Cyg was compared with those of field stars ranging from K2 III to

Table 2.2: Equivalent widths for V404 Cyg using FS indices

Feature	Symbol	Integration limits	Equivalent width($\AA$)
SiI 1.5892	$\mathbf{W_{1.59}}$	1.5870-1.5910	3.36 ± 0.07
$^{\mathbf{12}}$**CO**$(\mathbf{6,3})$ 1.6187	$\mathbf{W_{1.62}}$	1.6175-1.6220	4.10 ± 0.08
NaI 2.2076	$\mathbf{W_{Na}}$	2.2053-2.2101	2.03 ± 0.10
FeI 2.2263	$\mathbf{W_{Fe1}}$	2.2248-2.2293	1.22 ± 0.74
FeI 2.2387	$\mathbf{W_{Fe2}}$	2.2367-2.2402	0.76 ± 0.12
CaI 2.2636	$\mathbf{W_{Ca}}$	2.2611-2.2662	2.06 ± 0.23
MgI 2.2814	$\mathbf{W_{Mg}}$	2.2788-2.2840	1.18 ± 0.18
$^{\mathbf{12}}$**CO**$(\mathbf{2,0})$ 2.2935	$\mathbf{W_{2.29}}$	2.2924-2.2977	9.11 ± 0.76
$^{\mathbf{12}}$**CO**$(\mathbf{3,1})$ 2.3227	$\mathbf{W_{2.32}}$	2.3218-2.3272	9.15 ± 0.28
$^{\mathbf{13}}$**CO**$(\mathbf{2,0})$ 2.3448	$\mathbf{W_{2.34}}$	2.3436-2.3491	3.30 ± 0.56

Note: The equivalent widths were calculated using the integration limits from Förster Schreiber (2000). The error bar on the measurements are based on continuum placement uncertainties.

K4 III spectral types. The spectrum of the template star was convolved with a Gaussian of 38.8 km s^{-1} FWHM in order to take into account the rotational velocity of the donor star in V404 Cyg (noting that this correction was negligible given the 250 km s^{-1} resolution of our spectra). Before fitting, the spectra of both V404 Cyg and the template were normalized by fitting cubic splines along the local continuum surrounding the lines under analysis. The continuum points were picked by eye. We determined the donor fraction as follows: after normalizing both the target and the template spectra, we multiplied the latter by a fraction, f, which was incremented from 0 to 1 in steps of 0.01. The result was subtracted from the spectrum of V404 Cyg to obtain the residual. We then minimized the chi-square, χ^2_ν, between the residual and the mean of the residual to obtain the donor fraction that gave us the best fit. In cases where the template had weaker absorption features compared to V404 Cyg, we let the donor fraction, f, take on values greater than 1. Even though this represents an unphysical scenario, it is useful as a guide to constrain the correct spectral type of the donor star by calculating the extent of weakness of the absorption feature in a particular template. For the fitting procedure, we selected only the strongest absorption features and fit absorption features for individual species separately. There were cases where absorption features of two different species occurred very close together in wavelength. If we were not able to separate them and identify the continuum around those absorption features, we did not include them in our analysis.

In order to better account for the uncertainty associated with the data, we divided our individual exposures into two sets. They were then separately combined and the result of one divided by the other. The deviation from the mean was then determined for each spectral order separately to assign the errors. Since the J-band comprises of three orders, we obtained the mean of these to assign the error bars for the J-band. We used these errors for the χ^2 analysis for V404 Cyg as it was clear that the statistical error bars were too small and did not account for systematic uncertainties in the data reduction process. For the template stars we used the statistical errors provided with the template spectra, but note that the

uncertainties for V404 Cyg dominate over the error in the template stars while fitting various spectral features. Table 2.3 shows the donor fractions calculated for K2 III, K3 III and K4 III spectral types along with the χ^2_ν values. When we compare the χ^2_ν values for fits across the entire K and H-band at once, we obtain K3 III as the best match for the donor in V404 Cyg. However, in order to make a final choice on the donor spectral type, we also looked at all the individual absorption features selected for analysis.

In the K-band, we fit the CO bands together from 2.29 – 2.42 μm and obtained the best fit with a K3 III spectral type. There is a Na I feature near 2.34 μm included in the fit region but the fit is dominated by the prominent CO-features. Generally, the K3 III star has the lowest χ^2_ν for fits to individual absorption features compared to the K2 III or the K4 III template stars. For the K2 III star all the absorption features are consistently weak in the template compared to V404 Cyg (resulting in the unphysical fit, $f > 1$). The K4 III template has fewer $f > 1$ deviations than for the K2 III star, but some of the lines cannot be fit with $f < 1$ and the χ^2_ν values are generally larger than for a K3 III template. Even for the K3 III template, some lines give $f > 1$ including the Mg I, Ca I and the Al I feature near 2.28 μm, 1.98 μm and 2.112 – 2.128μm, respectively. These features deviate less from $f = 1$ for a K3 III star than for the other templates but may indicate systematic mismatches (in temperature, gravity, or metallicity) between V404 Cyg and the field star templates. Overall, a K3 III star provides the most consistent match to the K-band spectrum of V404 Cyg.

In the H-band, looking at the CO features, $f = 1.24$ for the K2 III template, implying very weak ^{12}CO features in the template compared to V404 Cyg, whereas in K3 III and K4 III, the value of f is 0.98 and 0.95, respectively. In case of the K2 III star, the value of donor fraction is consistently > 1 for all the individual features in the H-band also indicating that most of its absorption features are weaker than in V404 Cyg. With the K3 III and K4 III stars, Mg I is always weaker in the template than in V404 Cyg (except for one feature at 1.71μm when compared against a K4 III template). This trend is also observed for the Mg

Table 2.3: Donor fractions, f,obtained for V404 Cyg with K2 III - K4 III field stars

Band	Wavelength range(μm)	Feature	f(K2 III)	χ^2_ν	f(K3 III)	χ^2_ν	f(K4 III)	χ^2_ν
	1.97 – 2.42	entire K-band	1.05	8.90	0.95	5.83	0.84	8.79
	1.97 – 1.99	Ca I	1.36	2.55	1.07	4.50	1.18	9.53
	2.112 – 2.128	Al I	1.50	0.20	1.05	0.52	1.57	0.35
K	**2.203 – 2.214**	Na I	1.50	0.24	0.94	0.15	1.07	0.23
	2.26 – 2.27	Ca I	1.24	0.21	0.85	0.15	0.98	0.26
	2.276 – 2.286	Mg I	1.60	0.89	1.25	0.87	1.87	0.73
	2.28 – 2.42	CO bands	1.05	13.0	0.95	6.70	0.87	17.80
	1.48 – 1.72	entire H-band	1.33	21.2	1.09	13.42	1.05	18.76
	1.48 – 1.52	Mg I	1.53	3.57	1.19	4.34	1.40	5.96
	1.574 – 1.587	Mg I	1.43	7.00	1.15	4.99	1.19	6.78
H	**1.584 – 1.595**	Si I	1.07	3.70	0.94	2.44	0.98	2.50
	1.615 – 1.650	CO bands	1.24	10.5	0.98	6.33	0.95	9.00
	1.670 – 1.678	Al I	1.32	3.77	1.03	2.14	1.17	1.85
	1.70 – 1.72	Mg I	1.56	4.00	1.18	5.57	0.98	5.00
	0.854 – 0.857	Mg I	1.02	1.27	0.91	0.51	0.95	1.05
	0.865 – 0.869	Ca I	1.03	1.71	0.89	1.62	0.93	2.15
	1.158 – 1.167	Fe I	1.11	0.08	0.83	0.10	1.09	0.12
	1.168 – 1.172	K I	1.23	0.04	0.96	0.07	1.11	0.08
	1.182 – 1.186	Mg I	1.33	0.19	1.12	0.09	1.24	0.05
	1.187 – 1.192	Fe I	1.08	0.09	0.85	0.02	0.90	0.03
J	**1.202 – 1.207**	Si I	1.23	0.04	1.05	0.02	1.17	0.03
	1.279 – 1.287	Ti I	1.59	0.23	1.38	0.21	1.59	0.40
	1.287 – 1.292	Mn I	0.99	0.05	0.88	0.02	0.95	0.03
	1.310 – 1.317	Al I	1.23	0.15	1.09	0.10	1.16	0.08

I line in the K-band. The same is true for the Al I feature in the H-band though it is close to $f = 1$ for the K3 III template. In the H-band too, we find that a K3 III star is the most consistent match to the donor star spectrum in V404 Cyg in terms of χ^2_ν as well as the strength of the lines indicated by the donor fraction.

In the J-band too, when we compare the χ^2_ν values and also the strength of the absorption features of the template with respect to V404 Cyg for the three different spectral types, a K3 III spectral type best matches the donor type in V404 Cyg. From our analysis with the spectral energy distribution, equivalent width calculation of various lines and direct determination of donor fractions, we conclude that the donor star in V404 Cyg has a K3 III spectral type. We see from Table 2.3 that the Mg I features for a K3 III spectral type have been consistently weaker in the template than in V404 Cyg (except the one feature near .856μm). This suggests an abundance mismatch between the template and V404 Cyg for this species. The same is perhaps true for Al I but there are not enough features to establish a consistent trend. For this reason, we did not include Mg I in our final donor fraction calculation.

Even though there is a good qualitative match between the spectrum and the K3 III template, our χ^2 statistics are poor, ranging from $\chi^2_\nu << 1$ for fits to individual lines in J and H to $>> 1$ for fits to individual lines in H and broadband fits in H and K. We attempted to take into account the systematic uncertainties that dominate in NIR ground-based spectra by recalculating the error bars as described above, but it is clear that our error bars are still too large in J and portions of K and too small in H. Due to this, we did not rely on χ^2 statistics to obtain our final donor fraction. Instead, we determined the donor fraction in V404 Cyg by taking an average of the best fits to multiple absorption features using a K3 III template and used the standard deviation between these line fits to represent the uncertainty on the final value of f. We believe this is a better tracer of systematic uncertainties in our fitting process because it also takes into account the possibility of slight mismatches between the V404 Cyg and the stellar template. Using this method, we obtained a H-band donor fraction

of $f = 0.98 \pm .05$ and a K-band fraction of $f = 0.97 \pm .09$. Thus, we find no substantial NIR contribution from the non-stellar sources in V404 Cyg similar to Hynes et al. (2009) and Shahbaz et al. (1996).

In Figure 2.7, we show the the K-band spectrum of V404 Cyg overplotted with the spectrum of a K3 III star scaled by a factor of 0.97. The close qualitative match between the template and spectrum is evident. The Mg I lines at 2.10 and 2.28 μm are weaker in the template spectrum than in the V404 Cyg. Shown in Figure 2.8 is the spectrum of V404 Cyg in the H-band over plotted with a scaled K3 III spectrum using $f = 0.98$. The Mg I lines at 1.50μm, 1.58μm and 1.71μm in the template are weaker than in V404 Cyg but the other absorption features give satisfactory fits.

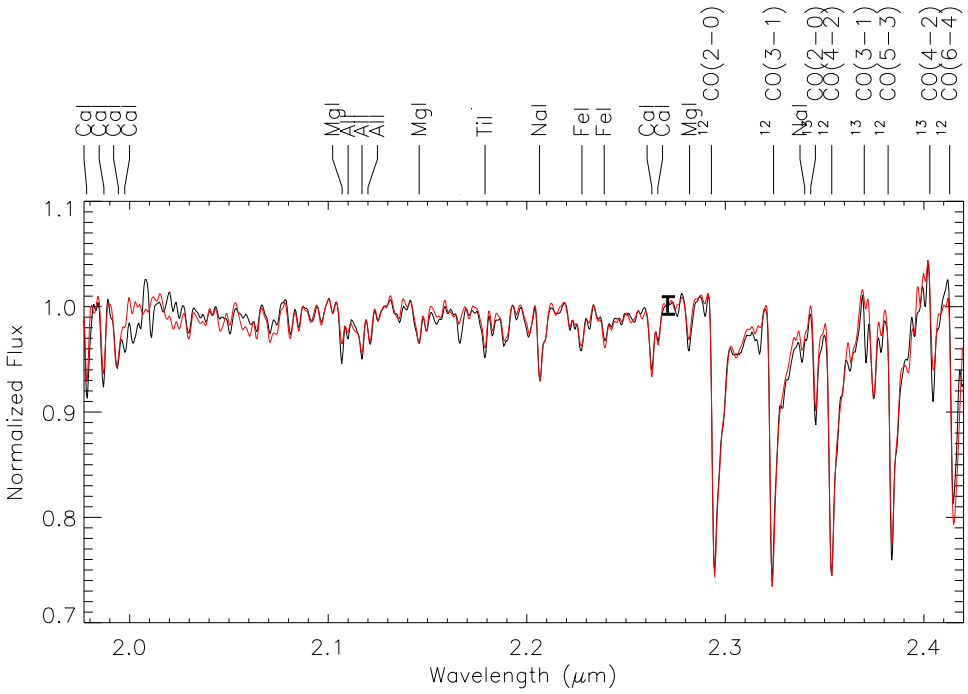

Figure 2.7: The normalized Kband spectrum of V404 Cyg (in black) is shown overplotted with a K3 III field star (red) normalized and scaled to $f = .97$ of K3 III field star. Representative error bars are shown in the figure.

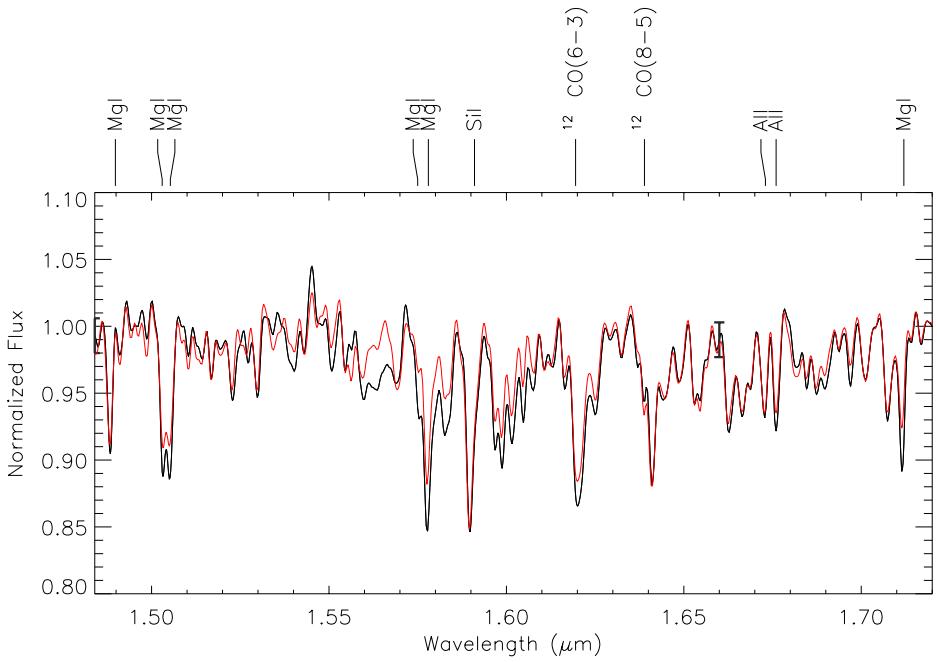

Figure 2.8: The normalized H-band spectrum of V404 Cyg (in black) is shown overplotted with a K3 III field star (red) normalized and scaled to $f = .98$. Representative error bars are shown in the figure.

2.4 Non-stellar contamination and mass of the black hole in V404 Cyg

Previous estimates have given K0 IV as the donor type in V404 Cyg (Casares and Charles 1994). Our high S/N NIR spectrum shows strong ^{12}CO and ^{13}CO features that point to a more evolved star. By comparing the spectral energy distribution with various field stars, EW diagnostics and dilution analysis, we found that a K3 III star is the best match to the donor star of V404 Cyg with minimal non-stellar contribution. From a comparison of the spectrum of V404 Cyg with a scaled K3 III star, one can appreciate the close qualitative match in the two spectra. In the K-band, the CO bands and most metals are consistent with the K3 III spectral type but Mg I appears supersolar in both the H- and K-bands. Unlike other compact binaries like A0620-00 (Froning et al. 2007), XTE J1118+480 (Haswell et al. 2002) and some cataclysmic variables (Harrison et al. 2000, 2004) that show weak CO

bandheads and depleted carbon abundances, the CO bandheads in V404 Cyg are consistent with the solar abundance K3III template spectrum.

Sanwal et al. (1996) obtained an H-band light curve of V404 Cyg. We retrieved their data from their Figure 2 and remodeled the light curve taking into account the (small) dilution of the donor star flux. The light curve modeling program is the same as used for A0620-00 (Froning and Robinson 2001). The parameters used for the model are T_{eff}=4300 K, a gravity darkening exponent of 0.08 (Lucy, 1967) and a limb darkening coefficient from Claret et al. (1995) for a $\log g$ value suitable for a K3 III star (Berdyugina and Savanov 1994; Cayrel de Strobel et al. 1980). For the error bars on the light curve, we used the scatter on the reference field star observed by Sanwal et al. (1996) (.02 mag) and equally weighted the points. For a mass ratio of $q = 0.060^{+.004}_{-.005}$ and $f(M) = 6.08 \pm .06$ (Casares and Charles 1994), the mass of the BH can be written to one unknown as $M_{BH} = (6.83 \pm .09)\ \sin^{-3} i$, where i is the inclination of the binary. We varied the donor fraction from .93 – 1.00 and obtained a best fit ($\chi^2_\nu = 3.3$) to the H-band light curve data for an inclination of $i = (67^{+3}_{-1})^\circ$ where the uncertainty in the inclination is propagated from the fractional donor star contribution. Figure 2.9 shows the best fit light curve of V404 Cyg obtained for $q = .06$ and $i = 67^\circ$. The uncertainty was dominated by the change in the donor fraction. The uncertainty in the mass reflects the uncertainty from varying the donor fraction. It does not include the uncertainty in the light curve measurements. Accordingly, we obtained the mass of the black hole in V404 Cyg as $9.0^{+.2}_{-.6} M_\odot$ for $q = 0.06$.

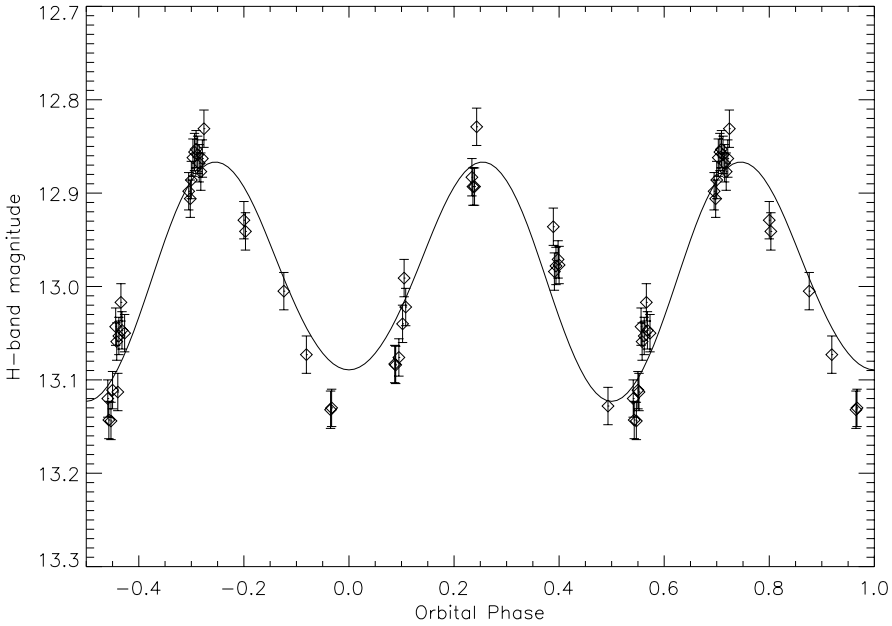

Figure 2.9: The best fit H-band light curve of V404 Cyg using the orbital ephemeris of Casares and Charles (1994). The data points (diamond) and the equally weighted error bars for each point are obtained from Sanwal et al. (1996). The solid line shows the best fit to the ellipsoidal modulation including 2% dilution from the non-stellar sources for an inclination of 67° and $q = 16.67$.

It has been shown in Cantrell et al. (2008, 2010) that fitting ellipsoidal models to the light curves of A0620-00 in its passive state increases the binary inclination considerably. The variability in the light curve shape (which can change from night to night) has been attributed to the disk component. Since V404 Cyg has a high S/N, we tested the stability of the donor fraction from the spectrum obtained for each individual night and found it to be fairly constant for each night. V404 Cyg exhibits fast strong variability which is likely produced by the disk (Sanwal et al. 1996). To test what effect that would have on the inclination and the black hole mass, we picked points from the lower envelope of their light curve data in Figure 1 by eye. We found a best fit for an inclination of $\approx 72°$ which translates to a reduction of black hole mass by about $1M_{\odot}$.

Shahbaz et al. (1996) obtained a 100% contribution of the donor star to the infrared

flux in the K-band which implies a binary inclination of 56°. Despite our comparable result for the donor contribution, their inclination does not agree with our value within the error bars. They used the light curve from Shahbaz et al. (1994) to determine the inclination. Sanwal et al. (1996) recalculated their K-band model light curve by equally weighing each night of data and obtained a significant improvement on the variance of the model light curve. From Figure 2 of Sanwal et al. (1996), for a mass ratio of q=.07, the absolute lower limit to the inclination corresponds to $\approx 60°$. They established an upper limit of $12.5 M_{\odot}$ for the mass of the black hole in V404 Cyg and our result is consistent with their limits with respect to both the inclination and the BH mass.

In our analysis, there are areas that contribute to systematic uncertainties which may not be accounted for in our final uncertainties. One of these is using a field star to duplicate the Roche-lobe filling donor stars. In V404 Cyg, we found that a K3 III field star with near-solar abundance matched the donor of V404 Cyg quite well except for the Mg I lines.

Previous studies have assumed that the light curve shape is consistent throughout quiescence. However, it has been shown in several systems that this assumption is not valid and will lead to systematic errors in the determination of the compact star masses (Cantrell et al. 2008, 2010). We obtained the spectra of our targets in 2007 whereas the light curve data for V404 Cyg were obtained in 1993 respectively. This wide time gap between obtaining the light curve data and the spectra adds to the uncertainty associated with the mass of the compact objects. In V404 Cyg, the non-stellar contribution is very small and has remained so over multiple observations (Shahbaz et al. 1996; Hynes et al. 2009). Our fractional contribution for the donor star agrees with the value obtained by Shahbaz et al. (1996) within their statistical uncertainties implying that the small non-stellar contamination in the K-band has changed negligibly in the time gap between the two observations.

2.5 Conclusion

We have obtained broadband near infrared spectroscopy of V404 Cyg in order to directly evaluate the relative contributions in the infrared light due to the donor star and non-stellar sources and determine precise compact star masses. We determined the spectral type of the donor star in V404 Cyg to be a K3 III. We performed dilution analysis based on individual prominent metal lines and groups of lines and determined the donor star fraction to be $0.98 \pm .05$ in the H-band and $0.97 \pm .09$ in the K-band. With previous light curve data in the H-band, we obtained the inclination of the binary as $i = (67^{+3}_{-1})^{\circ}$ and a mass for the BH of $9.0^{+.2}_{-.6}$ $M_{\odot}$. The mass estimated for the black hole should be viewed with some caution, however, since contemporaneous light curve and spectral data are required to obtain definitive masses.

Chapter 3

Mass of the Neutron Star in Cen X-4

3.1 Introduction

Cen X-4 was discovered on May 23, 1969 by the *Vela 5B* satellite (Conner et al. 1969) when it went into X-ray outburst. During its second outburst in 1979, it increased in visual magnitude by ∼6 magnitudes from its pre-outburst phase (Canizares et al. 1980). Matsuoka et al. (1980) identified the mass accreting star as a neutron star due to the fact that it displayed a Type I burst. Shahbaz et al. (1993) modeled the H-band light curve to obtain a binary inclination of 31°–54° and the mass of the neutron star as 0.5–2.1$M_\odot$. Torres et al. (2002) performed high-resolution optical spectroscopy on Cen X-4 in quiescence and determined the mass of the compact object as $0.49M_\odot < M < 2.49M_\odot$. They determined the mass function to be $f(M) = 0.220 \pm 0.005M_\odot$, which was later refined by D'Avanzo et al. (2005) to $f(M) = 0.201 \pm 0.004M_\odot$. The system parameters were again refined by Casares et al. (2007) and much tighter constraints were imposed on the radial velocity semi-amplitude, $K_2 = 144.6 \pm .3$ km s^{-1}, the orbital period, $P = .6290522 \pm .0000004$ d and the binary mass ratio, $q = .20 \pm .03$. The mass function adopted for this paper is calculated from the P and K_2 values of Casares et al. (2007), which is $f(M) = 0.197 \pm 0.001M_\odot$. However, as with V404 Cyg, in all the above cases, it was assumed that the donor star was the only NIR flux source, an assumption that has not been tested in Cen X-4.

In this paper, we present broadband (0.8–2.42 μm) NIR spectroscopy of Cen X-4 obtained with SpeX on the IRTF. By comparing the spectra to field stars of known spectral

type, we determine the donor star contribution to the infrared flux. We use these results to remodel previously obtained light curve data to determine the binary inclinations and to derive precise compact star mass for the black hole.

3.2 Observations

Like V404 Cyg, Cen X-4 was observed on June 7–9, 2007 with SpeX at the NASA Infrared Telescope Facility (Rayner et al. 2003). All observations were made using the Short XD (SXD) mode through the 0.5″ slit (R=1200), which covers the entire wavelength range, 0.8–2.4μm, simultaneously in 6 orders. An A0V star was observed hourly for the purpose of telluric correction. Observations were taken in ABBA pairs in two positions along the slit with a 300 sec exposure time at each position. The slit was oriented along the parallactic angle throughout the observations, limiting the relative flux calibration uncertainties to $< 2\%$ (Vacca et al. 2003). Table 3.1 lists the observations with the corresponding cumulative exposure times and orbital phases observed.

Table 3.1: Table of Observations for Cen X-4

Date	Exposure time(min)	Orbital Phase
06/07/07	100	0.80-0.92
06/08/07	30	——[a]
06/09/07	110	0.97-0.05

[a] Data from 06/08 was not used due to poor data quality at high extinction.

Data reduction consisted of calibration (sky subtraction, flat-fielding, wavelength calibration), optimal spectral extraction, and telluric correction, all of which were carried out using the idl based package Spextool (Cushing et al. 2004). Each exposure was shifted to the rest frame of the donor star, using the orbital ephemeris from Casares et al. (2007). The individual shifted exposures were median-combined and all 6 orders were merged to obtain the time-averaged spectrum. Using the magnitudes of the A0V star, the telluric correction

tool, `xtellcor`, also flux calibrates the spectra. Given our excellent observing conditions, the absolute fluxes should be fairly accurate, although we have not made any attempt to quantify the accuracy of those values, as they are not necessary for our analysis. Figure 3.1 shows the time-averaged spectrum of Cen X-4. It has been boxcar smoothed by 3 pixels and dereddened assuming E(B-V)= 0.1 (Blair et al. 1984). Figures 3.2, 3.3 and 3.4 shows the J-, H-, and K-band spectra of Cen X-4. We estimated the S/N in the time-averaged spectra of Cen X-4 by fitting straight lines through various continuum-dominated regions and measuring the scatter around these fits. For Cen X-4 we obtained a S/N $\approx$ 15–20 in J and K, and $\approx$ 25–30 in H.

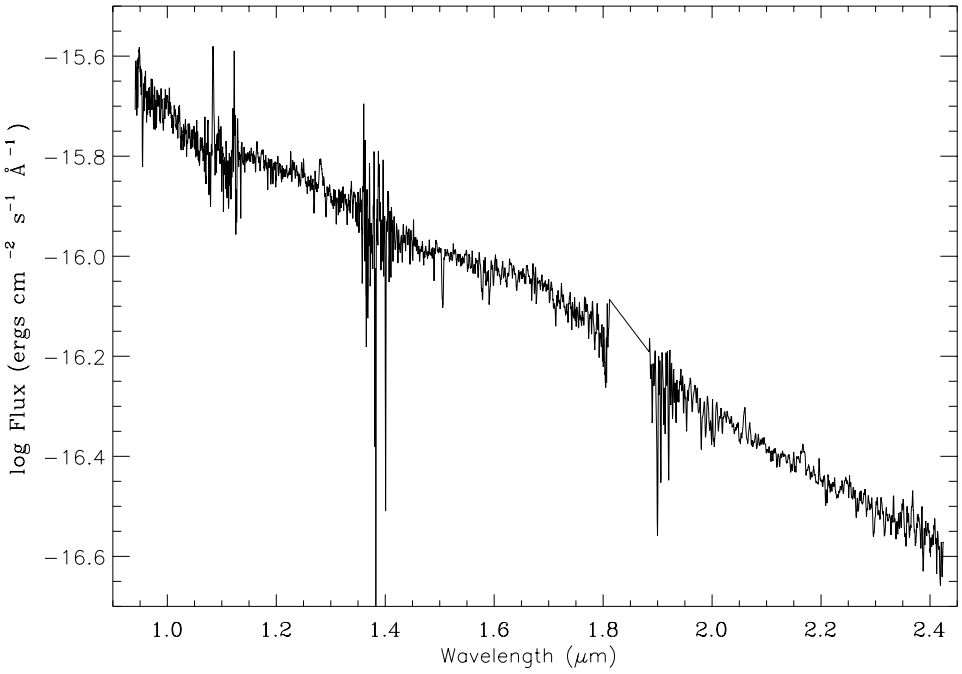

Figure 3.1: The NIR spectrum spectrum of Cen X-4. The time–averaged spectrum was obtained by correcting the individual exposures for atmospheric absorption and shifting them to the rest frame of the donor star. The spectrum has been dereddened using E(B-V)=0.1 (Blair et al. 1984).

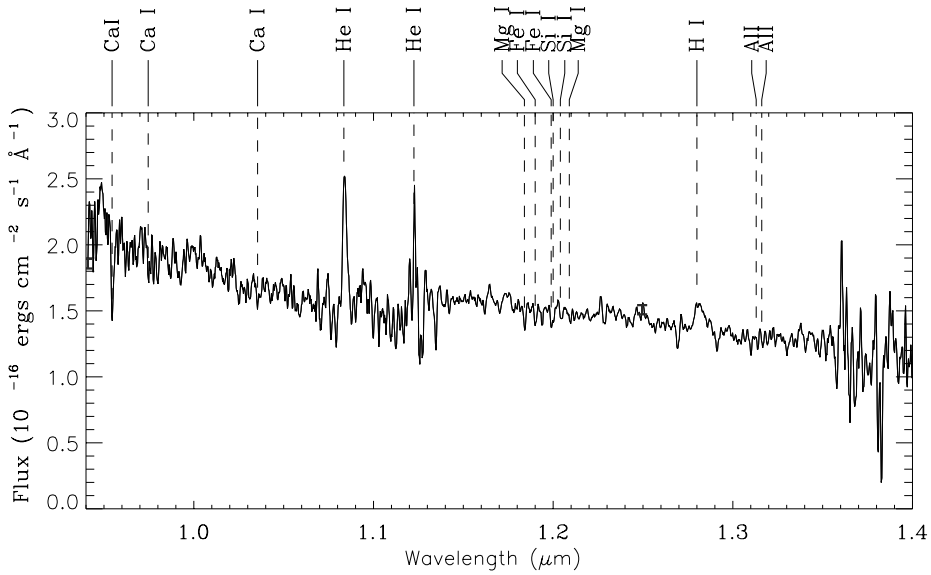

Figure 3.2: The J-band spectrum of Cen X-4. Prominent emission and absorption features are labeled at the top of the figure. Representative error bars are shown near wavelengths .94 μm and 1.25 μm.

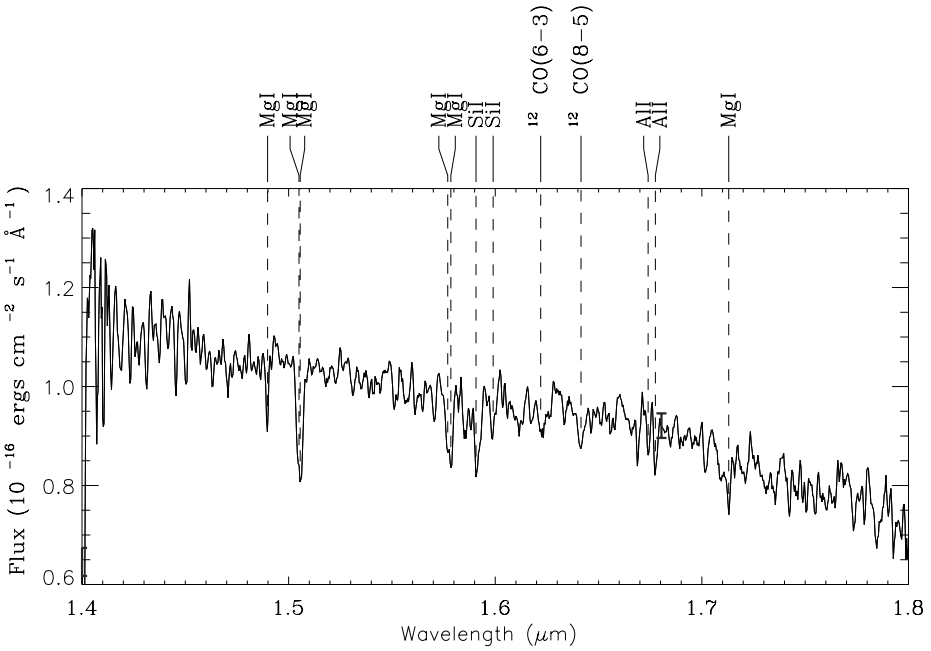

Figure 3.3: The H-band spectrum of Cen X-4 with representative error bars.

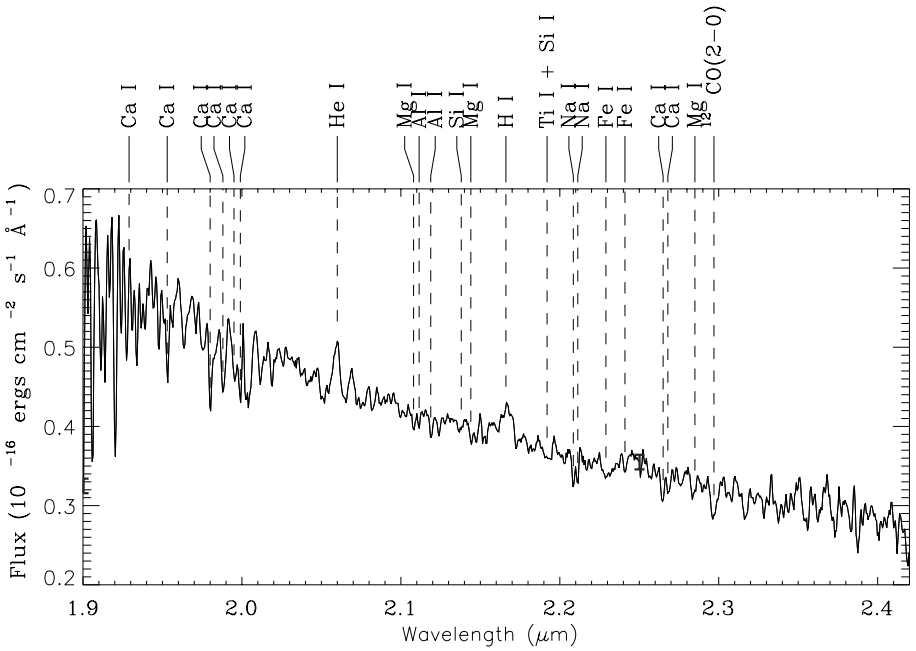

Figure 3.4: The K-band spectrum of Cen X-4 with representative error bars.

3.3 Analysis

The spectrum of Cen X-4 shows broad emission lines of H I and He I and narrow absorption lines of neutral metals including transitions of Na I, Mg I, Al I, Si I, Ca I, Fe I and molecules including ^{12}CO. The absorption lines originate in the cool donor star while the emission lines originate in the accretion disk. Chevalier et al. (1989) observed Cen X-4 in quiescence and determined the donor star to be of spectral type K5V – K7V. They also estimated that 25-30% of the total light was contributed by the accretion disk at visual wavelengths. In the infrared, the contribution from other non-stellar sources (e.g the accretion disk) to the total flux has traditionally been expected to be even less. Shahbaz et al. (1993) obtained the H-band light curve of Cen X-4 and predicted the contribution from the accretion disk to be significantly less than 10%.

Our spectrum of Cen X-4 is noisier compared to that of V404 Cyg which will make a precise spectral type determination more challenging. We compared the spectrum of Cen

X-4 with field dwarfs ranging from K5 – M1 V. The normalization was done at a wavelength just blueward of the ^{12}CO bandhead near 2.29 μm. If the donor star in Cen X-4 is the only contributor to the infrared flux, we find that the spectral types K5 – K7 V can be excluded. When the flux of a K5V star is normalized to that of Cen X-4 in the K-band, it exceeds the flux in the H-band by $> 15\%$. This excess in flux decreases as we move to cooler stars. For example, in Figure 3.5 we find an excess of $\approx 5\%$ in a K7 V star in the H-band and in the short J-band when normalized in K. From the comparisons, we conclude that if the donor star in Cen X-4 is the only NIR flux contributor, then it must be of spectral type later than K7 V; otherwise, some dilution must be present. For later spectral types, the flux of the donor star falls below that of Cen X-4 in the J-band and matches the H-band, as seen for an M0 V star in Figure 3.6. We also find $\approx 1\%$ (less than the error in the K-band) excess in the shorter K-band in all spectral types including an M0 V, indicating that some dilution, if quite small, may be needed for later spectral types as well.

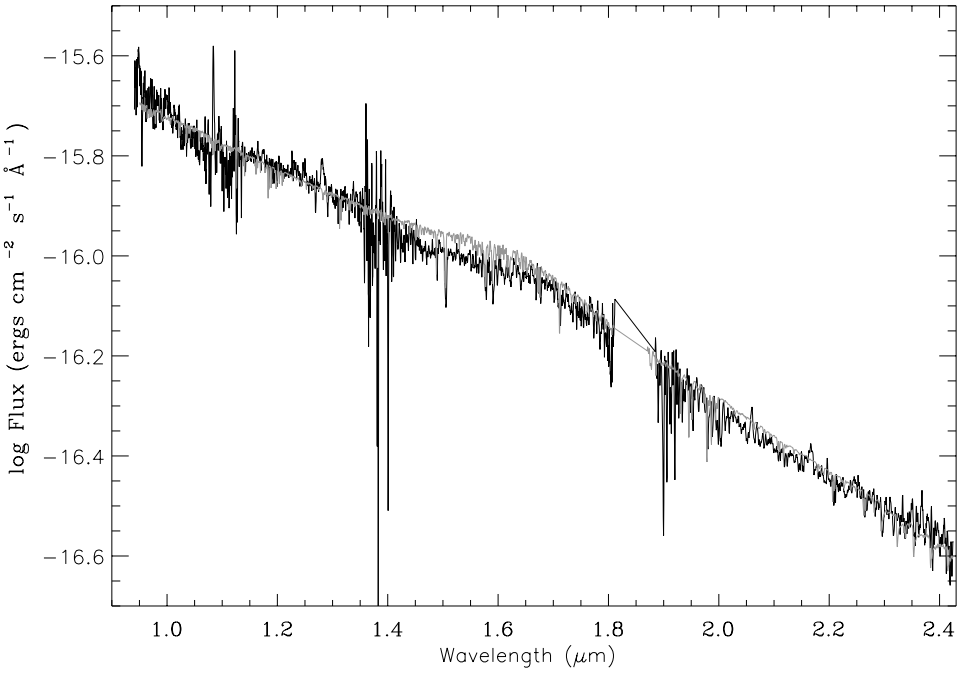

Figure 3.5: Comparison of the NIR spectrum of Cen X-4 (shown in black) with a K7 V field star (shown in gray). The field star spectrum has been normalized to that of Cen X-4 just blueward of ^{12}CO bandhead at 2.29 μm.

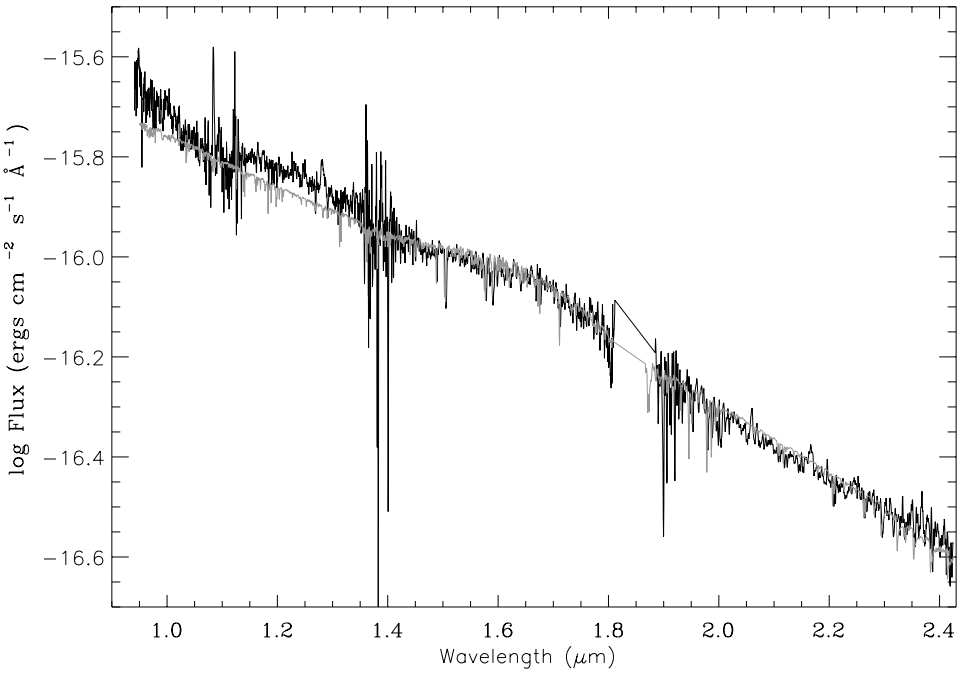

Figure 3.6: Comparison of the NIR spectrum of Cen X-4 (shown in black) with a M0V field star (shown in gray). The field star spectrum has been normalized to that of Cen X-4 just blueward of the ^{12}CO bandhead at 2.29 μm.

3.3.1 Equivalent width analysis

The analysis in FS focuses more on giants and supergiants than dwarfs, making use of the temperature and dilution indices ideal for V404 Cyg but less so for Cen X-4. However, we calculated the equivalent widths of the absorption features used by FS. Table 3.2 lists the values obtained for the equivalent widths of several absorption lines in Cen X-4. Due to the lack of data on dwarfs in FS coupled with a low S/N Cen X-4 spectrum, we obtained a large scatter in the T_{eff} values. We relied on just the prominent lines in Cen X-4 like the Ca I line at 2.26μm, the ^{12}CO bandhead at 2.29μm, the Na I line at 2.2μm, and the ^{12}CO bandhead at 1.62μm to constrain the spectral range of the donor. For Ca I at 2.26μm in FS, there are no data on dwarfs for the EW we obtained. With the remaining lines, we find K7 V – M1 V as the spectral range of the donor star in Cen X-4 in the event of no dilution.

Table 3.2: Equivalent Width analysis for Cen X-4 using FS indices

Feature	Symbol	Integration limits	Equivalent width($\mathring{A}$)
SiI 1.5892	$\mathbf{W_{1.59}}$	1.5870-1.5910	3.08 ± 0.41
$^{\mathbf{12}}$**CO**$(\mathbf{6,3})$ 1.6187	$\mathbf{W_{1.62}}$	1.6175-1.6220	1.90 ± 0.13
NaI 2.2076	$\mathbf{W_{Na}}$	2.2053-2.2101	2.56 ± 0.21
FeI 2.2263	$\mathbf{W_{Fe1}}$	2.2248-2.2293	2.25 ± 0.36
FeI 2.2387	$\mathbf{W_{Fe2}}$	2.2367-2.2402	0.51 ± 0.38
CaI 2.2636	$\mathbf{W_{Ca}}$	2.2611-2.2662	3.30 ± 0.55
MgI 2.2814	$\mathbf{W_{Mg}}$	2.2788-2.2840	0.89 ± 0.48
$^{\mathbf{12}}$**CO**$(\mathbf{2,0})$ 2.2935	$\mathbf{W_{2.29}}$	2.2924-2.2977	4.50 ± 0.44
$^{\mathbf{12}}$**CO**$(\mathbf{3,1})$ 2.3227	$\mathbf{W_{2.32}}$	2.3218-2.3272	3.01 ± 0.43
$^{\mathbf{13}}$**CO**$(\mathbf{2,0})$ 2.3448	$\mathbf{W_{2.34}}$	2.3436-2.3491	1.0 ± 0.59

The equivalent widths were calculated using the integration limits from Förster Schreiber (2000). The error bars on the measurements are based on continuum placement uncertainties.

Ali et al. (1995) have performed a similar analysis to FS but with emphasis on dwarfs ranging from F3 – M6 V. We calculated the equivalent widths for Ca I, Mg I, Na I and the ^{12}CO (2-0) band using the integration limits defined in their paper, which we show in Table 3.3. (Note that the FS and Ali et al. (1995) EWs are typically different for the same spectral features because of different choices in the integration limits over which the EWs were calculated.) We compared the EWs obtained for Cen X-4 with Figures 3 and 4 of Ali et al. (1995). Again, if we use only the prominent lines we find that the EW from Na I points to a spectral type K5 – K7 V and that Ca I predicts a spectral type later than K7 V. The EW of the ^{12}CO bandhead at 2.29μm gives inconclusive results as it falls within the flat portion of their data. The same is true for the Mg I feature. Ali et al. (1995) also noted that the sensitivity of CO to gravity makes it less useful as a temperature diagnostic. In the absence of dilution, we estimate the range of the spectral type of the donor in Cen X-4 as K5 – M1 V.

Table 3.3: Equivalent Width analysis for Cen X-4 using Ali et al. indices.

Feature	Symbol	Integration limits	Equivalent width($\AA$)
NaI 2.2076	$\mathbf{W_{Na}}$	2.204-2.211	3.33 ± 0.33
CaI 2.2636	$\mathbf{W_{Ca}}$	2.258-2.269	5.89 ± 1.23
MgI 2.2814	$\mathbf{W_{Mg}}$	2.279-2.285	1.65 ± 0.57
$\mathbf{^{12}CO(2,0)}$ 2.2935	$\mathbf{W_{2.29}}$	2.289-2.302	5.27 ± 1.09

The equivalent widths were calculated using the integration limits from Ali et al. (1995). The error bars on the measurements are based on continuum placement uncertainties.

Our conclusion from the EW calculation using the absorption features of Ali et al. (1995) is different from the estimate of FS in that we cannot rule out K5 V as a possible donor type. At the same time, from a spectral energy distribution comparison, if a spectral type as early as K5 V or K7 V were to be a possible donor in Cen X-4, we should expect to find some amount of dilution. We will examine the full K5 V – M1 V range to find out

the best spectral type for the donor in Cen X-4. In the next section, we present the results obtained from performing a dilution analysis.

3.3.2 Field star fits to Cen X-4

We compared the spectrum of Cen X-4 with those of field dwarfs: K5 V (HD36003), K7 V (HD237903) and M1 V (HD19305) spectral types from the IRTF spectral library using the same procedure used in calculating the donor star fraction in V404 Cyg. The spectrum of the template star was convolved with a Gaussian of 43 km s^{-1} FWHM to account for the rotational velocity of the donor in Cen X-4. The same procedure for determining the donor fraction in V404 Cyg was used for Cen X-4. For the fitting process, we chose only the most prominent absorption features in the spectrum of Cen X-4. The absorption features of individual species were fit separately and when such features occurred too close in wavelength such that the continuum region around an individual species could not be separated, we did not include that in our analysis. Due to the lower S/N, we fitted fewer lines than in V404 Cyg.

In order to better account for the systematic uncertainties, we determined the error bars in Cen X-4 by fitting straight lines through various continuum-dominated regions in the J-, H- and K-bands. For Cen X-4, we found this a more reliable method for error determination than the method of dividing the data into half used for V404 Cyg. (Since the NIR spectra of giants have fewer regions of continuum without strong line absorption, this method could not be applied in the error determination of V404 Cyg.) We propagated the error from the template stars as well in our analysis although the χ^2_ν values are dominated by the uncertainty from the Cen X-4 spectrum.

Table 3.4 shows the best fit donor fractions along with the χ^2_ν values obtained in Cen X-4 for various wavelength ranges with K5 V – M0 V template stars. When we compare the χ^2_ν values for fits across the entire K and H-band at once (after masking out the emission lines), we obtain an M0 V and a K5 V as the best matches, respectively. The entire J-band

could not be normalized satisfactorily at once and hence is absent in Table 3.4. We also looked at the χ^2_ν values and the donor fractions for individual lines. In the K-band, a K5 V star has the lowest χ^2_ν for most of the features while in the H- and the J-bands, it is an M0 V and a K5 V star, respectively. For all the features, we also examined the donor fractions for cases where $f > 1$. From Table 3.4, it is seen that in the K-band, an M0 V satisfies $f \leq 1$ for most cases and a K5 V does not; whereas in the H-band, all three spectral types are almost equally good, though the Si I feature (1.585 – 1.605 μm) gives $f > 1$ for all three templates. The same can be said of the J-band considering that the fractions $f = 1.03$ and $f = 1.06$ obtained for a K7 V and an M0 V in the Mg I feature are close to $f = 1$ (especially given the low S/N of Cen X-4). From this examination, it is evident that that data will not support narrowing the spectral type of the donor star from the K5V – M0V range under consideration.

Three features (the Na I line in the K-band, the Si I features in the H- and J-band and the Fe I feature in the J-band) are consistently weaker in all the templates than in Cen X-4. This might represent abundance mismatch between the donor in Cen X-4 and the templates akin to the mismatch seen in the Mg I feature in V404 Cyg. FS has noted that the temperature and luminosity variations of Ca I, Na I and Fe I features in the K-band are primarily governed by a blend of those species with Sc I, Ti I and V I which could explain why it is challenging to self-consistently match templates to these features. (A similar problem was encountered in K-band fits to the spectrum of A0620-00; Froning et al. 2007). These features cannot be eliminated from the final donor fraction calculation, however. Owing to the presence of only a couple of these species in the entire spectrum, it is not possible to make a decisive statement about abundance mismatch for specific elements. Other notable features are the ^{12}CO features in the K-band and in the H-band, which in other X-ray binaries such as A0620-00 have been anomalously weak. The CO feature in the K-band is much weaker in the template for a K5 V and a K7 V compared to Cen X-4, but all of the spectral types give consistent results of $f \sim 0.93$ for the H-band feature. A better S/N spectrum of Cen

Table 3.4: Donor fractions, f, calculated for Cen X-4 with K5 V - M0 V field stars.

Band	Feature	Wavelength range(μm)	f (K5 V)	χ^2_ν	f (K7 V)	χ^2_ν	f (M0 V)	χ^2_ν
	1.97 – 2.42	K-band	1.00	6.76	0.90	7.40	0.93	6.76
	1.97 – 1.99	Ca I	1.20	2.62	0.85	3.72	0.73	3.83
K	**2.203 – 2.214**	Na I	1.48	1.39	1.25	1.05	1.15	1.15
	2.260 – 2.272	Ca I	1.15	0.95	0.98	1.16	0.95	1.17
	2.295 – 2.305	^{12}CO	1.20	1.38	1.12	1.60	1.00	1.67
	1.48 – 1.72	H-band	0.89	2.56	0.93	2.75	0.92	2.76
	1.48 – 1.52	Mg I	0.93	1.24	0.97	1.07	0.98	1.20
	1.57 – 1.582	Mg I	0.95	0.90	1.04	1.02	0.98	0.85
H	**1.585 – 1.605**	Si I	1.10	1.37	1.15	1.60	1.22	1.33
	1.615 – 1.65	^{12}CO	0.93	1.02	0.93	0.96	0.92	1.20
	1.67 – 1.68	Al I	0.88	2.46	0.93	2.59	0.90	2.54
	1.70 – 1.72	Mg I	0.71	2.25	0.71	2.21	0.68	2.12
	1.182 – 1.186	Mg I	0.92	0.70	1.03	0.56	1.06	0.72
	1.187 – 1.192	Fe I	1.26	1.01	1.15	1.02	1.23	1.06
J	**1.202 – 1.207**	Si I	1.38	0.88	1.71	1.06	1.82	1.28
	1.310 – 1.317	Al I	0.86	1.55	0.86	1.92	0.80	0.93

X-4 is required to make a conclusive argument about this discrepancy especially as the S/N deteriorates sharply in the long K region where the CO bandheads occur.

We determined the final donor fraction by averaging over all the individual selected features from Table 3.4 for all three of the spectral type templates from K5 – M0 V. We obtain a mean donor fraction of $f = 0.94 \pm .14$ in the H-band and obtain $f = 1.09 \pm .20$ in K. Thus, the non-stellar sources can contribute up to 10% in the K-band. If a K5 V were to be excluded from the donor spectral type (based on its weak K-band features), we find a non-stellar contribution of up to 17% in K. This is consistent with the H -band fraction of 0.94, which would imply a $\sim$6 – 10% dilution in K (depending on the template spectral type). The H-band donor fraction contribution of $f = 0.94 \pm .14$ remains the same whether the K5 V star is included or not. Since the mass of the NS in Cen X-4 will be obtained from the H-band light curve data of Shahbaz et al. (1993), the inclusion or exclusion of a K5 V star will not affect the final mass. Figure 3.7 and 3.8 shows a comparison of the spectrum of Cen X-4 in the H- and K-band respectively, after scaling a K7 V and an M0 V template by a donor fraction of .94 and 1.0 respectively.

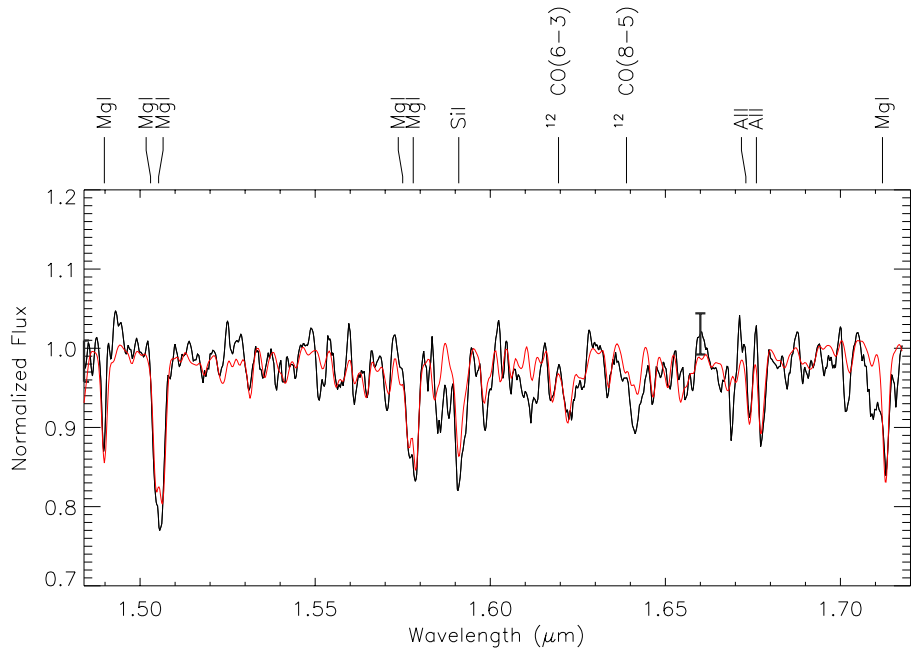

Figure 3.7: The normalized H-band spectrum of CenX-4 is shown in black. Overplotted in red is a K7V field star, normalized and scaled to $f = 0.94$. Representative error bars are shown in the figure.

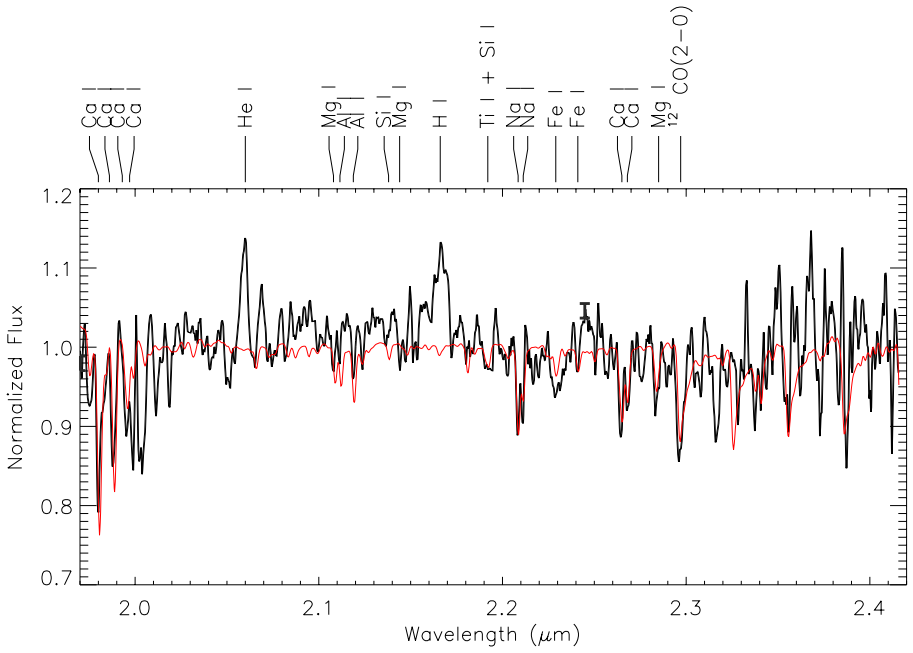

Figure 3.8: The normalized K-band spectrum of CenX-4 is shown in black. Overplotted in red is the spectrum of an M0 V field star, normalized and scaled to $f = 1.00$ with representative error bars.

3.4 Non-stellar contamination and mass of the neutron star in Cen X-4

From a comparison of the spectrum of Cen X-4 to those of various field dwarfs, we found that the donor star in Cen X-4 is probably not the only source of NIR flux. We found that in the H-band, a fraction, 0.94 ± 0.14, of the NIR flux comes from the donor star while in the K-band this fraction is $1.09 \pm .20$. Earlier estimates for the donor type in Cen X-4 include a K7 V star (Shahbaz et al. 1993) , a K3 V–K5 V star (Torres et al. 2002) and a K3 V–K5 V star (D'Avanzo et al. 2005). We have estimated the donor type in Cen X-4 to lie between a K5 V and an M1 V. If the donor star is a K5 V or K7 V, there must be at least 5 – 15% K-band dilution to reconcile the NIR spectral energy distribution in Cen X-4 with the template SED. A later type donor star of M0 V or M1 V requires only a few percent dilution in the K-band to match the broadband SED. Higher signal to noise data is required

to constrain the donor spectral type even further.

We use the orbital parameters from Casares et al. (2007) and determine the mass function is found to be $f(M) = .197 \pm .001$. Using this value of the mass function and the binary mass ratio, $q = .20 \pm .03$, the mass of the neutron star in Cen X-4 can be written upto one uknown as (0.28±.01) $\sin^{-3} i\ M_{\odot}$. For modeling purposes, we chose $T_{eff} = 4300$ K for a K7 V. We chose a value of $\log g$=4.5 appropriate for a K7 V star to obtain the corresponding limb darkening coefficients (Claret et al. 1995). We also chose a value of 0.08 for the gravity darkening coefficient assuming that the donor has a convective envelope (Lucy 1967; Sarna 1989). The flux from non-stellar sources will reduce the apparent amplitude of the ellipsoidal modulations which in turn will underestimate the binary inclination and overestimate the mass of the neutron star. We determined that the contamination from the non-stellar could be up to 20% in H. We can make an initial estimate of the mass of the neutron star in Cen X-4 by combining our dilution estimate with the H-band light curve observations of Shahbaz et al. We read in their light curve data from their Figure 1. Their data points include uncertainties in both magnitude and orbital phases, which was derived from how they binned their data (rescaling their errors in each phase bin to get $\chi^2_{\nu} = 1$ and then averaging the points). We could not read these values off their graph, so we assumed an equal weighting on each point using the 0.006 mag error for their reference star measurement.

In order to take into account the uncertainties in the orbital phase by Shahbaz et al. (1993), we varied the donor fraction in Cen X-4 from $0.80 < f < 1.00$ along with a phase-offset that gave the lowest χ^2 for a certain inclination. We obtained an inclination of $(35^{+4}_{-1})^{\circ}$ for the binary from which we obtained the mass of the neutron star as $M_{NS} = 1.5^{+.1}_{-.4} M_{\odot}$. Figure 3.9 shows the best fit ($\chi^2_{\nu} = 9.57$) to the H-band light curve (dashed line) of Cen X-4 for q = 0.20 and i= 36° for a phase-offset of .03, after it was modeled with a K7 V donor plus 6% constant dilution contribution. The solid line represents the best fit for no phase-offset ($\chi^2_{\nu} = 12.2$). Note, however, that the uncertainty on our final result only reflects the uncertainty in varying the donor star fraction. It does not include the uncertainty in

the light curve measurements. As a result, our derived neutron star mass and uncertainty should be viewed with some caution.

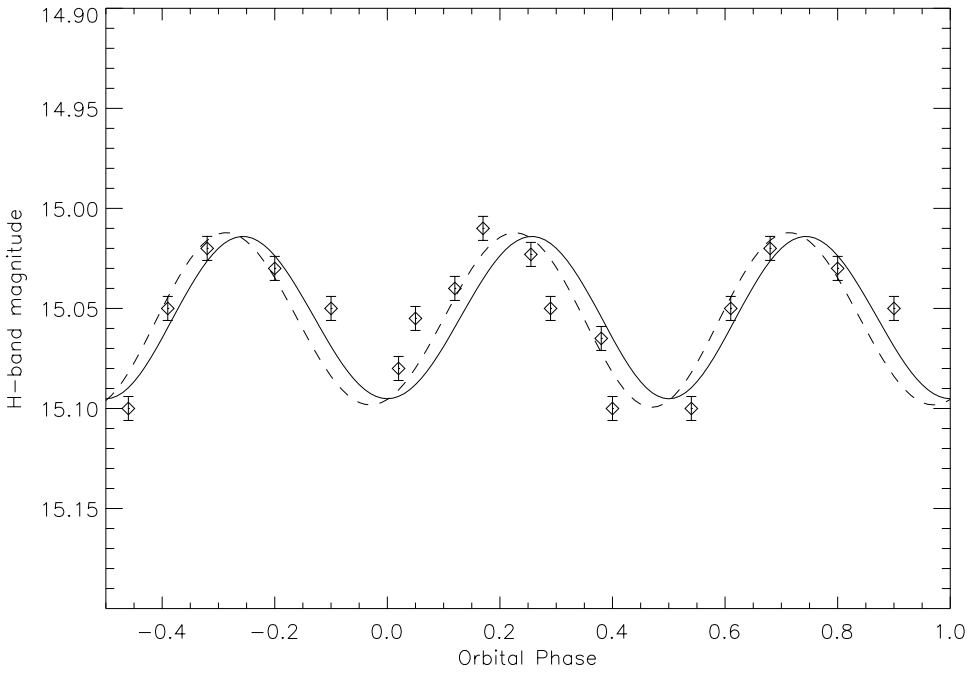

Figure 3.9: The best fit H-band light curve of Cen X-4 with zero phase-offset and an inclination of 35° is shown in solid while the dashed line represents the best fit for an inclination of 36° and a phase-offset of .03. The data points (diamond) and the equally weighted error bars for each point are obtained from Shahbaz et al. (1993). Both include 6% dilution from non-stellar sources and are plotted for q = 0.20.

With that caveat, the value $1.1M_{\odot} < M_{NS} < 1.6M_{\odot}$ we find is consistent with past estimates found by Casares et al. (2007), Torres et al. (2002), D'Avanzo et al. (2005) and Shahbaz et al. (1993). To include the spectral types between M0 V – K5 V we varied the temperature, T_{eff} from 3700 K to 4500 K, and found that the inclination changes by $\approx 1°$. We obtain the same variation in the inclination if we use $\log g$=4.0 if the donor in Cen X-4 were to be a sub-giant. The mass ratio value also has a negligible effect on the inclination.

Upon varying the mass ratio within its uncertainties (0.20±0.03), we found the inclination to change by less than a degree. The biggest uncertainty comes from varying the donor fraction than from varying any other parameters.

Both Chevalier et al. (1989) and Shahbaz et al. (1993) have argued that the donor in Cen X-4 is more likely a subgiant than a dwarf. They pointed out that based on the orbital period alone, if the donor were to be a main sequence star, it would underfill the Roche-lobe by a factor of ≈ 2. The CO bands would provide the best tracer of whether the donor star is evolved. We could not test this hypothesis here, both because of the relatively poor data quality in the long wavelength end of the K-band where the strongest CO bandheads occur, and because of the dearth of subgiant stars in the IRTF spectral library. Hence, the possibility that the donor in Cen X-4 could be a subgiant (later than K1 IV) remains open at this point .

It has been seen that pulsar masses are typically higher (≈ 1.50 $M_{\odot}$) in neutron star–white dwarf systems than in neutron star–neutron star systems and this is attributed to higher accretion in these systems (Nice et al. 2008). It has been pointed out by Shahbaz et al. (1993) that either the neutron star (NS) in Cen X-4 was formed as it reached the end of nuclear evolution in the progenitor's core or it could have collapsed to form a neutron star by gradual accretion onto a dwarf with electron degenerate core. In the latter case, the mass of the neutron star could be higher than typical neutron star masses as they can accrete up to several tenths of solar mass during their lifetimes (Casares 2006; Bhattacharya and van den Heuvel 1991). Our value of the mass of the neutron star in Cen X-4 exhibits a range of $1.1M_{\odot} < M_{NS} < 1.6M_{\odot}$ with the most probable value of $1.5M_{\odot}$. The error on the mass needs to be constrained further in order to realize whether Cen X-4 could be a potential system for understanding nuclear matter, and to rule out different equations of state similar to the neutron star LMXB candidate, Cyg X-2 (Casares et al. 1998). Both for the analysis done on V404 Cyg and Cen X-4, there exists systematic uncertainties which may not be accounted for in our final uncertainties. One of these is using a field star to duplicate the

Roche-lobe filling donor stars. For Cen X-4, we find that after applying the final donor fraction, some of the lines in the template were still weaker than Cen X-4. Using a field dwarf with solar abundances to represent a Roche-lobe filled star in Cen X-4 could be a plausible explanation for this discrepancy, as could minor mismatches between template and donor star in temperature, gravity, or metallicity. We attempted to mitigate this potential error source in Cen X-4 by averaging over fits to multiple lines and multiple spectral types to obtain the fraction and its uncertainty. Fortunately, our results are dominated by the H-band donor fraction where we obtained consistent results for all three template stars. It has been shown that the light curve will vary in morphology even in quiescence which will lead to systematic uncertainties in the compact object mass estimates (Cantrell et al. 2008, 2010). We obtained the spectra of our targets in 2007 whereas the light curve data for Cen X-4 were obtained in 1990-91 respectively. This wide time gap between obtaining the light curve data and the spectra adds to the uncertainty associated with the mass of the compact objects. For Cen X-4, we do not have as much information about the long-term variability of the system. However, the uncertainty on our donor star fraction ($\pm$14% in H) and resulting uncertainty on the neutron star mass is broad enough to span the observed range of variability in the system. We also note that the $1.5 M_{\odot}$ result is consistent with the masses measured in other NS LMXBs. Contemporaneous light curve and spectral data are recommended to obtain a definitive NS mass in Cen X-4.

3.5 Conclusion

We have obtained broadband near infrared spectroscopy of Cen X-4 in order to directly evaluate the relative contributions in the infrared light due to the donor star and the non-stellar sources and to determine the mass of its neutron star. We performed a similar analysis as in V404 Cyg but restricted our fits to the strongest absorption lines due to the lower S/N of the spectrum. We determined the spectral type of the donor star to lie within the range K5 V – M1 V but could not constrain it further. The dilution fraction was determined

to be $0.94 \pm .14$ in the H-band and $1.09 \pm .20$ in the K-band. From past H-band data we modeled the light curve with a donor star plus a constant flux from other non-stellar sources and determined the mass of the neutron star in Cen X-4 as $1.5^{+.1}_{-.4} M_{\odot}$ which agrees well with past estimates. However, contemporaneous light curve and spectral data are required to obtain definitive masses, and the mass obtained by us should be viewed with some caution.

Chapter 4

Mass of the Black Hole in XTE J1118+480

4.1 Introduction

XTE J1118+480 belongs to the class of transient low mass X-ray binaries (LMXBs) in which a late type donor star transfers mass to its compact companion (either a black hole or a neutron star) via an accretion disk. Accurate compact object masses are required to test models of formation and evolution of black holes (BHs) and neutron stars (NSs) (Brown et al. 1998; Fryer and Kalogera 2001; Nelemans and van den Heuvel 2001; Belczynski et al. 2011). XTE J1118+480 was discovered with the All-Sky Monitor (ASM) aboard the Rossi X-ray Timing Explorer (RXTE) satellite on March 29, 2000. Several independent observations obtained in quiescence have established various key properties of the binary, including its relatively short orbital period ($P_{orb} = 0.16$ days), a secondary star radial velocity semi-amplitude of $\sim$709 km s^{-1}, and a mass function (or minimum mass) of the compact object of $f(M) = 6.27 \pm .04 M_{\odot}$ (González Hernández et al. 2008). The minimum mass of the compact object has established beyond doubt that XTE J1118+480 contains a BH. Because of its location along a sightline of low interstellar absorption (A_V=0.06), this system has been extensively studied both in outburst and in quiescence at multiple wavelengths. These data have been used to test accretion disk and jet models (Yuan et al. 2005; Maitra et al. 2009), to test models of natal kicks and spin-orbit misalignments between the black hole and the accretion disk (Fragos et al. 2009), and to predict observational tests of braneworld gravity models (Johannsen 2009).

A BH is completely characterized by its mass and spin, and a reliable estimate of the latter is intricately dependent on the former (e.g. Steiner et al. (2009)). These two parameters are critical in understanding space-time behavior near the vicinity of a BH (McClintock et al. 2011). Observations of BHs in X-ray binaries are also key for understanding supermassive BHs in AGNs. Studies have revealed a "Fundamental Plane" of BH accretion in which X-ray luminosity, radio luminosity, and BH mass are related, both for Galactic BHs and their supermassive counterparts, implying that physical processes in AGNs can be determined from observations of similar processes in X-ray binaries by an appropriate scaling of the BH mass thereby allowing us to take advantage of the faster timescales of variability in X-ray binaries (Merloni et al. 2003; Falcke et al. 2004; Markoff et al. 2008). Compact object masses in LMXBs are commonly measured in the near-infrared (NIR), where the late-type donor star dominates. Often, investigators assume a negligible contribution from non-stellar sources (e.g. the accretion disk) at NIR wavelengths. However this assumption has often been questioned based on the work done by Cantrell et al. (2008, 2010); Reynolds et al. (2008). Unaccounted-for extra flux will lower the measured binary inclination from its true value and consequently overestimate the BH mass. This could potentially provide an explanation for the lack of observed low mass BHs seen in the $2-5M_{\odot}$ range in the observed NS-BH mass distribution (see, Bailyn et al. (1998); Farr et al. (2011); Özel et al. (2010)), for systems for which the minimum mass function falls within (or below) this range. BH masses are calculated by a combination of spectroscopy (to determine the non-stellar NIR light fraction) and light curve modeling (to determine the binary inclination after accounting for the non-stellar flux). However, Cantrell et al. (2008, 2010) have shown that XRB light curve morphologies can vary throughout quiescence. As a result, robust masses can be obtained only when light curve data is supplemented with contemporaneous spectral data.

Gelino et al. (2006) obtained the most comprehensive light curve data set of XTE J1118+480, covering the B, V, R, J, H and K wavebands and simultaneously modeling all the light curves to derive an inclination of $68^{+2.8}_{-2.0}$ degrees, allowing an accretion disk con-

tamination of at most 8% in the NIR. Their optical data were partly obtained in 2003 and partly in 2004 while their NIR data were obtained in 2003, five months prior to the 2003 optical data. Based on the work by Cantrell et al. (2008, 2010) on A0620-00, it is possible that XTE J1118+480 may have also change in morphology while it is in quiescence. This is suggested in the variation of the J-band light curve taken by Mikołajewska et al. (2005) five months after Gelino et al. (2006). Another complication in the analysis of Gelino et al. (2006) arises from the fact that the binary inclination and the disk light (in B and V) were derived by simultaneously fitting all the B-, V-, R-, J-, H- and K- band light curve data and by assuming negligible disk contribution in the J-, H- and K-band light curves. However, acquisition of their data was spread over various times; it is possible that both the non-stellar component of optical/NIR flux as well as the light curve shape may have varied during that time even when the system was in quiescence.

Motivated by the desire to measure an accurate BH mass in XTE J1118+480, we obtain contemporaneous light curve and spectral data of this system at NIR wavelengths to establish the non-stellar light from spectroscopy at the time of acquisition of light curve so that true binary inclination of this system can be obtained. In the following sections, we estimate the veiling caused by the non-stellar components at NIR wavelengths by measuring the EWs of absorption lines in the photosphere of the donor star. We accounted for this extra NIR light when fitting ellipsoidal models to the observed light curve data in order to obtain a true and robust value of binary inclination and consequently the BH mass.

4.2 Observations

XTE J1118+480 was observed with the Near-Infrared Camera & Fabry-Perot Spectrometer (NICFPS) on the 3.5-m telescope at Apache Point Observatory (APO) and with the Gemini Near-Infrared Spectrograph (GNIRS) at Gemini-North. All photometry and spectroscopy data were initially scheduled to be acquired on April 2 and April 3, 2011 at both locations. We achieved this goal for the night of April 2, 2011. Additional light curve

data were obtained on April 3, 2011 but due to continual bad weather at Mauna Kea, we finished the remainder of our spectral observations on April 12, 2011, giving us contemporaneous light curve and spectral data. Table 4.1 lists our observations, the exposure times used and the orbital phase coverage.

4.2.1 Spectroscopy

We observed XTE J1118+480 using GNIRS at Gemini-North. Spectroscopy of XTE J1118+480 was obtained in the cross-dispersed mode with the 31.7 line mm^{-1} grating and the 0.30″ wide slit, yielding R ∼1700 while effectively covering the entire near-infrared range from 0.9 – 2.5 μm. We achieved a total on-source observing time of 4.1 hrs. Data were taken in ABBA pairs at two positions along the 7.0″ long slit with a 310 sec exposure time at each position. The slit was oriented along the mean parallactic angle throughout the observations. An A0 V type telluric star was observed hourly with the same configuration with 5 sec exposure times. From two nights of data we were able to cover all binary phases at least once, except phases $\phi = 0.10 - 0.35$ and $\phi = 0.72 - 0.76$ which were covered twice. The raw data were reduced using the GNIRS tools within the Gemini-IRAF package, version v1.11. The raw images were first treated for fixed pattern noise using the `cleanir` [1] tool. The other data reduction steps consisted of flat-fielding, sky subtraction and wavelength calibration. Owing to the faintness of the target, we could not confidently extract the spectra from the individual sky-subtracted exposures. Instead, to improve the signal-to-noise in the exposures to be extracted, we combined every three exposures (adjacent in phase and equivalent to 5% of one full orbit) to perform reliable spectral extraction. The spectrum extracted in this manner were minimally affected by orbital smearing effects when compared with the instrumental resolution of 177 km s^{-1} when averaged. Flux calibration and telluric correction were performed with the `xtellcor` package within Spextool (version 3.4) (Cushing et al. 2004; Vacca et al. 2003). We shifted each of the extracted spectra to the rest frame

[1] http://staff.gemini.edu/ astephens/niri/cleanir/

of the donor star using the orbital ephemeris of Calvelo et al. (2009), median-combined each order separately, and merged all the orders to generate the time-averaged spectrum of XTE J1118+480 shown in Figure 4.1. The spectrum has been boxcar-smoothed by 2 pixels, corresponding to one resolution element. The spectrum in Figure 4.1 was corrected for interstellar absorption using A_V=0.066 (Gelino et al. 2006). We did not attempt to quantify the flux calibration accuracy since the spectral analysis of XTE J1118+480 does not require absolute flux values. However, we find that the mean H-band flux of the spectrum agrees with the photometry within $\sim 4\%$.

4.2.2 Photometry

Light curve data were obtained with NICFPS at APO in the H-filter. We used individual exposure times of 20 seconds for the target. A standard star for flux calibration was observed every 1.5 hrs along with the target observations. We had excellent seeing conditions ($\sim 0.6''$) on the night of April 2, 2011 but on April 3 the seeing conditions went from moderate ($\sim .8''$) to poor ($> 1.0''$) after the first two hours of observing and the data were discarded. The binary orbital phases between $\phi = 0.1 - 0.2$ and $\phi = 0.33 - 0.5$ were not covered at all, but all other phases were covered more than once. To account for the dark current in the NICFPS exposures, dark frames matching the exposure times of the target and standard star were obtained at the beginning of each observing run and subtracted from the target /standard star exposures. Finally, the images were flat-fielded with sky-flats. We obtained five point dither images of the field, each offset by $20''$, and constructed a sky-flat by median-combining these exposures. To obtain sufficient signal to noise in our reduced data images, we median combined every three exposures (equivalent to $\sim$ 60 seconds) to construct final reduced images. Aperture photometry was performed on the combined images using the IRAF `phot` package. For flux calibration, we used the stars in the field of XTE J1118+480 selected from the Two Micron Sky Survey (2MASS) catalogue as well as the ARNICA (Arcetri NICMOS3 camera) near-infrared standard star AS-11 (Hunt et al.

1998).

Table 4.1: Table of observations

Observations	Date	Individual Exposure time(seconds)*	Binary Orbital Phases Covered
Spectroscopy	04/02/11 04/12/11	310 310	0.13 – 0.39, 0.72 – 0.98 0.06 – 0.32, 0.49 – 0.76
Photometry	04/02/11 04/03/11	20 20†	0.00 – 0.35, 0.40 – 0.99 0.18 – 0.99, 0.01 – 0.04

* A total on source integration time of $\sim$ 2.7 hours was obtained each night for spectroscopy and $\sim$4.5 hours for photometry.

† Data after the first 2 hours of observation were discarded owing to bad weather.

4.3 Analysis

4.3.1 Spectroscopy

The spectrum of XTE J1118+480 displays narrow absorption lines of neutral metals including transitions of Al I, Na I, Mg I, Fe I and Si I which are believed to originate in the photosphere of the donor star. We also detect broad emission lines of H I and He I from the accretion disk. These J-, H- and K-band spectra are shown in Figures 4.2, 4.3 and 4.4. We identified spectral features using line identifications from Wallace and Hinkle (1997), Wallace et al. (2000), Kleinmann and Hall (1986), Meyer et al. (1998), Kirkpatrick et al. (1993), Rayner et al. (2009) and the Atomic line list[2] . In Figures 4.2, 4.3 and 4.4, the error bars were calculated for each resolution element (=2 pixels) by fitting straight lines through several continuum-dominated regions and obtaining the scatter about that line. The continuum-dominated regions were selected in XTE J1118+480 after an inspection of

[2] http://www.pa.uky.edu/ peter/atomic

similar featureless regions in K5 V – M1 V template stars. We obtained signal-to-noise (S/N) estimates of ~ 18 in the H-band and ~ 15 in the J- and K-bands respectively.

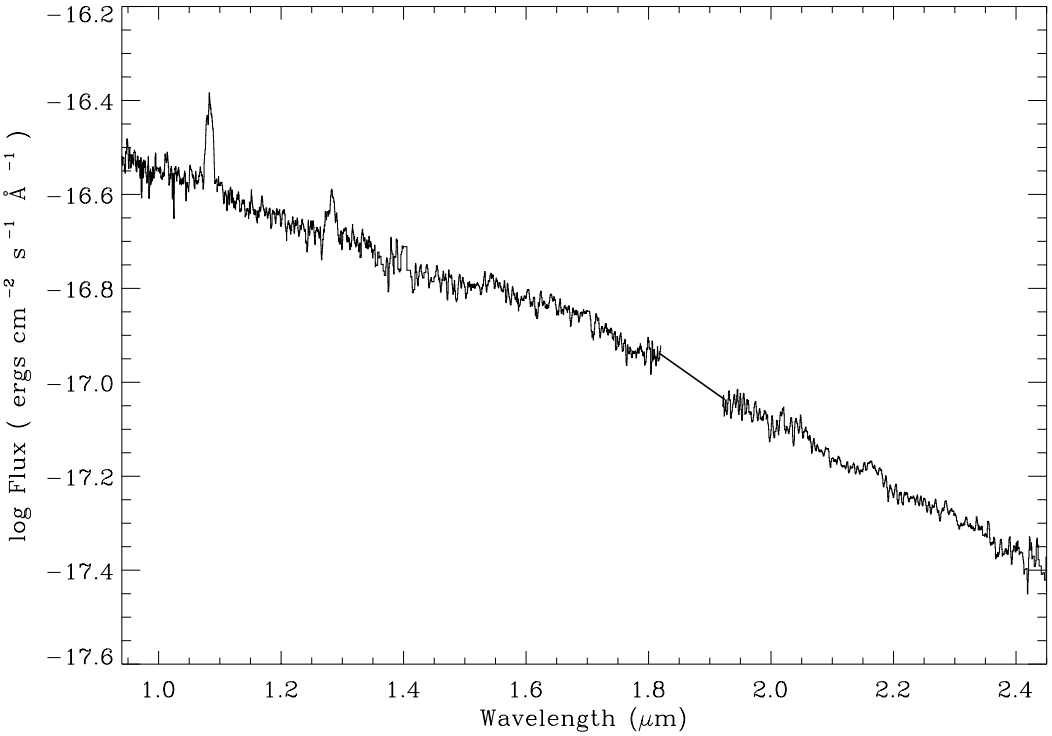

Figure 4.1: The time-averaged spectrum of XTE J1118+480 obtained after correcting for atmospheric absorption and shifting the individual exposures to the rest frame of the donor star. The dereddened spectrum, using E(B-V)=0.06 (Gelino et al. 2006), is shown in black.

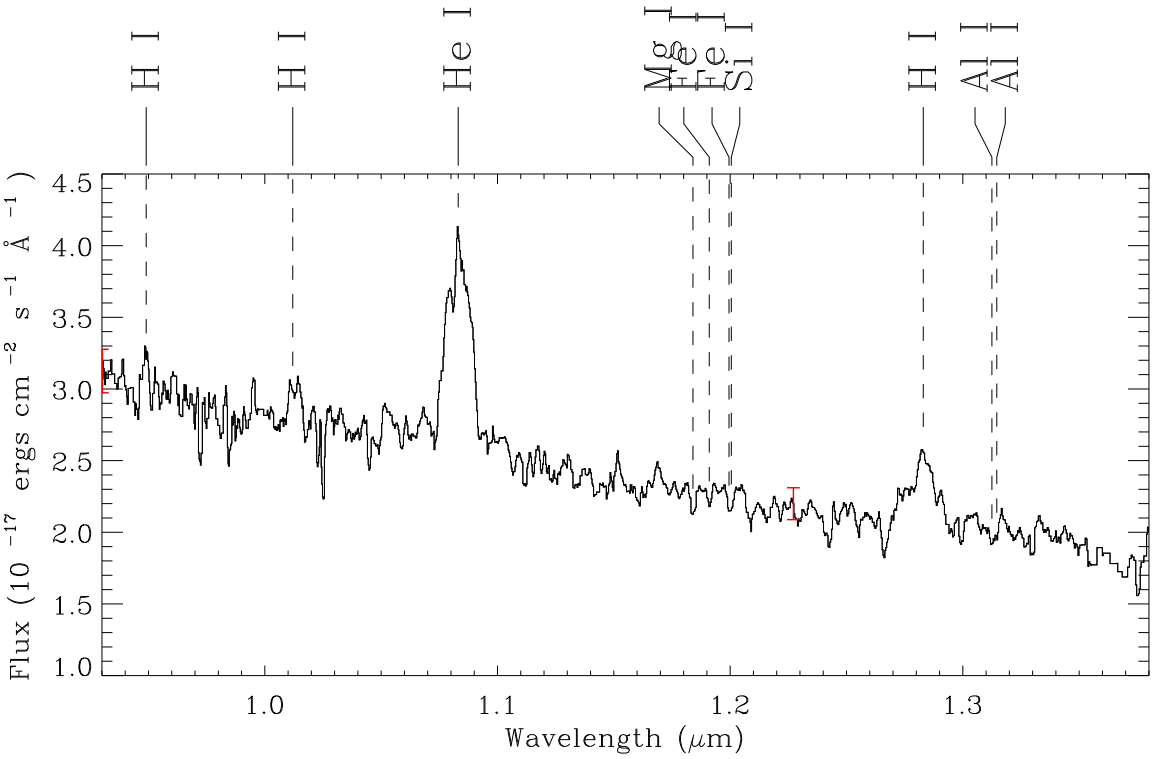

Figure 4.2: The J-band spectrum of XTE J1118+480 showing emission features from the accretion disk and absorption features from the donor star in XTE J1118+480. All line identifications do not imply an actual detection due to the low S/N of the spectrum. The typical error bar is shown in red.

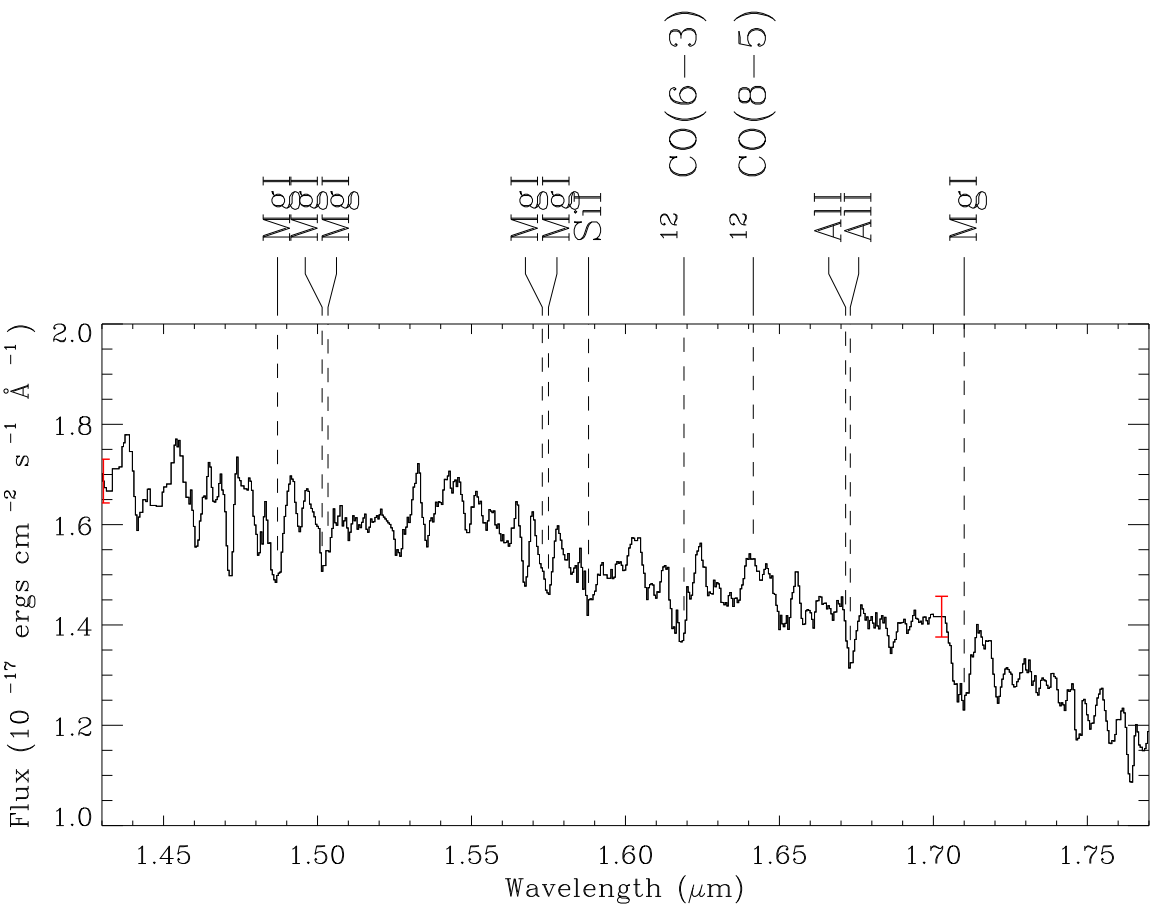

Figure 4.3: The H-band spectrum of XTE J1118+480. The typical error bar is shown in red.

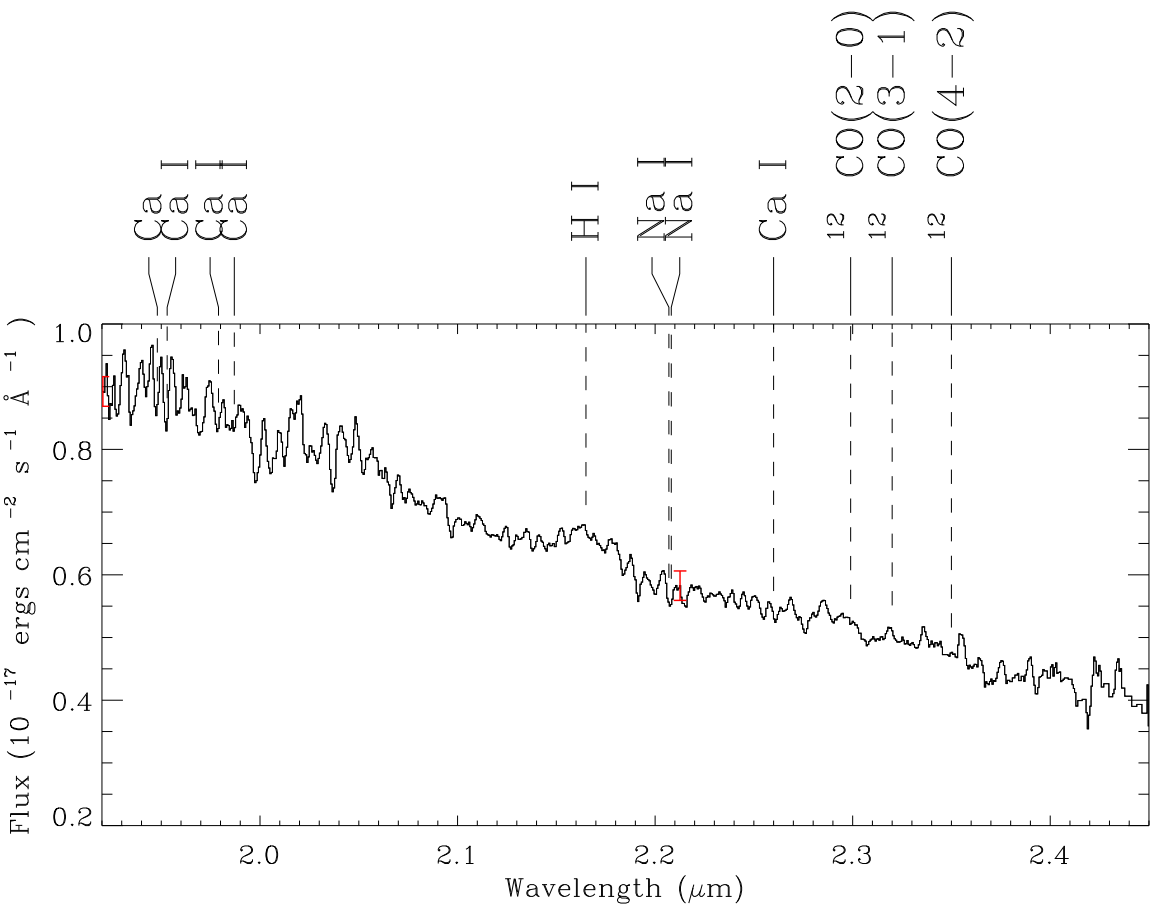

Figure 4.4: The K-band spectrum of XTE J1118+480. All line identifications may not imply an actual detection due to the low S/N of the spectrum. The typical error bar is shown in red.

In the J-band we detect a few absorption features in the 1.175 – 1.320 μm range, mainly blends of Mg I, Si I, Fe I and Al I, and broad emission features of H I and He I. In the H-band, we observe narrow atomic features of Mg I, Al I and Si I which are marked in Figure 4.3. The Al I doublet at ∼1.167 μm. When compared to field stars of spectral type K5 V – M1 V, the bluer component of the Al I doublet in XTE J1118+480 appears much weaker than its red counterpart. This behavior is contrary to the observation that the strength of both these features attain a comparable maximum depth in K–early M type dwarfs (Meyer et al. 1998; Rayner et al. 2009). In the K-band, the most prominent features used for spectral classification are the ^{12}CO bands, Na I and Ca I, with Na I being more temperature sensitive

than Ca I (Kleinmann and Hall 1986). The position of these lines are marked in Figure 4.4. The centroids of the Na I line at 2.20 μm and the Ca I lines between 1.94–1.99 μm are consistent within the wavelength calibration accuracy of $\sim \pm 0.002$ μm but Ca I at 2.264 μm is not (centroid of this feature ¿ $\pm 0.002\mu$m of the true wavelength). Also, the strength of the Na I feature is at the same level as the average noise in the K-band and is therefore not a very reliable detection. There is also a weak emission feature of H I at 2.16μm. We do not detect any CO features in the K-band. Enhanced N V and depleted C IV and O V emission lines have been seen in the UV spectrum of XTE J1118+480 suggesting that the accreting material has been CNO processed (Haswell et al. 2002). Therefore, our non-detection of the CO-bands in the K-band is expected. However, in the H-band, we apparently detect the ^{12}CO (6,3) feature at 1.619 μm. This contradicts our non-detection of CO in the K-band but this apparent contradiction is also noticed in the spectrum of A0620-00 (compare Figures 6 and 7 in Froning et al. (2007)). The ^{12}CO (6,3) band contains a blend of several other species such as Ca, Fe, Ni, Si and OH whose contributions might mislead one into believing that a possible CO feature exists at 1.619 μm. This detection is further made questionable by the fact that the second overtone ($\Delta\nu = 3$) bands of CO near the 1.1619 μm have oscillator strengths that are approximately 100 times smaller than the first overtone bands near 2.29 μm (Gautier et al. 1976) and therefore very unlikely that we should detect the former and not the latter. Therefore, we do not include the CO-features in the H-band in our analysis.

The spectral type of the donor star in XTE J1118+480 has been broadly be classified as K5 V – M1 V (González Hernández et al. 2008; Gelino et al. 2006; Wagner et al. 2001; Frontera et al. 2001; McClintock et al. 2001). We seek to constrain the spectral type of the donor star further and to estimate the relative contribution of near-infrared light from the donor star and non-stellar sources. Towards that end, we will make use of the broadband spectral energy distribution (SED) of XTE J1118+480 in conjunction with fitting field star spectra to donor star absorption features. The use of our spectrum to obtain reliable estimates of the donor spectral type of XTE J1118+480 and non-stellar light is challenging

because of the low signal-to-noise ratio (S/N ∼15–18) of the spectrum. Figure 4.5 shows the spectrum of XTE J1118+480 compared to the spectrum of a K5 V star (in red) and M1 V star (in green). The broad H-band bump (between 1.5–1.7 μm) that is seen in the spectrum of K-stars increases with decreasing effective temperature and is attributed to the H^- opacity minimum at 1.6μm (Rayner et al. 2009). In XTE J1118+480, this feature is consistent with spectral types later than K5 V. When the spectrum of a K7 V or earlier star is scaled to match the flux of XTE J1118+480 in the K-band (around 2.23 μm), the template star exceeds both the J- and the H-bands by $> 7\%$. This implies that if the donor star constitutes all the flux in the K-band conforming to previous assumptions of negligible non-stellar contribution, we would expect the donor spectral type to be later than a K7 V; otherwise some dilution should be expected. In Figure 4.5 an M1 V star scaled to match the K-band flux of XTE J1118+480 follows the broadband shape of the latter more closely if negligible non-stellar dilution is present. Estimates obtained from template star fits to photospheric absorption features in the donor star spectrum of XTE J1118+480 will be used in conjunction with the overall shape of the SED to constrain the donor spectral type.

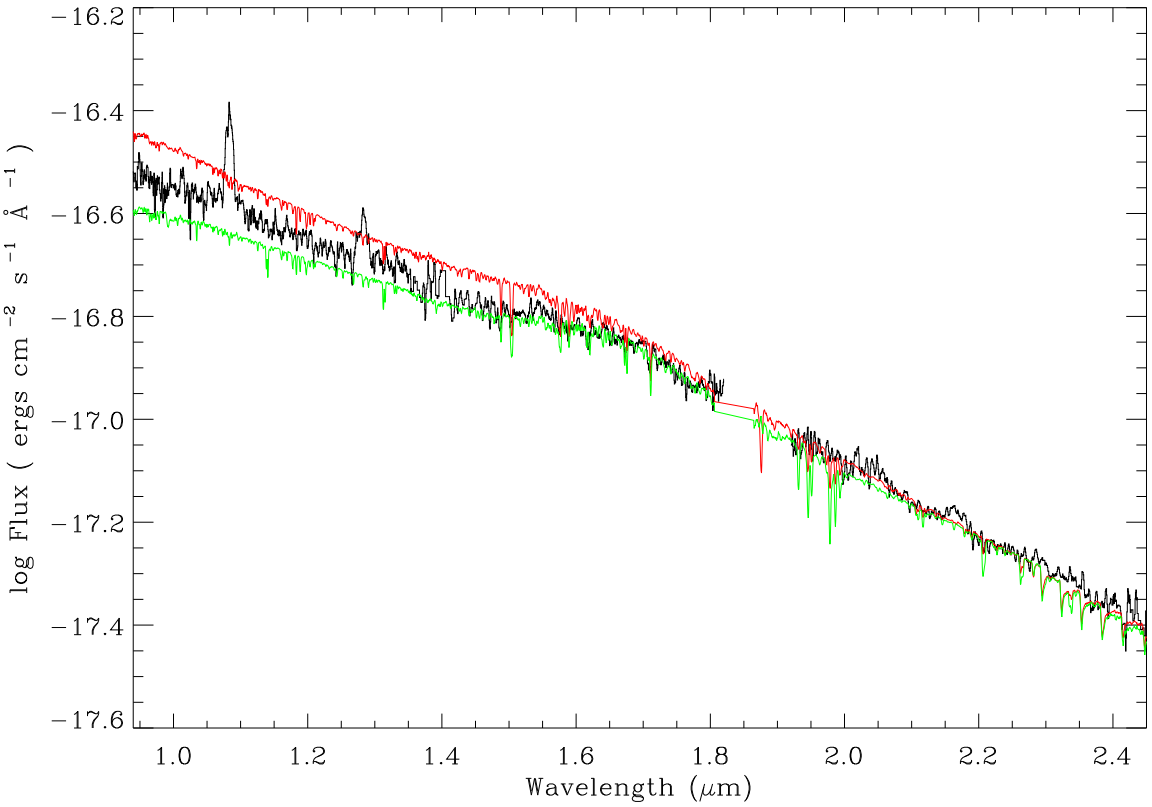

Figure 4.5: The time-averaged spectrum of XTE J1118+480 compared to the spectrum of a K5 V (in red) and M1 V (in green). The K5 V and M1 V spectra have been scaled to match the XTE J1118+480 flux near 2.23 μm. The H-band bump seen in late-type stars indicates that the donor star in XTE J1118+480 has a spectral type later than K5 V.

4.3.1.1 Field star fits to XTE J1118+480

To constrain the donor spectral type and estimate the fraction of NIR flux originating from the donor star (donor fraction, f) in XTE J1118+480, we followed the procedure outlined in Khargharia et al. (2010) and Froning et al. (2007). The normalized spectrum of the template star was subtracted from XTE J1118+480 after the former was scaled by a fraction f that was varied from 0 to 1 in steps of 0.01, and the residual was computed. The continuum points used for normalization were picked by eye and a cubic spline was fitted

through these points for normalization. The value of f that minimized the chi-squared value between the residual and the mean of the residual determined the best fit. Stars of spectral type K5 V (HD36003), K7 V (HD237903), M0/M0.5 V (HD209290) and M1 V (HD42581) were compared against the normalized spectrum of XTE J1118+480 to obtain a reliable estimate of the donor fraction. There is a disagreement in literature about the spectral type of HD209290 and hence we refer to it as M0/M0.5 V star (Rayner et al. 2009; Koen et al. 2010). The template star spectra have been obtained from the IRTF spectral library [3] .

The fit regions that were investigated in the J-, H- and K-bands for the spectral types between K5 V – M1V are listed in Table 4.2 along with the best fit donor fractions, f and χ^2_ν values. In the J-band, our fits were restricted to the region between 1.20 – 1.314 μm within which we detected features containing blends of Mg I, Si I, Fe I and Al I. However, the absorption features in this band in dwarf stars (earlier than M5 V) are intrinsically weak making it challenging to estimate the donor fraction (see, for example, spectra in Wallace et al. 2000). In the K-band, the fits to the Ca I between 1.94 – 2.00 μm are not reliable due to telluric correction residuals affecting our low S/N spectra and are therefore not taken into account for spectral type determination of the donor star. In the H-band, we fit features of Mg I, Al I and Si I over the wavelength range 1.475 – 1.73 μm. From Table 4.2, it is seen that a non-negligible contribution from non-stellar sources exists in the H-band. To constrain the spectral type of the donor star in XTE J1118+480, we used three criteria : (a) the lowest χ^2_ν values, (b) the consistency of the donor fraction computed from spectroscopy with the overall broadband spectral energy distribution in XTE J1118+480, and (c) the consistency of the H-band bump discussed in Section 4.3.1.

The χ^2_ν values are listed in Table 4.2 along with the best fit donor fractions. However, these values suffer from several systematic uncertainties that are expected in NIR ground-based spectra of faint sources. For example, uncertainties in the sky background removal;

[3] `http://irtfweb.ifa.hawaii.edu/~spex/IRTF_Spectral_Library`

Table 4.2: Donor fractions, f, with the χ^2_ν values calculated for XTE J1118+480 for K5 V - M1 V field stars.

Band	Wavelength range(μm)	Feature	f (K5 V)	χ^2_ν	f (K7 V)	χ^2_ν	f (M0.5 V)	χ^2_ν	f (M1 V)	χ^2_ν
K	**1.94 – 1.99**	Ca I [‡]	0.15	1.16	0.18	1.12	0.20	1.10	0.18	1.13
	2.203 – 2.214	Na I	0.80	0.50	0.70	0.55	0.65	0.57	0.62	0.49
H	**1.48 – 1.51**	Mg I	0.35	1.24	0.37	1.75	0.48	1.20	0.56	1.80
	1.568 – 1.60	Mg I, Si I	0.40	0.67	0.44	0.62	0.47	0.90	0.63	0.80
	1.67 – 1.68	Al I	0.39	0.68	0.39	0.66	0.30	0.62	0.40	0.73
	1.70 – 1.72	Mg I	0.55	1.16	0.60	1.08	0.65	1.13	0.70	1.12
J	**1.176 – 1.202**	Mg I, Fe I, Si I	0.63	0.47	0.65	0.44	0.68	0.55	0.69	0.46
	1.310 – 1.317	Al I	0.65	0.53	0.64	0.49	0.66	0.51	0.72	0.50

[‡]Fits may be affected due to residuals of telluric correction.

residuals from telluric correction; line blending in the absorption features affecting the donor fraction, especially for slight abundance and/or temperature mismatches between the donor and the template star; and uncertainties arising from differences in estimated (by eye) versus true continuum for spectrum normalization will affect the fit results. However, relative χ^2_ν values among the different spectral types can be used for constraining the donor spectral type because the same uncertainties are present for all the fits in the fitting procedure. The template star spectra (S/N $\sim$ 100) were obtained by the same instrument (not the same as the science data , but each other) under similar observing conditions and were fitted to the same spectrum of XTE J1118+480. An examination of the lowest χ^2_ν values for all fit regions in Table 4.2 favors K7 V – M1 V, over K5 V as the likely donor star spectral type in XTE J1118+480. However, caution should be exercised in drawing a conclusion about the donor spectral type based on the lowest χ^2_ν. These values range from 0.34 – 1.75 and are not reflective of the true uncertainty in our fits due to unaccounted-for systematic uncertainties. Since the S/N in our spectrum is low, we have adopted a different technique to properly evaluate the noise associated with the spectrum of XTE J1118+480 and its contribution to the donor fractions. The procedure for this involves "scrambling" the XTE J1118+480 spectrum and fitting the template star spectra to many such randomly 'scrambled' data in order to place robust error estimates on the best fit donor fractions. A detailed explanation can be found in Appendix A. The uncertainties calculated in this manner are shown in Table 4.3 along with the best fit donor fraction values, f, obtained from Table 4.2.

Next, we asked if the donor fractions calculated in the J-, H- and K-bands obtained from spectroscopy were consistent with the overall shape of the broadband spectral energy distribution of XTE J1118+480. To answer that question, we scaled the flux of each field star by the average donor fraction in the H-band (near 1.6 μm) obtained from Table 4.3 and computed the value by which the average flux of the field star drops below that of XTE J1118+480 in both the J- and K-bands. Less emphasis was given on obtaining a K-band match due to the fact that we only had the Na I feature to compare with and this feature is

Table 4.3: Final Donor fractions, f, with robust error estimates obtained after "scrambling" the XTE J1118+480. The errors were propagated to the average donor fraction.

Band	Wavelength range(μm)	Feature	f (K5 V)	f (K7 V)	f (M0.5 V)	f (M1 V)
K	**1.94 – 1.99**	Ca I *	0.15±.11	0.18±.14	0.20±.12	0.18±.10
	2.203 – 2.214	Na I	0.80±.15	0.70±.15	0.65±.18	0.62±.18
H	**1.48 – 1.51**	Mg I	0.37±.07	0.37±.07	0.48±.08	0.58±.09
	1.568 – 1.60	Mg I, Si I	0.40±.11	0.44±.09	0.47±.09	0.63±.10
	1.67 – 1.68	Al I	0.39 ±.12	0.39±.11	0.30±.09	0.40±.10
	1.70 – 1.72	Mg I	0.55±.09	0.60±.09	0.65±.11	0.70±.09
J	**1.176 – 1.202**	Mg I, Fe I, Si I	0.63±.10	0.65±.13	0.68±.13	0.69±.15
	1.310 – 1.317	Al I	0.65±.15	0.64±.16	0.66±.17	0.72±.18

*Donor fraction for this feature was not used in analysis.

at about the same level as the noise in the K-band. Depending on whether the corresponding drop in flux in the J-band was consistent with the average J-band donor fraction (within the bounds allowed by propagating the errors to calculate the average donor fraction) computed from Table 4.3, we could further constrain the donor spectral type. Figure 4.6 shows that when a K5 V star was scaled to 43% of the XTE J1118+480 flux at the center of the H-band, it resulted in an average flux drop of 41% in the J-band (between 1.1 – 1.3 μm) and 38% in the K-band (near 2.20 μm), inconsistent with the average donor fractions (even after accounting for the error) expected from spectroscopy in both J- and K-bands. A K7 V matches the drop in J-band flux but not in the K-band, while M0.5 V/M1 V matches both J and K-bands when their H-band fluxes were scaled to the corresponding average H-band donor fraction obtained from Table 4.3. Figure 4.7 shows the case for an M1 V star. This suggests that K7 – M1 V is the most likely range of donor spectral types in XTE J1118+480.

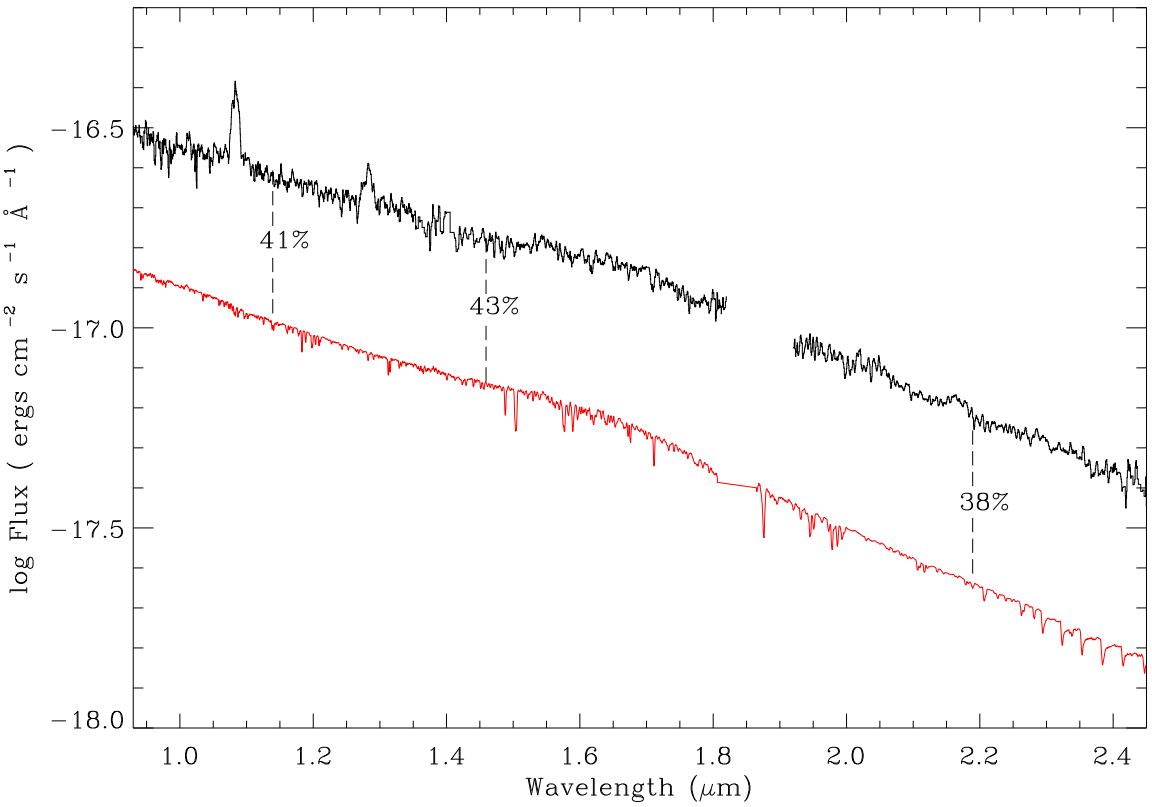

Figure 4.6: The time-averaged spectrum of XTE J1118+480 compared to the spectrum of a K5 V (in red) after the latter has been scaled to 43% of the XTE J1118+480's H-band flux. The corresponding drop in fluxes in the J- and K-bands in the K5 V star does not agree with the values expected from spectroscopy: 64%±18% in the J-band and 80%±15% in the K-band.

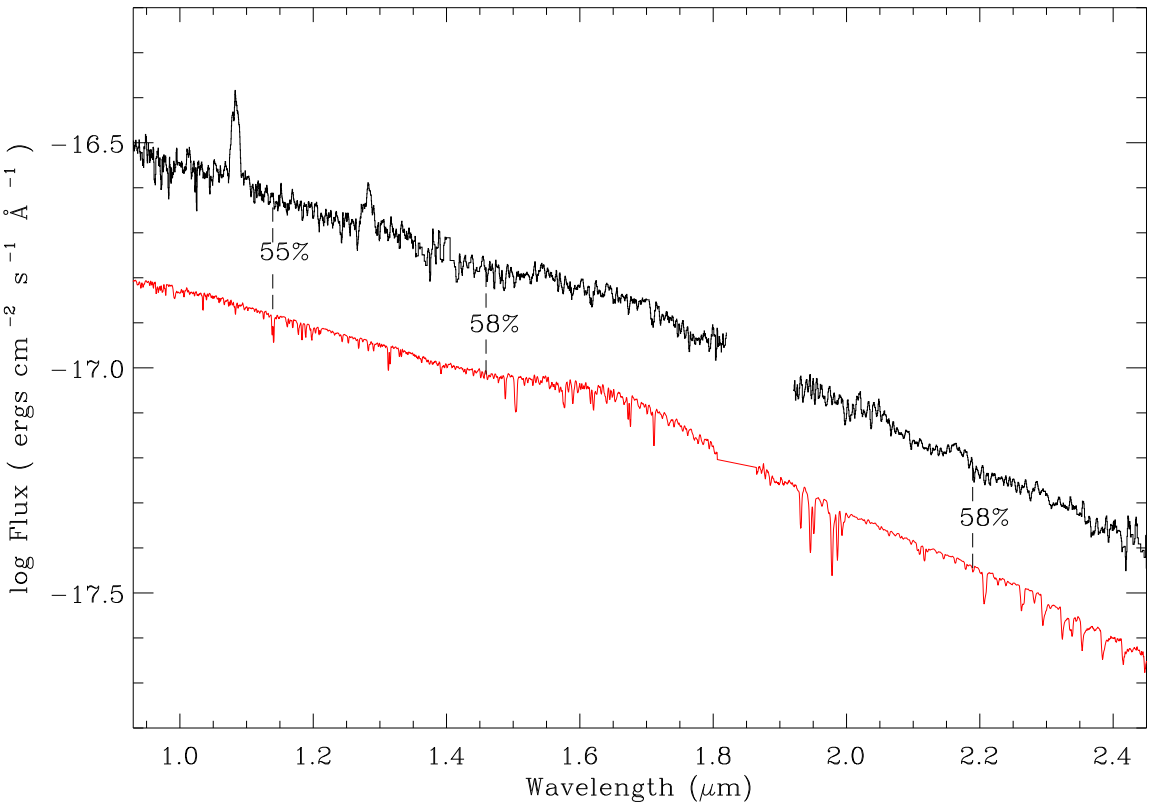

Figure 4.7: The time-averaged spectrum of XTE J1118+480 compared to the spectrum of a M1 V (in red) after the latter has been scaled to 58% of the XTE J1118+480's H-band flux. The corresponding drop in fluxes in the J- and K-bands in the M1 V star agrees with the values expected from spectroscopy: 71%±23% in the J-band and 62%±18% in the K-band.

Earlier, we found that the broad H-band bump near 1.6 μm in XTE J1118+480 was consistent with spectral types later than K5 V. By fitting absorption features of the donor star in XTE J1118+480 to various field stars we concluded that the spectral type best describing the donor star in XTE J1118+480 lies between K7 V – M1 V. This spectral range is further supported by comparing the consistency of the donor fraction obtained from spectroscopy with the shape of the overall broadband spectrum. The donor star spectral type range could not be constrained any further from our data. We have chosen to estimate the final donor

fraction by obtaining an average of best fits to multiple lines over the templates K7 – M1 V, and propagating the corresponding uncertainties accordingly from Table 4.3 rather than through the use of χ^2 statistics. This leads to a H-band donor contribution of $f = .50 \pm .32$ in the spectrum of XTE J1118+480. This result is contrary to previous assumptions of negligible dilution from other sources of flux in the near-infrared (Gelino et al. 2006). The upper panel of Figure 4.8 shows the normalized spectrum of XTE J1118+480 plotted (in black) over the normalized spectrum of a K7 V star (in red) while the lower panel shows the same comparison but with the K7 V star scaled to match the best donor fraction of 50%.

4.3.2 Photometry

Our spectroscopic observations of XTE J1118+480 were supplemented with contemporaneous light curve data. The H-band light curve of the donor star in XTE J1118+480 was obtained using the orbital ephemeris from Calvelo et al. (2009). Figure 4.9 shows the H-band light curve after the data was combined into phase bins of size $\Delta\phi = 0.03$. Each data point in this figure represents the mean of the points in the specific phase bin and the error bar in each is represented by the scatter of the points about the mean value. In cases where we did not have enough data points (< 3 points) to place a reliable error estimate on the magnitude, the error bar for that data point was changed to the value of the biggest error bar in the remainder of the phase bins. The orbital phases represent the standard convention where phase 0.0 stands for the inferior conjunction of the donor star. From the H-band light curve in Figure 4.9, we see that there is an apparent departure from the conventional ellipsoidal modulation expected from a Roche-lobe filling donor star: the maximum at phase $\phi = 0.75$ is higher than the maximum at $\phi = 0.25$.

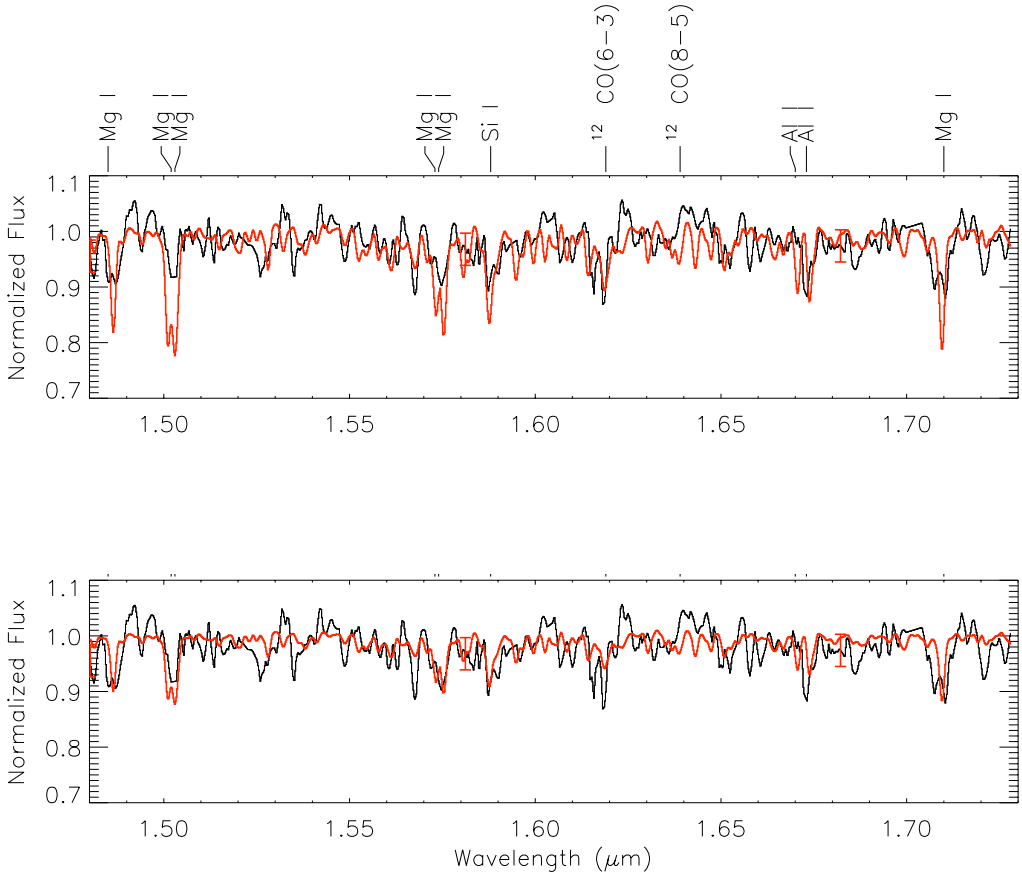

Figure 4.8: The normalized H-band spectrum of XTE J1118+480 is shown in the upper panel overplotted on a K7 V star (in red). The lower panel shows the same after the K7 V star has been normalized to the best fit fractional contribution of 0.50.

Such asymmetric modulations were detected in the quiescent J-band light curve of XTE J1118+480 obtained by Mikołajewska et al. (2005). However, Gelino et al. (2006) obtained NIR light curves of XTE J1118+480 four months prior to Mikołajewska et al. (2005) and found no asymmetries in their J-band light curve data. Typically this observed asymmetry in the light curve maxima is attributed to the emission from a bright spot in the accretion disk (Froning and Robinson 2001; Froning et al. 1999) or from a dark spot on the donor star (Gelino et al. 2001). Doppler and modulation tomography of XTE J1118+480 during

quiescence taken by Calvelo et al. (2009) revealed a well-defined hotspot but Torres et al. (2004) found no evidence of a hotspot in their Doppler tomograms. The lack of evidence for a hotspot was attributed to a significant drop in the mass transfer rate when Torres et al. (2004) obtained their data versus resumption of mass transfer when Calvelo et al. (2009) obtained their data, producing a hotspot in the Doppler maps; the system was in quiescence at both times. In the following sections, we present two simple models for fitting the observed light curve of XTE J1118+480: a) a model incorporating a donor star with constant extra flux from nonstellar sources (e.g., the accretion disk); we will refer to this component as the "constant disk flux" or f_{disk}, and b) a model incorporating a donor star and an accretion disk with a bright spot.

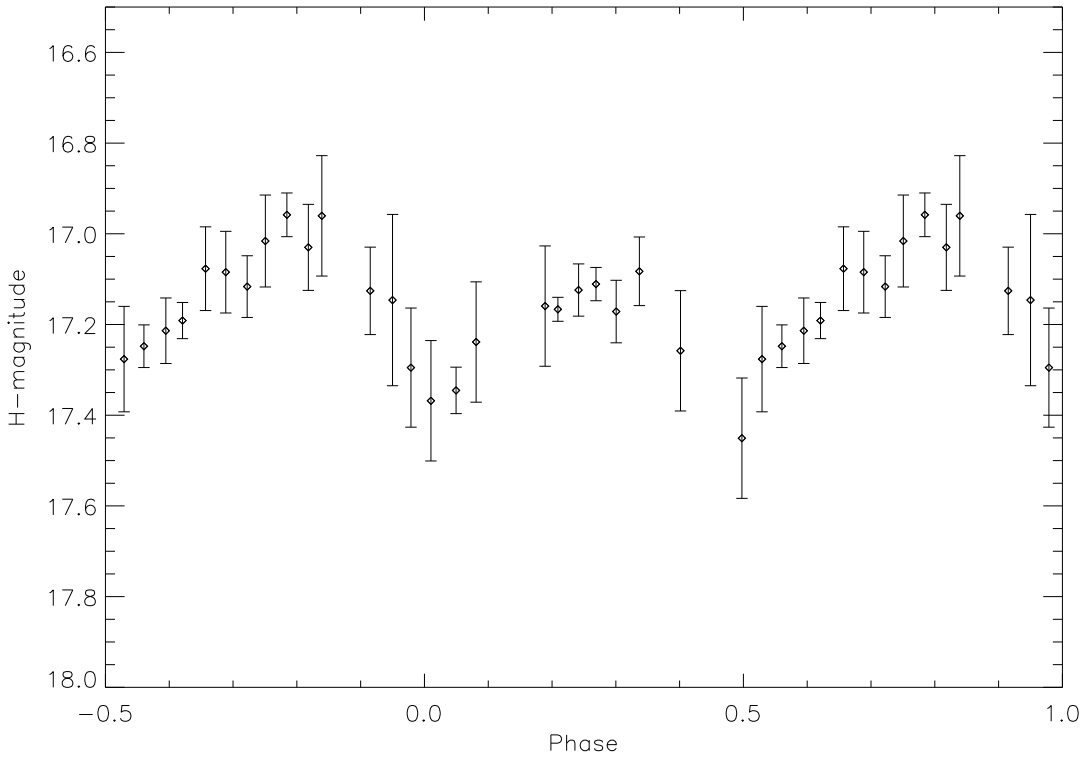

Figure 4.9: The light curve of XTE J1118+480 after binning the observed data in phase bins of 0.03. The error bars are derived from scatter about the mean in each bin. For phase bins that contained fewer than 3 points, we used the largest error bar in the rest of the bins as its error.

We modeled the H-band light curve of XTE J1118+480 with an updated version of the light curve synthesis code presented in Zhang et al. (1986) which has been used to model the light curves in several other LMXB's (Froning and Robinson 2001; Khargharia et al. 2010). This code accounts for the geometry of the binary system and then calculates the light curve by computing the temperature and intensity distribution across the surface of the Roche-lobe filling donor star and an accretion disk with a bright spot at its top and rim. It also takes into account gravity and limb darkening for each component of the X-ray binary system. Limb darkening coefficients were calculated using the square root limb darkening law applied to stellar atmospheres of late type stars (Claret et al. 1995). The best fit light

curve is obtained by minimizing the chi-squared value between the synthetic and the observed light curves. Below we discuss each model that was fitted to the observed light curve of XTE J1118+480.

4.3.2.1 Modeling the H-band light curve with a donor star and constant disk flux

In the past, NIR light curves have been modeled to determine the binary inclination contingent on the assumption that the donor star is the sole contributor to the NIR flux. Gelino et al. (2006) obtained optical and infrared photometry of the donor star in XTE J1118+480 and simultaneously fit their optical and NIR light curves with previously determined accretion disk contamination in the optical and assuming up to 8% dilution in the NIR bands to obtain a binary inclination of $68^{+2.8}_{-2}$ degrees consistent with the inclination estimate by Fitzgerald and Orosz (2003). On the other hand, the inclination of the binary in XTE J1118+480 was found by other studies to be very high: $80^{\circ} \pm 2^{\circ}$ (Wagner et al. 2001), $71^{\circ} - 82^{\circ}$ (Zurita et al. 2002) and $\sim 80^{\circ}$ (McClintock et al. 2001; Mikołajewska et al. 2005). At such high inclinations, eclipses are expected, but because of the extreme mass-ratio of this system, only a grazing eclipse will be seen, if any. In fact, previous observations of XTE J1118+480 have revealed no eclipse features (Uemura et al. 2000; Wood et al. 2000). We ran a few models to evaluate the effect of adding constant disk flux on the inclination of the binary. For modeling purposes, the donor star parameters were set as follows: $T_{eff} = 4000$ K, to reflect the average temperature from the derived spectral types; gravity darkening coefficient of 0.08, assuming that the donor has a convective envelope (Lucy 1967; Sarna 1989); limb-darkening coefficients were calculated from Claret et al. (1995). We adopted the mass ratio value obtained by Calvelo et al. (2009) which agrees with past estimates obtained by González Hernández et al. (2008), Torres et al. (2004) and Zurita et al. (2002). To avoid the extra flux from the bright spot at $\phi = 0.75$ as well as to account for the fact that the

Table 4.4: Effect of adding constant disk flux to the binary inclination in XTE J1118+480.

Disk fraction (f_{disk})	Inclination(deg)
0.00	56.0
0.05	59.0
0.10	62.0
0.15	65.0
0.20	70.0
0.25	77.0
0.30	89.0
0.35	89.0
0.40	89.0

average donor fraction calculated from spectroscopy is biased towards the phases 0.0 – 0.50 (see Section 4.2.1 for our phase coverage during spectroscopy), we modeled the light curve between phases ϕ =0.0 – 0.50 only. By allowing the constant disk fraction (f_{disk}) to vary within the limits obtained from spectroscopy, we modeled the light curve data to derive the corresponding best fit binary inclinations; these are shown in Table 4.4. Therefore, using f_{disk}=0.18 – 0.82, we find the binary inclination to lie between 68° – 89°. Figure 4.10 shows the best fit light curve ($i = 68°$) obtained by modeling the observed light curve with a donor star and for a disk light fraction of $f_{disk} = 0.18$ ($\chi^2_\nu = 0.51$). We varied the mass ratio within the limits specified in Calvelo et al. (2009) and the results were unchanged. From this, we can conclude that accounting for the constant disk flux within its uncertainty bounds obtained from spectroscopy places a lower limit on the binary inclination of $i \geq 68°$.

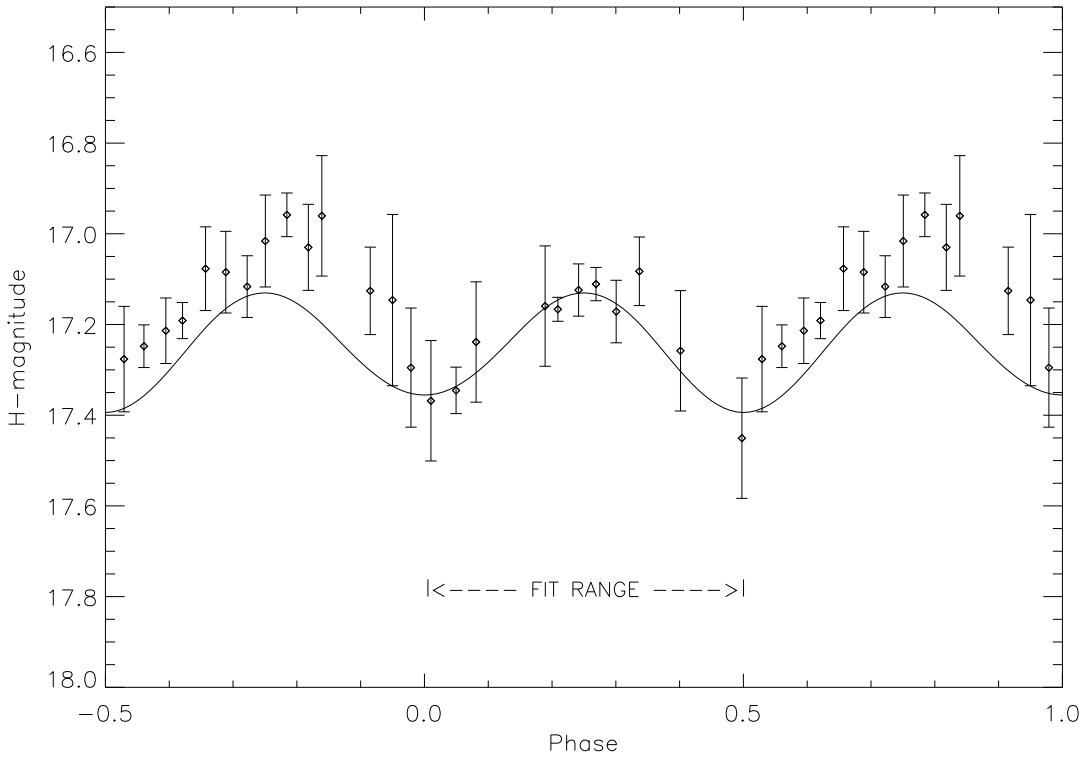

Figure 4.10: The best fit light curve obtained by modeling a donor star (fit range: ϕ= 0.0–0.5) along with a constant extra flux from the disk obtained for 68°. We find that this model cannot account for the extra light at ϕ=0.75.

4.3.2.2 Modeling the H-band light curve with a donor star and an accretion disk with a bright spot

The H-band light curve of XTE J1118+480 shows asymmetry in the maxima of the peaks at phases 0.25 and 0.75, which is often attributed to emission from a bright spot on the accretion disk. We modeled the light curve with a donor star and a cool opaque accretion disk with a bright spot on its rim. By this method, we do not attempt to constrain the physical properties associated with either the disk or the bright spot. However, we will derive a range of possible inclinations by modeling this system with reasonable estimates for the parameters associated with the accretion disk and bright spot. The donor star parameters were set at

$T_{eff} = 4000\ K$, gravity darkening co-efficient of 0.08, limb-darkening coefficients calculated from Claret et al. (1995) and mass-ratio of $q = 0.024$ as discussed in the previous section. We have found that varying these parameters had negligible effect ($\leq 1^{\circ}$ change) on the derived inclination of the system and therefore, we keep them fixed for these set of models and only vary the parameters associated with the accretion disk and the bright spot. For the accretion disk, we adopted an inner radius of $0.001R_{L_1}$ (where R_{L_1} represents the distance to the inner Lagrangian point) and an the outer disk radius of $0.75R_{L_1}$; these numbers are taken from the work done by Wren et al. (2001) and Calvelo et al. (2009). We set the flare half-angle of the disk to a small value of 1°. The bright spot was added to the rim of the disk and spans an angle in the azimuthal direction whose position ϕ_{spot} and width $\Delta\phi_{spot}$ are variable parameters in the light curve fitting model. The other input parameters are the temperature of the disk (T_{disk}) and the bright spot (T_{spot}). Both the accretion disk and the bright spot were assumed to emit as black bodies with a single temperature, with the linear-limb darkening co-efficients. We varied T_{disk} between $2500 - 4500\ K$, T_{spot} from $5000 - 20000\ K$, ϕ_{spot} from $40 - 120$ degrees, and $\Delta\phi_{spot}$ from $5 - 15$ degrees. The choice of T_{disk} was motivated by the work done in Reynolds et al. (2008) who found that thermal emission from a cool outer accretion disk ($T_{disk} \sim 2000 - 4000$K) could be used to model the excess NIR emission in the multi-wavelength SED of several XRBs (including XTE J1118+480). In Figure 4.11, we show the best fit light curve (χ^2_{ν}= 0.57) achieved for an inclination of 78° and for the fit parameters: $T_{disk} = 3000\ K$, $T_{spot} = 12000\ K$, $\phi_{spot} = 85^{\circ}$ and $\Delta\phi_{spot} = 5^{\circ}$. From an investigation of our fits over the entire range of input parameters, we find that all fits have χ^2_{ν} values between 0.60 – 0.80 and produced lower/higher T_{disk} values for correspondingly lower/higher T_{spot} values. To put this into perspective, a model with $T_{disk} = 2500\ K$ and $T_{spot} = 10000\ K$ for an inclination of $i = 74^{\circ}$ gave a comparable fit (χ^2_{ν} =.60) to a model with $T_{disk} = 4000\ K$ and $T_{spot} = 13000\ K$ for an inclination for $i = 81^{\circ}$ (χ^2_{ν} =.63). We do not attempt to set constraints on either the disk or the bright spot parameters based on the light curve models with the lowest χ^2_{ν} value. However, we find that the range of binary

inclinations satisfying the entire set of input parameters agrees with $i > 74°$. We note from Figure 4.11 that a simple model incorporating a donor star and an accretion disk with a bright spot on the rim can account for the extra flux at $\phi = 0.75$. Extensive observations of XTE J1118+480 in outburst have not found any evidence of eclipses in this system (Uemura et al. 2000; Wood et al. 2000). From our light curve models, we find that eclipse features start to emerge at $i \geq 80°$ for an accretion disk of outer radius $.75R_L$. Hence, to maintain consistency with the non-detection of X-ray eclipses in XTE J1118+480 we set an upper limit to the binary inclination of $< 80°$.

By modeling the observed light curve with a constant disk fraction obtained from spectroscopy, we can set a lower limit to the binary inclination in XTE J1118+480 as $\geq 68°$. Additionally, an upper limit on the inclination is dictated by the absence of eclipses, as $< 80°$. Hence, we have constrained the binary inclination to lie between $68° \leq i < 80°$.

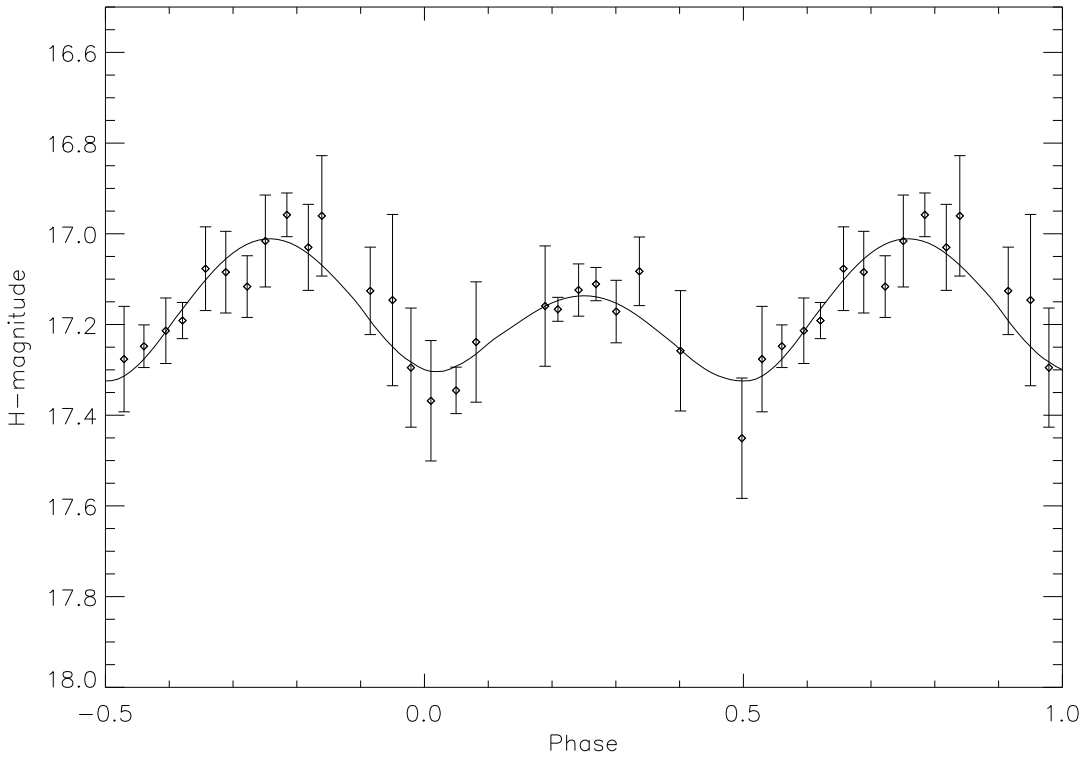

Figure 4.11: Light curve model consisting of a donor star, an accretion disk with a bright spot fitted for the full range of ϕ= -0.50 – 0.50 The best fit parameters for this model were obtained for $i = 78°$, $T_{disk} = 3000K$, $T_{spot} = 12000K$, $\phi_{spot} = 85°$, $\Delta\phi_{spot} = 5°$.

4.4 Discussion

4.4.1 Accretion disk contamination and mass of the black hole in XTE J1118+480

By performing spectroscopy of XTE J1118+480, we find that the donor star contributes a fraction $f = 0.50 \pm .32$ of the H-band flux. As we have shown in Section 4.3.2.1, the H-band light curve model results depends sensitively on the amount of extra constant non-stellar flux, which will alter the inferred binary inclination and consequently, the determined mass of the black hole. By varying the constant non-stellar (or "disk") fraction within

the limits obtained from spectroscopy while simultaneously imposing the absence of eclipse condition, we obtained a binary inclination of $68^\circ \leq i < 80^\circ$. Using the best fit orbital parameters from Calvelo et al. (2009), we determined the mass of the black hole in this system to be $6.9 < (M_{BH}/M_\odot) \leq 8.2$ for the inclination range of $68^\circ \leq i < 80^\circ$. The binary inclination obtained by us is in agreement with the values obtained previously by Frontera et al. 2001, Zurita et al. 2002, Mikołajewska et al. 2005, Khruzina et al. 2005 and Gelino et al. 2006. Accounting for any non-stellar sources of light at NIR wavelengths will raise the determined binary inclination and consequently lower the corresponding black hole mass. However, the disk fraction obtained from spectroscopy could be constrained only very broadly ($f = 0.50 \pm .32$) due to the low S/N in the spectrum of XTE J1118+480. Despite that, the binary inclination range was fairly narrow (12°) due to disk fractions $f_{disk} > 0.26$ resulting in $i > 80^\circ$ (which is beyond the limit set by the lack of eclipses in this system). The binary inclination of $68^\circ \pm 2^\circ$ obtained by Gelino et al. (2006) is within our inclination range suggesting the possibility that they may have acquired all their light curve data when the disk contribution was indeed negligible.

4.4.2 On the quiescent light curve changes in XTE J1118+480

In an extensive study of the X-ray binary A0620-00 by Cantrell et al. (2008, 2010), it was shown that the system existed in three distinct optical states even in quiescence. The authors found that a correct determination of the inclination relies on identifying the state of the system. This was found to be more important than the particular waveband where the measurements are made since non-stellar sources can be present at optical as well NIR wavelengths. XTE J1118+480 is seen to exhibit changes in the shape of its quiescent ellipsoidal light curve (compare Gelino et al. 2006 and Mikołajewska et al. 2005) similar to A0620-00. The asymmetry observed in the H-band light curve of XTE J1118+480 obtained by us is similar to that seen by Mikołajewska et al. (2005) in their J-band data. Similarly, significant changes in the quiescent infrared light curves of the black hole X-ray binary GRO

J0422+32 were also seen in two independent observations by Reynolds et al. (2007) and Gelino and Harrison (2003) even though the mean K-band magnitudes were similar on both instances. We observe the same from a comparison between our H-band light curve and that obtained by Gelino et al. (2006) in XTE J1118+480. Our contemporaneous light curve and spectral data allowed us to properly account for the disk contamination and consequently provide accurate values of inclination values and mass of the black hole.

4.4.3 Abundances of the donor star in XTE J1118+480

Enhanced N V emission and depleted C IV and O V emission in the UV spectrum of XTE J1118+480 has revealed strong evidence of CNO processed material in the accretion disk (Haswell et al. 2002). The authors suggest that XTE J1118+480 represented a later evolutionary stage of A0620-00, in which weak CO features were detected in the K-band spectrum (Froning et al. 2007). We did not detect CO features in either the K- or the H-band spectrum, supporting the result obtained by these authors. One of the uncertainties in our analysis is the assumption that the donor star in XTE J1118+480 is of solar abundance and therefore our analysis carries with it the uncertainty of fitting field stars with solar metallicity to obtain the final donor fraction. On the contrary, González Hernández et al. (2008) performed abundance analysis on the donor star spectrum by using a slightly earlier spectral type (T_{eff}=4800 K) for the donor in XTE J1118+480 and detected supersolar abundances for Mg I and Al I ([Mg/H]=0.35, [Al/H]=0.60) and other metals not used in our analysis. If Mg I were indeed to be supersolar based on the work by González Hernández et al. (2008), then the non-stellar contribution will be lower than that obtained by us. Once again, this would significantly alter our results only if it exceeds the uncertainty in the donor fraction. However, this could be further addressed by fitting a synthetic spectrum with the correct geometry representing a Roche-lobe filling donor star to the spectrum of XTE J1118+480.

4.5 Conclusion

We have obtained broadband near-infrared spectroscopy of XTE J1118+480 along with contemporaneous light curve data to accurately account for the veiling that affects determinations of the binary inclination and compact object mass. By comparing the shape of the spectral energy distribution of the combined JHK spectrum as well as individual absorption lines in our spectrum with those of field stars of known spectral type, we were able to broadly account for the fraction of NIR light contributed by the donor as $f = .50 \pm .32$. We factored this into our H-band light curve fits and obtained a binary inclination of $68^\circ \leq i < 80^\circ$. From these we obtained a robust determination of the black hole mass in XTE J1118+480 of $6.9 < (M_{BH}/M_\odot) \leq 8.2$. Our light curves combined with the non-negligible non-stellar contribution show that if XTE J1118+480 exhibits similar state changes to A0620-00, it was most probably not in "true quiescence" when our data were acquired.

Chapter 5

PSR J1903+0327: A Unique Binary Milli-Second Pulsar

5.1 Introduction

Binary pulsars are excellent systems for understanding the nature of binary star evolution and they also act as laboratories for tests of extreme physics. The milli-second pulsar (MSP), J1903+0327, was first discovered in the Arecibo L-band Feed Array pulsar survey (Cordes et al. 2006). It was soon found by Champion et al. (2008) that the MSP has a spin period of 2.5 ms and is in a highly eccentric orbit ($e = 0.44$) around what appears to be a solar-mass companion. It is atypical of MSPs to exhibit such high eccentricity or to have a main-sequence (MS) companion. Current models of stellar and binary evolution do not predict such a scenario either (Stairs 2004). This is the first and only MSP in the Galactic disk that exhibits such orbital attributes, and therein lies its uniqueness. To search for the pulsar companion, Champion et al. (2008) obtained near-infrared J-, H- and K_s images of the pulsar field with Gemini Multi-Object Spectrograph (GMOS) on Gemini-North and found a single star at the position of the pulsar with J=19.22, H=18.41 and K_s=18.03 magnitudes. They determined, from the density of stars in the field, that the probability of finding a star at the position of the pulsar was $< 3\%$. However, it was not known whether this star was a chance encounter or a distant third member in a hierarchical triple system. To confirm this association or lack thereof, Freire et al. (2011); F2011 hereafter, obtained optical spectroscopy of the possible pulsar counterpart using the FOcal Reducer and low dispersion Spectrograph (FORS2) on the European Southern Observatory's (ESO) Very Large

Telescope (VLT). They determined the spectral type of the companion to lie between an early to mid-G dwarf and from radial velocity changes, they positively confirmed the MS star's close-in association with the pulsar. It is typically seen that MSPs with spin-periods < 10 ms have white dwarfs (WD) as their companions and exhibit very circular orbits with eccentricities, $e < .001$ (Phinney 1992). To explain this inconsistency in PSR J1903+0327, Champion et al. (2008) proposed the possibility of a triple system where the pulsar is orbiting an unseen massive white dwarf (WD) of 0.9–1.1 $M_{\odot}$ while the MS star is in a much wider orbit around the MSP-WD binary and provides the eccentricity to the inner binary via the Kozai mechanism, which causes periodic exchange between inclination and eccentricity of the orbit (Kozai 1962). Recently, Portegies Zwart et al. (2011) have questioned the plausibility of the existence of such a MSP–WD–MS triple system and have pointed out several shortcomings associated with such a proposition. It should be mentioned that triple systems with eccentric orbits have been observed in the past. For example, the soft X-ray transient, 4U 2129+47 (V1727 Cyg) is a low mass X-ray binary (LMXB) with an orbital period of 5.24 hr and a third companion (F-type MS star) in an eccentric orbit of 175 days (Garcia 1989; Bothwell et al. 2008; Lin et al. 2009); similarly the cataclysmic variable EC 19314-5915 has an orbital period of 4.85 hr with a G8 V star as the outer companion (Buckley et al. 1992). An alternative scenario proposed by Champion et al. (2008) was the possibility of an exchange interaction in a globular cluster that eventually resulted in the MSP orbiting the MS star as its present companion, but the new observations of F2011 have shown this to be highly unlikely. Other formation and evolution mechanisms discussed in F2011 are summarized in Section 5.4.2. In the same section, we also discuss the results obtained from the numerical simulations by Portegies Zwart et al. (2011) to test the formation scenario of PSR J1903+0327 proposed by F2011.

Based on the observations of Champion et al. (2008) and F2011, we appear to have the unique case of a MSP in orbit around a MS star in a highly eccentric orbit in the Galactic

disk. This can prove to be of immense importance in the field of general relativity. Pulsar timing of this unique system can test alternative theories of gravity and probe the equation of state (EOS) of super-dense matter. Accurate pulsar masses already set interesting limits for the EOS of neutron star (NS) material (Freire 2009), ruling out a few softer models. Also, the rate of orbital decay of this system will constrain various scalar-tensor theories of gravity because the members of this binary system have vastly different self-gravities, (0.2 for NS and $10^{-0.6}$ for MS stars). An accurate measurement of the orbital decay of the pulsar companion accompanied by the confirmation that it is a slowly rotating solar mass MS star can constrain a significant portion of parameter space for general relativity versus scalar tensor theory. So far, the best candidate for constraining these dipole contributions consists of a 394 milli-second pulsar orbiting a WD with comparable mass in a moderately eccentric orbit (Bhat et al. 2008). In F2011, the rotational velocity of the pulsar companion could not be very tightly constrained (< 140 km s^{-1}, 3-σ). An accurate estimate of the rotational velocity of the pulsar companion is important in terms of constraining the classical contributions to the measured periastron advance of the MSP. The dominant classical contributions arise from the rotationally-induced quadrupole moment of the star and this classical spin-orbit coupling can account for 10% of the measured periastron advance for a rotational period of few days (Wex 1998).

In this paper, we present three new epochs of optical spectroscopy of the pulsar companion obtained with GMOS at Gemini-N. In Section 5.2 we describe the observations and data reduction procedures. In Section 5.3, we present a detailed analysis to confirm the results of F2011 as to the association of the pulsar companion with the MS star, determine the spectral type of the pulsar companion as accurately as possible using a combination of F2011 data along with our new spectra and constrain the rotational velocity of the pulsar companion more precisely. Section 5.4 discusses the various formation and evolution scenarios possible for this system. The result obtained on the rotational speed of the pulsar

companion has several implications in the field of general relativity which are also presented in this section. Finally, we summarize the conclusions in Section 5.5.

5.2 Observations and data reduction

Long slit ($1.0''$ slit-width), moderate resolution (R=2200) spectroscopy of the pulsar companion in the 7500–9600 Å range was performed with GMOS on Gemini North in three different observing epochs separated by 20 – 40 days. The observations took place on Aug 19, Sep 06 and Oct 05, 2010 using the EEV detector with five thirty–minute individual exposures (total of 2.5 hours on-source integration time). Wavelength calibration exposures were obtained before and after each target exposure, which were then averaged to determine a wavelength solution for that particular exposure. Wavelength solution accuracy was further checked using the sky lines in the spectrum. Additionally, a bright slowly rotating (11 $\mathrm{km} s^{-1}$) F-type star was observed before and after the target observations which served as our rotational standard star (Wolff and Simon 1997). The detector was read out with no binning, giving a resolution of 3.4 Å sampled at 0.34 Å pix^{-1}. The Gemini IRAF package for GMOS data reduction was used to reduce the data which involved the processes of bias subtraction, flat-fielding, sky-subtraction and finally, spectral extraction. No flux calibration was performed on the data. F2011 points out that a bright star located $2.3''$ from the pulsar counterpart contributes partly to the counts from the latter, complicating its extraction in their spectrum. Hence they used the optimal spectral extraction technique by Hynes (2002) to obtain the spectrum of the pulsar companion. In Figure 5.1, we show the position of the target compared to the bright source located $2.3''$ away. Upon fitting Moffat profiles to both the target and the bright object, we notice that in the better seeing conditions of the GMOS observations, the contamination caused by the bright object to the target is negligible. Additionally, we selected a narrow spatial window ($0.5''$ – $0.6''$) for spectral extraction of the target, thus further reducing any contamination from the bright source. Our final extracted spectra still has residuals from night sky lines. Furthermore, the wavelength range from

8600 — 8700 Å is affected by the broad feature in the airglow spectrum which is contributed by a blend of R- and P- branches of $O_2(0-1)$ (Broadfoot and Kendall 1968). This, along with residual night sky lines, resulted in our inability to recover the Ca II 8662 Å feature in the spectrum of the pulsar companion. In the remainder of the paper, we will focus on the wavelength region 8400 – 8600 Å where most of the prominent features reside and where our sky subtraction was best. The features in this region were identified using the line list from Cenarro et al. (2001) and the night sky lines were identified from Osterbrock et al. (1996).

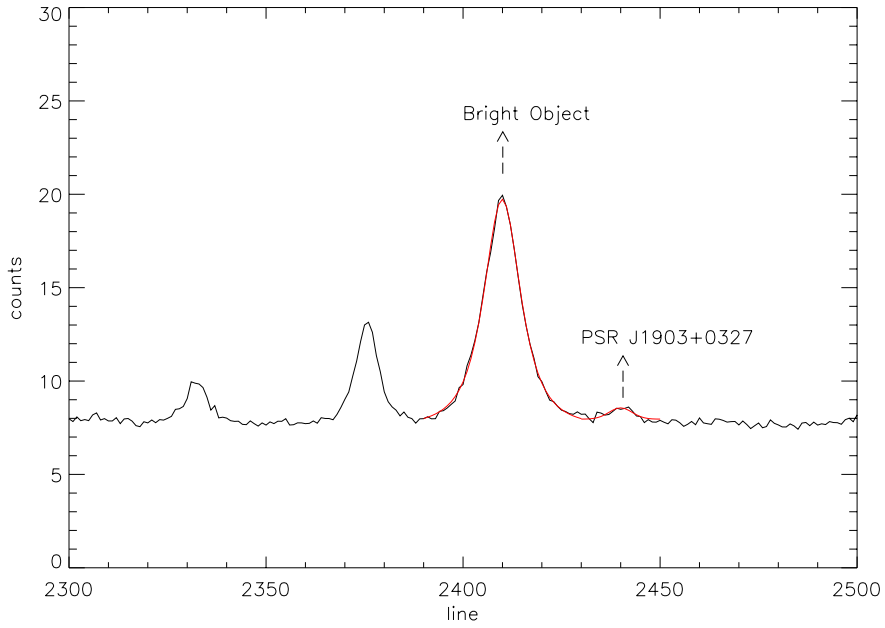

Figure 5.1: The position of the pulsar (line # 2442) and the bright object (line # 2410) 2.3″ from the pulsar is shown in the above figure for a total of 100 columns. Moffat fits to their profile indicate negligible contamination to the counts from the pulsar companion.

5.3 Analysis

In Section 5.3.1, we confirm the results of F2011 as to the association of the MS star to the pulsar by comparing the radial velocities obtained by us in three different epochs

against the radial velocity of the pulsar companion obtained by F2011. In Section 5.3.2, we constrain the spectral type of the pulsar companion by employing equivalent widths of some of the prominent absorption line features in our spectrum and comparing them against values from the literature. Finally, in Section 5.3.3, we have constrained the rotational velocity of the pulsar companion using the rotational standard star that was observed for this purpose.

5.3.1 Radial Velocity of the pulsar companion

To compute the radial velocities at each of the three epochs, we first obtained the wavelength shift in the strongest Ca II triplet feature at 8542 Å. The accuracy of the wavelength calibration was established by comparing the position of night sky lines in the spectrum of the pulsar companion against the values from Osterbrock et al. (1996). From this comparison, we found zero point offsets in the wavelength calibration of -0.31 Å, -0.25 Å and +0.15 Å for the three observation epochs respectively, which were then taken in account while computing the final radial velocities. After shifting the individual spectra by their respective wavelength offsets, we created an averaged spectrum of the pulsar companion shown in Figure 5.2. The calcium 8542 Å and the 8498 Å features are seen in the spectrum. The absorption feature at 8598 Å is at the location of the P14 line in the Paschen series. These features are present in the spectrum at each epoch. There are also possible detections of Fe I at 8514.1 Å and 8688 Å. However, considering the modest S/N ($\sim 7 - 10$) of the spectrum, we have decided to restrict our analysis to the lines : Ca II (λ8498, λ8542) and P14(λ8598). The deviation of the data points from a straight-line fit to various regions of continuum was used to assign the error on the normalized spectrum. In Figure 5.2, the location of sky line residuals have been replaced with similar continuum regions from the GMOS spectrum of the rotational standard. These locations are marked with vertical dashed lines in Figure 5.2.

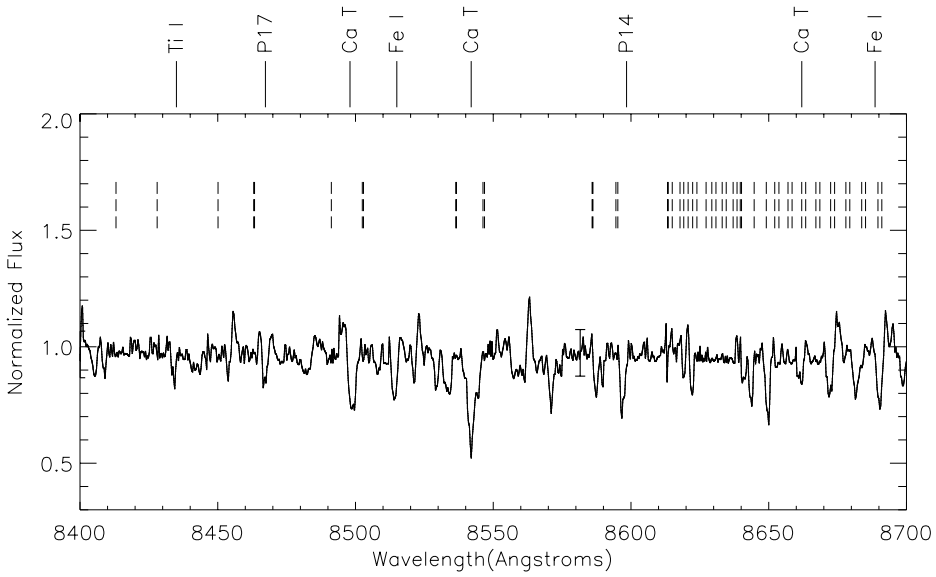

Figure 5.2: The normalized averaged spectrum of the pulsar companion is shown with representative error bars. Ca II (λ8498 and λ8542) lines are visible in the spectrum as well as the P14 line at 8598Å and Fe I at 8515Å. There are also possible detections of Ti I (8435 Å), P17 (8467 Å) and Fe I (8688.5 Å) lines but we cannot be certain due to the low S/N of the spectrum. The position of the sky lines are indicated by the vertical dashed lines. Sky lines that are too close in wavelengths to be resolved as separate lines appear as thick dark vertical lines.

To refine our estimates for the radial velocities, we cross-correlated the averaged spectrum with the individual unshifted ones at each epoch while correcting for the wavelength calibration accuracy. The cross-correlation function in each case was fitted with a Gaussian and the error was obtained by the uncertainty in the determination of the line centroid. This error was then propagated in the estimation of the radial velocities. As a result, we obtained radial velocities of $V_1 = 39.1 \pm 4.5$ km s^{-1}, $V_2 = 25.2 \pm 5.4$ km s^{-1} and $V_3 = 17.8 \pm 6.4$ km s^{-1} with respect to the solar system barycenter at the three different epochs, respectively. Figure 5.3 shows the predicted radial velocity curve of the pulsar companion (solid line), based on the orbital parameters determined from pulsar timing. Our observations confirm the result of F2011 that the optical counterpart is indeed the close-in companion to the

pulsar, orbiting it in a 95-day period. We found that the two data points from F2011 allow the eccentricity of the orbit to be as low as $e = 0.20$ while inclusion of all five data points constrain the eccentricity to $e \geq 0.36$ thereby confirming the high eccentricity independently from the optical observations. For example, Figure 5.3 shows that the radial velocity curve of the pulsar companion for an eccentricity of $e = 0.6$, mass-ratio of $R = 1.42$ and systemic velocity of $\gamma = 44.3$ km s^{-1} (dotted-dashed line) is aligned with the data points within the error bars. With five epochs of radial velocities in-hand and in agreement with the predicted reflex motion of the pulsar companion, the highly elliptical orbit of this system is confirmed for the first time. An independent estimate of the mass-ratio of 1.59 ± 0.21 is obtained by taking into consideration all five radial velocity data points. This estimate is in agreement with the result derived from radio timing. On the other hand, timing measurements cannot provide an estimate of the systemic radial velocity of the binary. With five epochs of data, we have refined this number to be $\gamma = 41.7 \pm 2.2$ km s^{-1}. However, further optical/infrared observations of the pulsar companion could be useful in placing an even tighter constraint on the radial velocity curve as predicted by the orbital eccentricity obtained from pulsar timing.

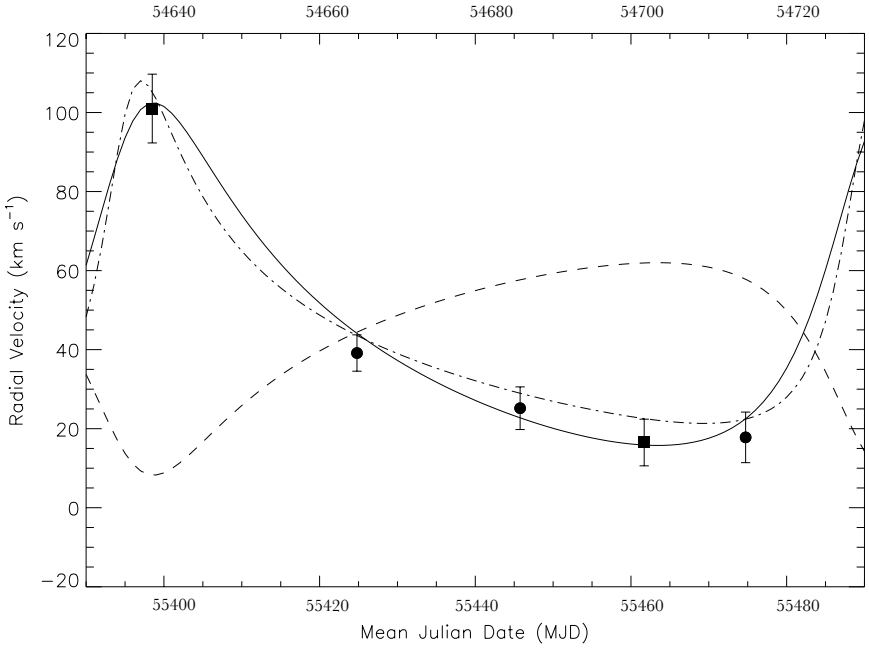

Figure 5.3: The barycentric radial velocity curve of the pulsar (dashed line) and the pulsar companion (solid line), as predicted from pulsar timing ephemeris ($e = 0.44$) in F2011. The bottom x-axis and the top x-axis are the Mean Julian Date (MJD) of observations conducted by Khargharia et al. (2012) and F2011 respectively. The data points in filled circles are the measured values of radial velocity obtained from our dataset while the two points in filled squares (near MJD 54640 and MJD 54700) from F2011 are also shown in the figure. The dotted-dashed line represents the radial velocity curve obtained for an eccentricity of $e = 0.6$, mass-ratio of $R = 1.42$ and a systemic radial velocity of $\gamma = 44.3$ km s^{-1} which lies within the error bars of the data points.

5.3.2 Spectral type of the pulsar companion

Significant work has been done in the past to use equivalent widths (EWs) of the calcium triplet as well as the Paschen lines as indicators of temperature, metallicity, and

luminosity of a star. This is the method we have employed in determining the spectral type of the pulsar companion. To this end, we have followed the works of Mallik (1994), Ginestet et al. (1994), Jones et al. (1984), Idiart et al. (1997) and Diaz et al. (1989). The spectral features along with the line windows used for calculation of EWs and our results are shown in Tables 5.1 and 5.2. EWs were calculated from the the averaged, normalized spectrum and errors on EW values were obtained by choosing different continuum points for normalization ($\pm 1\sigma$). Since the Ca II line at 8662 Å was not recovered in our spectrum, we have used the EW of this feature from the normalized spectrum of F2011 wherever applicable (see Table 5.2). Furthermore, we have reanalyzed the data of F2011 using the two well-detected Ca II features at 8542 Å and 8662 Å shown in Table 5.3. This was done to ascertain if tighter constraints could be placed on the spectral type of the pulsar companion from their data. It should be noted that the error in the EWs obtained from their already normalized spectrum is based on the error in the Gaussian fit to the feature rather than on continuum placement.

Table 5.1: Equivalent Width Analysis; comparison with Mallik (1994)

Feature	Integration limits ($\AA$)	Equivalent width($\AA$)
CaT 8498	8495 – 8501	0.61 ± 0.27
CaT 8542	8535 – 8550	1.70 ± 0.74

Note: Table of EWs for comparison with the work by Mallik (1994)

A summary of our conclusions from various references are shown in Table 5.4. The sum of EWs of the calcium triplet is a robust indication of the luminosity class and following all the references cited above, the pulsar companion clearly belongs to a luminosity class 'V'. It is a determination of the temperature that poses a greater challenge. Using the EWs of the calcium triplet alone does not constrain the spectral type any tighter than between F5 – G5 (see Table 5.4). On the other hand, from Ginestet et al. (1994), the non–zero EW of the

Table 5.2: Equivalent Width Analysis; comparison with Ginestet et al. (1994), Jones et al. (1984), Idiart et al. (1997) and Garcia-Vargas et al. (1998)

Feature	Integration limits ($\AA$)	Equivalent width($\AA$)
CaT 8498	8488 – 8510	1.17 ± 0.50
CaT 8542	8530 – 8556	2.32 ± 0.70
CaT 8662	8652 – 8672	1.36 ± 0.15*
P14 8598	8585 – 8605	.70 ± .50

Note: Table of EWs for comparison with the work by Ginestet et al. (1994), Jones et al. (1984), Idiart et al. (1997) and Garcia-Vargas et al. (1998)

*Data for this absorption feature was used from Freire et al. (2011)

Table 5.3: Equivalent Width Analysis; comparison with Diaz et al. (1989)

Feature	Integration limits ($\AA$)	Equivalent width($\AA$)
CaT 8542	8527 – 8557	2.40 ± 0.17
CaT 8662	8647 – 8677	1.32 ± 0.15
P14 8598	8585 – 8605	.11 ± .07

Note: Table of EWs for comparison with the work by Diaz et al. (1989). The line window for P14 is used from Table 5.2. All other line windows are from Diaz et al. (1989). The data for computation of the above EWs is obtained from Figure 2 of Freire et al. (2011)

†λ8662 feature was used from F2011

*both features were used from the data of F2011

P14 line restricts the spectral type to G0 or earlier. Our confidence in the P14 detection is supported by the fact that we observe this feature in all three epochs of data with the same wavelength shift as the calcium lines at 8498 Å and 8542 Å. Taking this into account, we conclude that the spectral type of the pulsar companion lies between F5 V – G0 V. The last column in Table 5.4 summarizes the metallicity obtained for the pulsar companion from each of the references. While it is useful, we do not attempt to draw any significant conclusion from it since the metallicity results are limited by the uncertainty in the spectral type.

F2011 determined the spectral type of the pulsar companion by comparing their averaged spectrum with synthetic spectra and obtained a temperature of $T_{eff} = 5825 \pm 200K$ and a surface gravity of ≥ 4.0 cm s^{-1}. Their analysis points to a star roughly of spectral type G0 – G5 V (Ali et al. 1995). However, from an equivalent width analysis of the Ca II features at 8542 Å and 8662 Å obtained from their data, we can conclude only that the star has a spectral type between F5 V – G5 V. But we also note that they appeared to have detected P14 as we do although at the low signal-to-noise based on our own measurement (see Table 5.4), constraining the spectral type to G0 or earlier. There is a slight mismatch between our conclusion and F2011 regarding the spectral type of the pulsar companion (F5 V – G0 V vs G0 V – G5 V) . However, the detection of Paschen P14 line in all three epochs of our data and that of F2011 requires a spectral type G0 or earlier. Taking both studies into consideration, G0 V appears to best describe the spectral type of the pulsar companion. This also matches the prediction of the companion's mass of 1.667 $M_\odot$ from pulsar timing (F2011).

5.3.3 Rotational velocity of the companion star

We observed a bright rotational standard star (HD 176095) with GMOS at each epoch before and after our target observations. The rotational standard star is an isolated, slowly rotating (11 kms^{-1}) late F type star (Wolff and Simon 1997). Figure 5.4 shows the spectrum of the pulsar counterpart plotted over the spectrum of the rotational standard (in red).

Table 5.4: Summary of Results from Equivalent Widths Comparison

Reference	Feature used	Luminosity Class	$[Fe/H]$	Spectral Type
Mallik (1994)	CaT(λ8498+λ8542)	IV/V	-0.3 < $[Fe/H]$ <0.2	F5 – G5
Ginestet et al. (1994)	Ca II(λ8542), Ca II(λ8542), P14 (λ8498)	—-	—-	F2 – G0
Ginestet et al. (1994)	CaT(λ8498+λ8542+λ8662)	V	—-	—†
Jones et al. (1984)	CaT(λ8498+λ8542+λ8662)	V	—-	F5 – G7†
Idiart et al. (1997)	CaT(λ8498+λ8542+λ8662)	—	-0.6≤ $[Fe/H]$ ≤0.2	—†
Diaz et al. (1989)	CaT(λ8542+λ8662)	V	-0.4 ≤ $[Fe/H]$ <0.2	F5 – G5*

Note: Summary of results using the CaT features from our data and F2011.

$^{\dagger}\lambda$8662 feature was used from F2011

*both features were used from the data of F2011

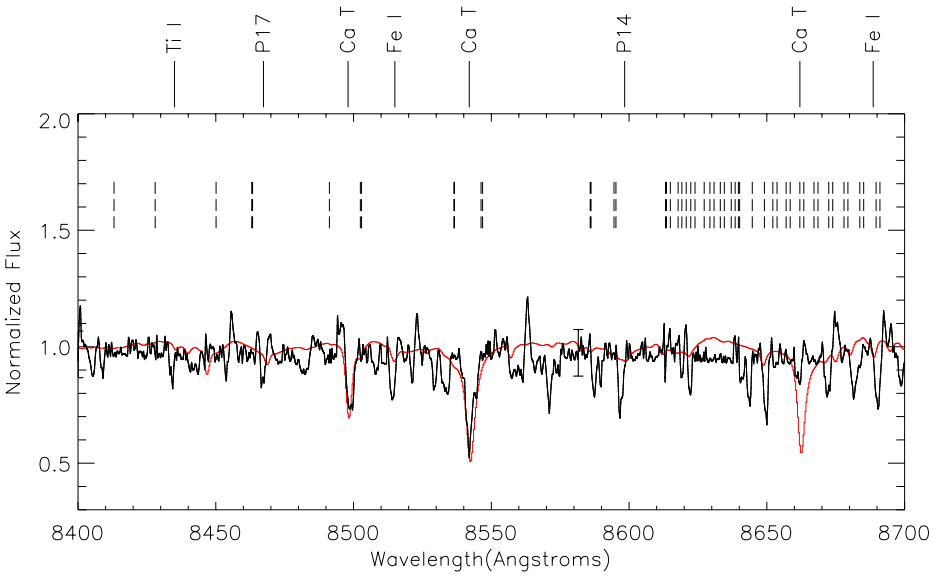

Figure 5.4: The normalized and averaged spectrum of the pulsar companion is shown in the figure compared to the normalized rotational velocity standard star spectrum (in red). The location of the sky lines are marked in vertical dashed lines.

At a spectral resolution of 136 km s^{-1}, the effect of broadening from a star rotating at 11 km s^{-1} cannot be detected. The calcium lines in solar-like stars are often broadened by collisional or pressure effects in the star's atmosphere (Smith and Drake 1987). From the spectrum of the pulsar companion, we find that the FWHM of the Fe I feature at 8515 Å, which is insensitive to pressure broadening, is similar to the FWHM of an arc lamp line, indicating that the pulsar companion is not rotating at a speed higher than the instrumental resolution. Therefore, an upper limit on the rotational velocity of the pulsar companion can be set by finding the minimum broadening that is detectable at the resolution of our instrument using cross-correlation techniques. From Tonry and Davis (1979) and Bailer-Jones (2004), the measured width (FWHM) of the cross-correlation function (CCF) can be expressed as

$$\sigma^2_{meas} = \sigma^2_{rot} + \sigma^2_{nat} + 2\sigma^2_{inst} \tag{5.1}$$

where σ_{rot} is the rotational broadening, σ_{nat} is the intrinsic broadening and σ_{inst} is the instrumental broadening. Following the argument made in Bailer-Jones (2004), σ_{rot} can only be detected if it exceeds $\sqrt{(2)}\sigma_{inst}$, assuming that σ_{nat} is negligible. Also, the full width of a rotational profile is contributed equally by both the approaching and the receding limb of the star and hence corresponds to twice the rotational velocity. Theoretically, we should be able to detect a minimum rotational velocity of $v_{rot} \sin i = \sqrt{(2)}(\sigma_{inst}/2)$ (Bailer-Jones 2004).

To test that, we obtained the autocorrelation function (ACF) of the rotational standard star separately in the wavelength ranges 8000 – 8450 Å and 8670 – 8800 Å . These regions mostly comprise the Fe I, Mg I and Ti I features while excluding the pressure sensitive calcium features. The average of the FWHMs of these two wavelength regions on either side of the calcium triplet was used as a measure of σ_{meas}. We then artificially broadened the spectrum of the rotational standard in steps of 3 km s^{-1} and cross-correlated the broadened spectrum with the original un-broadened one until a measurable difference was noticed in the CCF. From Equation 5.1, $\sigma^2_{meas} = 2\sigma^2_{inst}$ (for the ACF) and $\sigma^2_{meas} = \sigma^2_{rot} + 2\sigma^2_{inst}$ (for the CCF) and subtraction of one from the other gives σ_{rot}. We determined FWHMs of the ACF and the CCFs by fitting them with Gaussian profiles. A measurable difference in the CCF was obtained when the rotational standard star spectrum was broadened by $\sigma_{rot} =$ 132 km s^{-1}. Hence, the minimum detectable $v_{rot} \sin i$ at our instrumental resolution is 66 km s^{-1}. This value is close to the theoretical minimum detectable rotational speed of 96 km s^{-1} (=136 $\times$ $\sqrt{2}$ /2), obtained from the argument in Bailer-Jones (2004). Therefore, these observations constrain the pulsar companion's rotational speed to $\leq$ 66 km s^{-1}. Our constraint on the rotational velocity of the pulsar companion is a factor of $\sim$ 2 less than the value quoted in F2011.

5.4 Discussion

From our analysis, we have confirmed that the the observed star in the vicinity of the MSP is indeed its companion, orbiting it in a highly elliptical 95-day orbit as predicted from pulsar timing. From the EWs of the calcium triplet and the P14 feature, we constrain the spectral type of the star to lie between F5 – G0 V. Our detection of the hydrogen P14 feature in all three epochs showing the same wavelength shift as the calcium lines places the spectral type very close to the G0 V predicted by pulsar timing. Additionally, we have proven that the companion is rotating slowly with an upper limit of $\leq$66 km s^{-1}. In this section, we will discuss the implication of our result in two areas: constraining evolution scenarios of this unique system and using this system as an astrophysical laboratory for tests of general relativity.

5.4.1 Implications for General Relativity

The present analysis should allow us to constrain the classical spin-orbit contribution to the measured rate for the periastron advance: $\dot{\omega}_o = 86.38 \pm 0.08$ arcsecond century^{-1}. This is because the above contribution arises from the rotationally induced quadrupolar moment of the main-sequence companion in our binary pulsar and in what follows we provide few estimates for $\dot{\omega}_{SO}$. Using equation (79) in Wex (1998), we obtain a maximum value for the apsidal motion due to classical spin-orbit coupling to be $\dot{\omega}_{SO} \sim 7.6 \times 10^4 \times J_2$ arcsecond century^{-1}, where J_2 is the quadrupolar moment of companion star that we observed. If we let J_2 take a value close to that for the Sun ($J_{2\odot} \sim 1.7 \times 10^{-7}$), we get $\dot{\omega}_{SO} \sim 0.013$ arcsecond century^{-1} and this is roughly an order of magnitude smaller than the measurement uncertainty in $\dot{\omega}_o$(F2011). However, the fact that J_2 is proportional to the square of the angular velocity of the star's proper rotation implies that we may use $J_2 \sim J_{2\odot} \times v_{rot}^2/v_\odot^2$, where v_{rot} stands for the rotational velocity of the companion and we let $v_\odot \sim 2$ km s^{-1}. Therefore, we can provide few constraints for $\dot{\omega}_{SO}$ contributions to $\dot{\omega}_o$.

If we allow the spin axis of the star to be parallel to the orbital angular momentum of the binary, we have $v_{rot} \sim 66$ km s^{-1} which leads to $\dot{\omega}_{SO} \sim 14$ arcsecond century^{-1}. This is even substantially higher than the 2.3 arcsecond century^{-1} upper bound on the spin-orbit contributions to the apsidal motion that was obtained by treating general relativity to be the correct theory and using the minimum total mass compatible with the measurements of three relativistic observables (F2011). Interestingly, the fact that we have restricted the spectral type of the companion between an F5V – G0 V implies that v_{rot} may be in the range $12 - 25$ km s^{-1} (Tassoul 2007). These rotational velocity bounds lead to two estimates for $\dot{\omega}_{SO}$: 0.5 and 2 arcsecond century^{-1} respectively. These are also higher than the present measurement error in $\dot{\omega}_o$ indicating that it will be rather difficult to perform a test for general relativity using the available measurements of the three post-Keplerian parameters (F2011).

Our 8 meter spectra were taken under good to excellent conditions and yet have a relatively modest signal to noise at a resolution of R=2200 which is still $\sim$ 7–8 times poorer than what we need, to achieve a constraint of less than 10 km s^{-1} on $v_{rot} \sin i$. The lines which are unaffected by pressure broadening in the star atmosphere are too weak to be detected clearly at the current resolution and S/N and would require much better signal-to-noise to be confidently detected. Therefore, employing the agreement of the three different post-Keplerian parameters to perform a test of general relativity is not plausible at the current time.

5.4.2 Constraining evolutionary scenarios for the pulsar system

The detection of a MS star as the companion to the pulsar and the confirmation of a highly elliptical orbit raises various questions on the origin of this system while eliminating some other hypotheses. For example, Champion et al. (2008) considered the possibility of a triple system where the pulsar is orbiting an unseen white dwarf (0.9 – $1.1 M_{\odot}$) in a 95-day orbital period while the MS star happens to be in a longer period that drives the eccentricity of the system by the Kozai mechanism (Kozai 1962). Since we have established that the

MS star orbits the pulsar in a 95-day orbital period, the triple system hypothesis can be ruled out. Additionally, Portegies Zwart et al. (2011) have pointed out that the hypothesis of a MSP–WD–MS triple system is precluded by the fact that the observed change in the eccentricity of this system is three orders of magnitude smaller than that predicted via the Kozai mechanism (Gopakumar et al. 2009) .

Champion et al. (2008) also discuss the possibility of an exchange interaction in a dense stellar environment that might have brought the MS star to orbit the pulsar in a 95-day period. In F2011, the probability of this was found to be negligible. One of the parameters used in their simulation is the systemic radial velocity, γ, of the binary. With five epochs of radial velocity data, we have now refined this number to be $\gamma = 41.7 \pm 2.2$ km s^{-1}. Reinvestigating the exchange interaction scenario with the new improved systemic velocity estimate could be helpful in constraining any effects from a supernova kick that may have occurred in this system. This would be helpful in readdressing the original proposition by Champion et al. (2008) where the system may have been formed in a dense stellar environment but was eventually ejected via recoil during the exchange interaction.

F2011 also find that the pulsar has been recycled or spun-up to milli-second speeds (due to mass-transfer from a past, accreting X-ray binary phase) but show that the current MS star is unlikely to have played the role of the donor star responsible for its recycling. To answer the question of how the pulsar was spun-up and what happened to the donor star, F2011 investigated another triple system scenario. They considered a triple system wherein the outer companion (the present MS star) started out in a much wider orbit around the inner binary, which consisted of two more massive MS stars in a shorter orbital period. In their scenario, the more massive star in the inner binary evolves into a red supergiant phase and then engulfs the companion into a common envelope phase. As the orbit of the inner binary decays, it will release orbital energy sufficient enough to leave a much closer binary consisting of a He-core and an almost unaffected MS star. Meanwhile, if the outer star in the triple system is close enough, it could be engulfed by the expanding envelope of the inner

binary as well, which will cause it to spiral in and result in a much closer triple system. Once the He-core explodes in a supernova, we are left with an inner Low-Mass/Intermediate-Mass X-ray Binary (LMXB/IMXB) and an outer MS star. The NS is then spun up to milli-second periods by the donor star, which has filled its Roche-lobe by this time. As mass transfer continues from the donor to the NS, the orbit of the inner binary in the triple will widen to some extent and will end in a chaotic three-body interaction. This will result in expulsion of the less massive star from the system, eventually leaving the MSP in a tighter and eccentric orbit around the MS star (the initial outer body in the triple system). F2011 have also discussed in less detail several alternative scenarios for the formation and evolution of the system. All of these scenarios start out with the system as part of a triple and then invoke different dynamics that transpires after the common envelope phase, leading to the system as we see it now. However, thorough numerical simulations are necessary to provide more insight into the formation and evolution of these systems in a non-deterministic way.

Recently, Portegies Zwart et al. (2011) performed detailed numerical analysis to test the formation scenario presented in F2011. They start out with a stable LMXB ($P_{orb} < 1.0$ d) with a MS star in a wide and possibly eccentric outer orbit. They have shown from their simulations that as mass transfer starts in the inner binary and as the orbit of the inner binary widens, the system becomes unstable. Depending on the exact configuration of the system at this point, each one of the three components in this triple system could be ejected. Specifically, they found that a stable hierarchical triple consisting of an inner binary with component masses of 9–13 $M_{\odot}$ and 0.8 – 2.0 $M_{\odot}$, separated by $\geq 200R_{\odot}$ and an outer MS star with mass $< 2M_{\odot}$ and having a semi-major axis $> 560R_{\odot}$, could eventually result in the formation of a system like PSR J1903+0327. Even though the chances of passing through the various chain of events were found to be low, the result matches with what we see in PSR J1903+0327. Portegies Zwart et al. (2011) were also able to describe an evolution scenario for the soft X-ray transient 4U 2129+47 (V1727 Cyg) and the cataclysmic variable, EC 19314-5915, we noted before in Section 5.1. Additionally, they concluded that systems like

PSR J1903+0327 have a birthrate of less than 3% compared to the Galactic LMXB's and 10 times less than all MSPs. Thus the probability for this formation scenario happening, is not large, but it is also not nil. Their model predicts tens to hundreds of systems similar to PSR J1903+0327 existing in our Galaxy and raises the question of why no system like this has been found prior to PSR J1903+0327.

In another independent work, Liu and Li (2009) consider that PSR J1903+0327 started out as a binary system but during the supernova (SN) explosion that produced the pulsar, a fall-back disk was formed around the newborn NS. Accretion started from the disk onto the NS, which spun it up to milli-second speeds. Meanwhile the high eccentricity was considered to be a consequence of the SN explosion that produced the NS. Liu and Li (2009) mention that if this system was undisrupted, it could maintain this eccentricity for $\geq 10^{10}$ yr. One of the uncertainties mentioned in their work is whether the fall-back material would have enough angular momentum to produce the disk. This calls for an unusual SN-fallback history to explain the very short period (2.5 ms) of PSR J1903+0327. In order for the fallback disk scenario to work, it requires the companion of the pulsar to be $\leq (1-2) \times 10^9$ yr. From our work as well as from F2011, we find the MS star to be older than what is required for the fallback disk scenario to work.

5.5 Conclusion

By obtaining new spectroscopy with GMOS at Gemini-N, we have confirmed the results of F2011 as to the positive identification of the MS star as the close-in pulsar companion. Radial velocities are now in-hand for 5 epochs and the predicted radial velocity curve obtained from pulsar timing is confirmed. The highly eccentric orbit is confirmed as well. Additionally, we obtained estimates for the mass-ratio of $R = 1.59 \pm 0.21$ and the systemic radial velocity of the binary of $\gamma = 41.7 \pm 2.2$ km s^{-1}. These refined estimates are important in the context of explaining the origin of this system. We have determined the spectral type of pulsar companion to lie quite close to G0 V, from an analysis with our data and a reanalysis of

F2011 data. Also, we have constrained the rotational velocity of the pulsar companion as $<$ 66 kms^{-1}. With the present estimate of the $v_{rot} \sin i$, it will be difficult to perform a test for general relativity. Radio pulsar timing can lead to better constraints on General Relativity in comparison to scalar tensor theories and should be pursued over the next few years. We have also noted that the evolutionary scenario possible for the formation and evolution of this unique pulsar system is best described by the recent numerical simulations of Portegies Zwart et al. (2011). Starting with a stable hierarchical triple system consisting of an inner binary with component masses of 9–13 $M_{\odot}$ and 0.8 – 2.0 $M_{\odot}$, separated by $\geq 200R_{\odot}$ and an outer main sequence star with mass $< 2M_{\odot}$ and having a semi-major axis $> 560R_{\odot}$, numerical simulations were able to replicate the formation and evolution of a system like PSR J1903+0327.

Chapter 6

Characterization of the Hawaii-1RG Near-Infrared Array

6.1 Introduction

Infrared arrays (or detectors) were introduced into astronomy in the mid-to-late 1980's. A basic summary of the features of these devices is presented in McLean (1993). Infrared detector arrays operating from $\sim 1\mu$m to 120 μm, are "hybrid" structures containing two slabs of semi-conductor material that are bonded to each other. The thin upper slab is made of IR sensitive material (usually HgCdTe or InSb) and is organized into a grid of individual pixels each of which contains a photodiode. Between the individual diodes are narrow regions of dead space formed by insulating material acting as barriers between the diodes. The lower slab (made of silicon) is also divided into the same number of pixels and each one of them consists of a silicon field-effect transistor (FET) that acts like a "buffer" to the charge that is collected on each pixel on the detector. In a hybrid array, each pixel unit is a detector in itself containing its own charge storage site and the read-out circuitry. The entire structure is referred to as the Focal Plane Array (FPA). Infrared photons landing on the surface of the detector at a certain pixel will produce an electron-hole pair which is quickly separated by the electric field produced by the reverse-biased pn junction in the detector material creating a depletion region that effectively acts like a capacitor. Due to migration of photon generated electrons to the n-type region, the capacitor voltage will change from its initial reverse-bias value. This change in voltage is then transmitted to the silicon FET which in turn communicates this change to one or more of the output lines. IR arrays can be read

out non-destructively such that while the charge at a certain pixel is being read, the charge in the neighboring pixels remains undisturbed, allowing the charge in that pixel to be read again later.

6.2 Noise sources in near-infrared observations

For an infrared observation, the sources that contribute to the overall noise can be broadly classified into a) external and b) internal noise. The external noise comprises photon noise from the source as well as from the sky background. The internal noise consists of dark current due to thermal electrons which increases linearly with exposure time as well as read noise (McLean 2008). The read noise arises from the readout electronics every time the array is read out and is independent of time. The read noise can be thought of as random fluctuations in voltages which are added to the true signal, digitized, and converted to an equivalent number of electrons. The signal to noise equation for a single infrared exposure (for a single pixel) takes the following form (McLean 2008):

$$S/N = \frac{S_E \times \sqrt{t}}{\sqrt{S_E + B_E + D_E + \sigma^2_{read_E}/t}} \tag{6.1}$$

where,

S_E = Total source signal in electrons.

σ_{read_E} = Read noise in electrons.

D_E = Dark current in electrons.

B_E = Sky background in electrons.

t = Exposure time.

For near-infrared observations, the main challenge is presented by the high sky background. Since the objects under study are typically fainter than the background, B_E dominates all other terms in the denominator in Equation 6.1. The S/N equation then takes the form $S/N = \frac{S_E \times \sqrt{t}}{\sqrt{B_E}} \propto \sqrt{t}$. Therefore, exposure times for near-infrared observations are calculated bearing in mind the bright and variable sky background. Individual near-infrared exposure times are of shorter durations and the telescope of is often "nodded" or "dithered" to obtain frequent samples of the sky on the same pixel locations as the source to be subtracted from images. Dithering also helps in removal of bad detector pixels when the individual exposures are median combined.

6.3 System gain

The photo-electrons collected at every pixel on the array are converted to a voltage value proportional to their number. This voltage value is then converted to a corresponding digital value which forms the raw data. The raw data are expressed in analog-to-digital units (ADU) or data numbers (DN). The constant of proportionality linking the DN with the number of photo-electrons is traditionally called the system gain and is expressed in units of e^-/ADU. To obtain the relation between the system gain and read noise, let us first define the following quantities:

σ_{total_E} = Total noise in electrons.

σ_{read_E} = Read noise in electrons.

σ_{S_E} = Source noise in electrons.

σ_{total_C} = Total noise in counts.

σ_{read_C} = Read noise in counts.

S_E = Signal in electrons.

S_C = Signal in counts.

g = gain in e^-/ADU

The signal and noise in "electrons" are simply related to their corresponding quantities in "counts" by the system gain. In particular, we have:

$$\begin{aligned} \sigma_{read_E/source_E/total_E} &= g \times \sigma_{read_C/source_C/total_C} \\ S_E &= g \times S_C \end{aligned}$$

Also since the source noise follows Poisson statistics, we have:

$$\sigma_{S_E} = \sqrt{S_E}$$

Since the noise sources are independent, they add in quadrature. Hence, we have:

$$\sigma^2_{total_E} = \sigma^2_{read_E} + \sigma^2_{S_E} \tag{6.2}$$

$$g^2\sigma^2_{total_C} = g^2\sigma^2_{read_C} + g \times S_C$$

$$\sigma^2_{total_C} = \sigma^2_{read_C} + (1/g) \times S_C \tag{6.3}$$

Equation 6.3 is analogous to a straight line equation where $1/g$ represents the slope of the line. The term $\sigma^2_{read_C}$ is the intercept and is independent of the exposure time. To measure the gain of the system, we plot the variance of the total counts vs. the observed signal (in counts) for a series of flat-field illumination images and fit a straight line through these data points to obtain the slope, which is a measure of the system gain. Generally, an average value of gain is computed for different regions on the detector to account for the fact that the gain may not be constant throughout the detector.

6.4 Read noise

The read noise of an infrared array is the noise that originates in the read-out electronics and is introduced into the system every time the array is read out. Read noise is a

constant and is independent of the exposure time. The process of Fowler sampling which incorporates multiple non-destructive reads in IR arrays, is often employed to reduce the read noise (Fowler and Gatley 1990). The number of Fowler samples (NFS) is the number of non-destructive reads requested by the user. In the tests that we conducted, the array was read non-destructively in the correlated double sampling mode (CDS or NFS = 1). The CDS mode operates in the following way: at the start of request for an exposure, the array is cleared pixel by pixel until the entire array is reset. This is followed by reading the array which marks the start of the exposure time (t_{exp}) requested by the user; the detector then integrates until the end of t_{exp}, after which the array is read out once again. This process could be applied to any number of Fowler samples, N (where N >1). For NFS=N, the read operation at the start and end of the integration ramp is performed N times each. Performing the read operation with a Fowler sampling of N will reduce the read noise by a factor of $\sqrt{N}$ (Fowler and Gatley 1990). Using the difference of the reads at the beginning and end of the integration cycle helps get rid of systematic effects inherent in the array which will otherwise affect our measurements. This includes the "kTC" noise added to the detector right after the inital reset operation, resulting from a build-up of charge on the integrating capacitor by thermally generated currents which manifests itself as a jump in the voltage to a variable new level (Reike 2007; Fowler and Gatley 1991). Subtraction of N (where $N \geq 1$) reads (after being averaged) at the beginning and end of the integration cycle will successfully remove this noise. Since our measurements were performed in the NFS=1 mode, we obtained two reads and our signal consisted of the difference frame between the two reads. Figure 6.1 shows the processes associated with acquisition of an infrared image with and without Fowler sampling.

6.5 Motivation for this work

The University of Colorado built a near-infrared instrument known as the The Near-Infrared Camera & Fabry-Perot Spectrometer (NICFPS) for the Astrophysics Research Consortium (ARC) 3.5 meter telescope for use at the Apache Point Observatory (APO), first made available to the ARC community in 2005. NICFPS uses a Rockwell Hawaii 1-RG detector, sensitive within the wavelength range ∼0.85–2.5 μm. Initially, the device was designed to be read out in the 2-channel mode which required ∼ 5.4 seconds to read out the entire array. In 2007, the read out capability was upgraded to the 16-channel mode thereby cutting down the readout time to ∼1.0 second[1] . The number of times the detector is read out for each exposure is determined by the Fowler Sampling setting. Following the upgrade to 16-channel, an increase in the read noise in NICFPS was noted; specifically, the read noise increased by ∼90 e^- in the CDS mode. To reduce the read noise in the exposures, the detector was read out using the NFS=8 setting, but at the cost of increased read out time of the array. To understand the behavior of read noise in these devices aimed at lowering the read noise in NICFPS, a study was undertaken by me under the guidance of Stéphane Béland at the Astrophysical Research Laboratory in the University of Colorado. This study was to be conducted on the Hawaii– 1RG engineering grade chip that would serve as a test bed for reducing the read noise in NICFPS. Since no characterization numbers were available for this device from the manufacturing company (Rockwell Scientific, now known as Teledyne), we first proceeded to characterize the array.

6.6 Experimental set-up and tests conducted

The first objective of our tests was to characterize gain and read noise of the Hawaii–1RG engineering grade chip. The Hawaii-1RG (hereafter, H1RG) chip was operated in the slow read mode (100 kHz) and the 2-channel output. The fast read mode (∼5 MHz) is

[1] `http://www.apo.nmsu.edu/arc35m/Instruments/NICFPS`

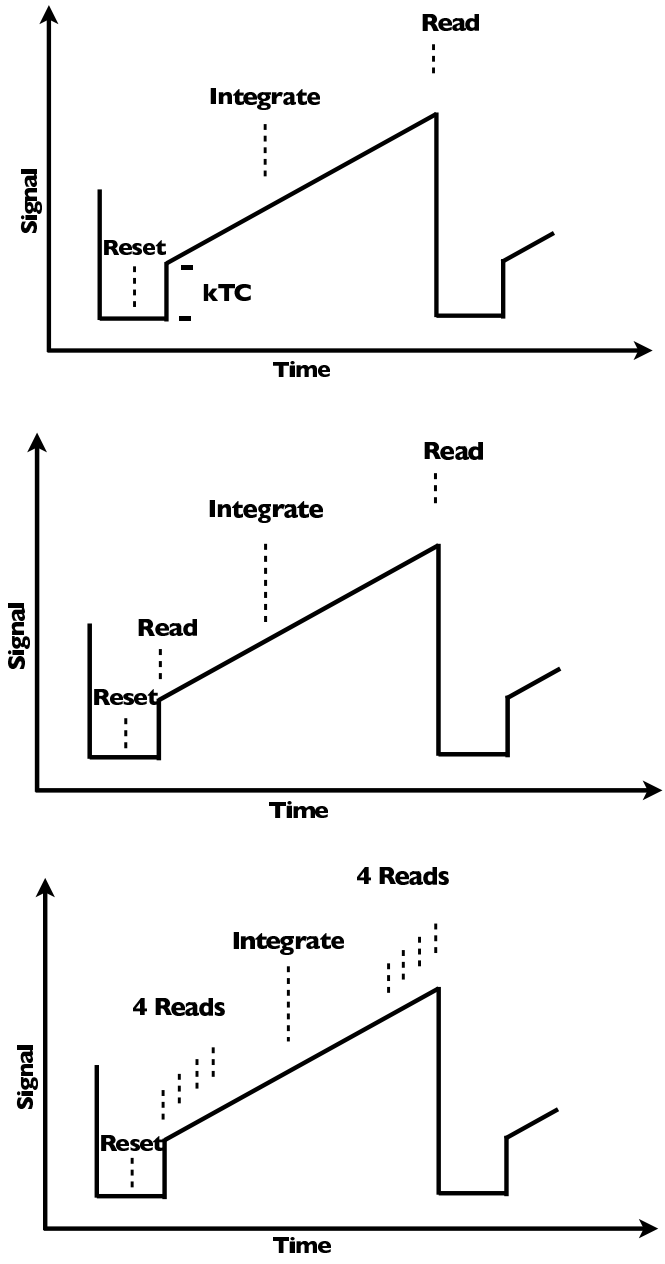

Figure 6.1: Schematic representation of the Fowler sampling process associated with acquisition of an IR image. The top panel represents a simple reset-integrate-read operation (NFS=0) that does not remove the variable "kTC" noise. The central panel shows the CDS (or NFS=1) mode that involves subtraction of two reads at the beginning and end of an an integration cycle. This remove the ''kTC" noise successfully. This Fowler sampling technique can be repeated for any number of reads at the beginning and end of an integration cycle. The final image is produced from a subtraction of such "N" average reads. The bottom figure shows the scheme applied to 4 such reads. Source: recreated from `www.caha.es/CAHA/Instruments/IRCAM/MAGIC/ObsGuide`

achieved at the cost of increased read noise of up to five times as well as greater power consumption. In the slow read mode, the entire array could be read out in 5.3 seconds (see *The Hawaii-1RG Technical Documentation* by Rockwell Scientific).

In our experimental set-up, the H1RG engineering grade chip, a fan-out board and an infrared light emitting diode (LED) were housed in a Dewar that was cooled down by liquid nitrogen (LN2) to temperatures of ~ 65 °K so that the array could operate below thermal infrared temperatures. The Dewar was connected to a controller that operated the array via the fan-out board. One side of the fan-out board connected directly to the H1RG chip via a 92-pin Hirose connector and the opposite side connected to the controller via three 21-pin Glenair connectors. All our tests were tried out with the fan-out board fabricated at University of Colorado (hereafter, CU fan-out board) and some tests were conducted with another fan-out board fabricated at the University of Virginia (hereafter, UVA fan-out board). The CU fan-out board is populated with 10 KΩ resistors on the VDDA line to the detector while the UVA fan-out board was designed with the option to add RC filters on the VDDA line for read noise reduction purposes. The VDDA line supplied the power for the internal analog electronic components in the H1RG detector. Additionally, the UVA board was designed to provide better shielding than the CU fan-out board.

The controllers used for our tests were a Leach controller and a Rockwell controller. The Leach controller houses the video processor board and the timing board. The video processor board amplifies and digitizes the video signals from the chip. The timing board provides the clock signals necessary for controlling the array as well as for maintaining communication with the host computer Peripheral Component Interconnect (PCI) board via a fiber optic cable (Leach and Low 2000). The Rockwell controller consists of the main electronics box that connects to the dewar containing the H1RG chip and is responsible for digitizing the analog output at either 100 KHz or 5 MHz. In addition, it contains the frame buffer box which converts the data from the main electronics box to a 25 MHz digital output which is then interfaced with a PC frame grabber (Clarke 2004).

In our experimental set up, an aluminum box, in contact with the cold base inside the Dewar, was mounted over the chip and the LED. The brightness of the LED was manually controlled by passing currents (of the order of μA) through it. This was used to uniformly illuminate the array for gain measurements. Before conducting any tests, the FPA was cooled down to temperatures where the thermal noise would not dominate. First, the Dewar had to be pumped out until the pressure inside dropped to $\sim 10^{-6}$ Torr. The cooling process was started by slowly administering LN2 into the Dewar at a steady rate of ~ 2 °K/min. Excessive cool down rates could cause delamination of the chip inside the Dewar. Once a temperature of about ~ 65 °K was reached, the flow rate was increased until the tank was topped off. The entire process of cooling took up to 2.5 – 3 hours and refilling of the Dewar was required every 8 – 10 hours to maintain this temperature and to minimize any dark current affecting our measurements. The initial dark exposures that were taken with the Rockwell controller showed pick-up noise pattern in the images. We tried to eliminate this noise by moving the entire set-up (test dewar + controller + computer) to a different work area but found the noise pattern to persist. Finally, we rebuilt all the cables connecting the fan-out board in the Dewar to the Rockwell controller and successfully eliminated the this noise. An example of the dark exposure with the pick up noise and its successful elimination is shown in Figure 6.2. We rebuilt the cables connecting the fan-out board inside the Dewar to the video processor board and timing board housed in the Leach controller, as well.
In the initial experimental setup, we operated the H1RG chip with the Leach controller to mimic the set up currently employed with NICFPS at APO. However, the read noise and gain measurements with the Leach controller were found to be highly inconsistent in every measurement. Therefore, we decided to conduct our first tests with the Rockwell controller then determine the noise contributed by the controller alone, and finally determine the noise contributed by the chip. We then repeated the same tests with the Leach controller to check the consistency with the results obtained from using the Rockwell controller.

All tests were performed with the cryogenically cooled H1RG engineering grade chip

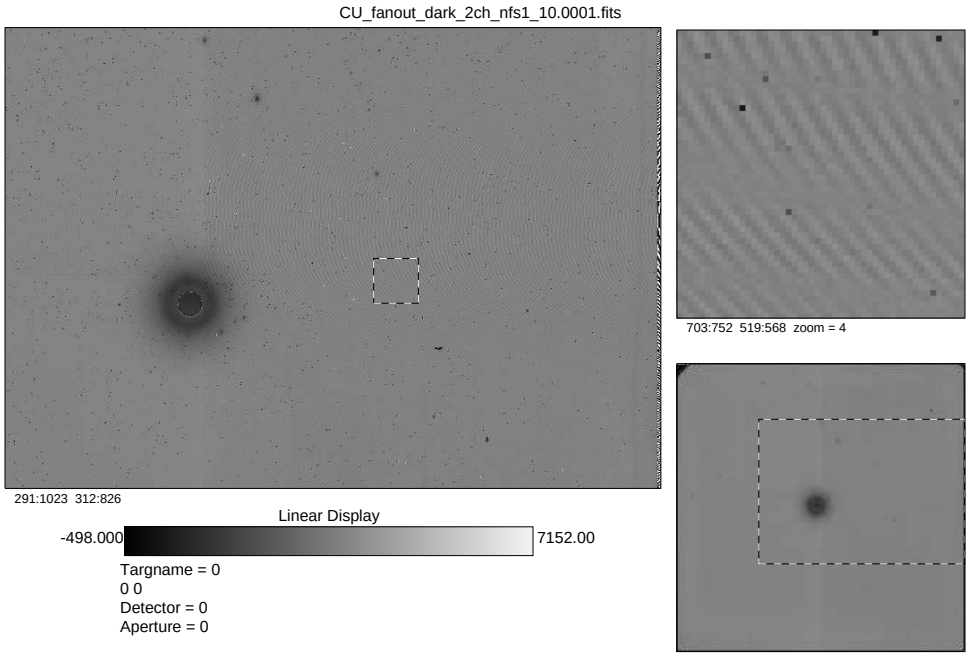

Figure 6.2: A dark image taken with the engineering grade chip and Rockwell controller showing the pick-up noise. The dark circle at the center of the array is from manufacturing defect. The zoomed in selected section of the array in the upper right gives a better view of the noise pattern. The figure on the lower right shows a dark frame taken after the original cables were replaced with new ones. The noise pattern is seen to be eliminated in the exposure.

using the Rockwell and the Leach controllers, aimed at measuring the gain and read noise of the chip. In the sections below, the tests done with each controller individually will be described.

6.7 Measurements done with the Rockwell controller and CU fan-out board

To obtain the gain and read noise measurements of the IR array using the CU fan-out board and the Rockwell controller, it is essential to first determine the linear regime of the chip. To establish this range, using the Rockwell controller, we passed a current of 6 μA through the LED and measured the counts obtained at increasing exposure times. As shown in Figure 6.3, the chip is 3% linear up to 25 K counts (ADU) which occurs at an exposure time of 30 seconds for this lamp current. Beyond that the chip deviates rapidly from the linear regime with increasing exposure times. Array saturation is reached near 35 K counts attained for an exposure time of 60 seconds for 6 μA current through the LED. From the same figure, we see that at exposure times $>$ 80 seconds, well beyond the point when the array has reached saturation, the counts drop by $\sim$1.5%. We operated the chip well within the linear regime for our tests.

6.7.1 Technique for gain and read noise measurements

For the system gain measurement, we obtained images in the CDS mode by passing a current of 6.0 μA through the LED at increasing exposure times from 10 – 20 seconds with a step size of 2 seconds thereby ensuring that the detector operated in the linear range. For each image, the difference between the two reads at the beginning and end of the integration time constituted the 2D processed image. We acquired two such processed images at every exposure time. Next, we obtained an average image and a difference image computed from these two processed images. Using the difference image to calculate the statistics eliminated sensitivity variations across the image as well as get rid of dark current. Two different procedures were employed for the gain calculation: a) the standard variance method, and

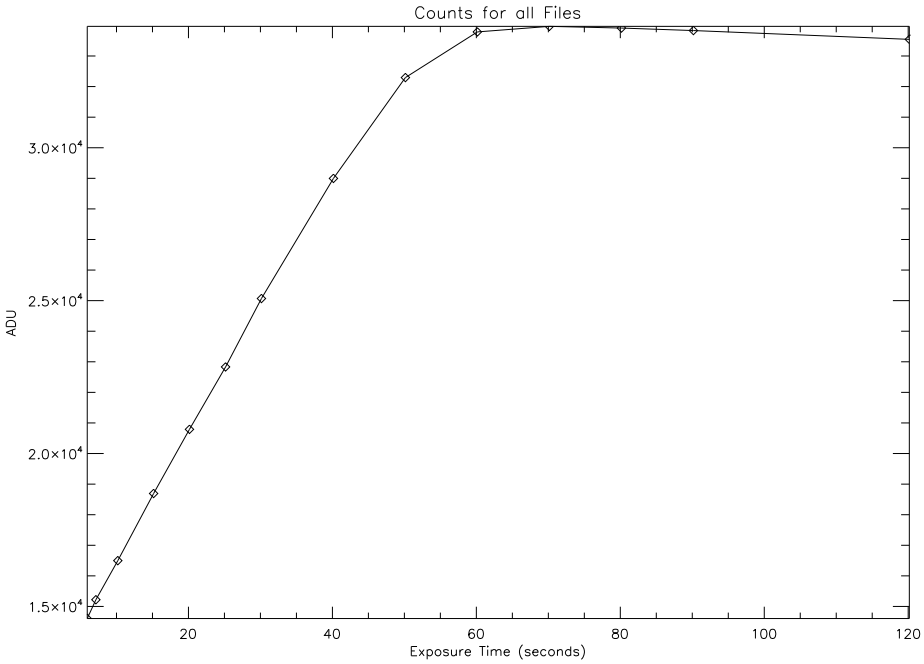

Figure 6.3: Plot showing the dynamic range for which the H1RG array is linear when operated with the Rockwell controller and the CU fan-out board.

b) the Gaussian fitting method. In the standard variance method of computing the system gain, the variance computed on the difference image was plotted against the mean computed on the average image. A straight line fit through the data points at various exposure times gave the system gain. In the Gauss fitting method, we fit a Gaussian to a histogram of the pixel values in the average image as well as in the difference image to obtain the mean signal and variance of the signal respectively. Once again, a straight line fit through these data points at various exposure times gave the system gain. To keep track of the variation of the gain over the entire array, we computed the gain over various sections of the array.

For measuring the read noise, we obtained ten sets of dark frames in the CDS mode with exposure times of 10 seconds each. Once again, the 2D processed image for each dark frame was obtained by a subtraction of the first read from the second read. These processed images served as the input to the read noise calculation. We first computed the variance of the counts for every pixel in the ten sets of processed images and obtained a variance image from this. The process of calculating the read noise from the variance image was initiated by taking a histogram of all pixels within 5σ of their median value. The histogram was then fitted with a Gaussian curve and the mean was taken from the fit parameters and reported as the read noise (in ADU). The read noise was then converted into units of e^- by multiplying by the system gain obtained in the manner described above. We also obtained a sample mean (without fitting the Gaussian) on the distribution of the pixel values from the variance image that agreed closely with the mean obtained from fitting a Gaussian. For all our read noise and gain tests, we selected sample regions with size 100×100 pixels that covered the upper, central and lower parts in both halves of the chip. The following regions ([X1:X2, Y1:Y2]) were used throughout the study:

upper left [184:284, 659:759]

upper right [639:739, 641:741]

lower left [184:284, 224:324]

lower right [641:741, 295:395]

center left [148:248, 382:482]

center right [662:762, 487:587]

6.7.2 Read noise and gain results

The results obtained from gain and read noise measurements using with the Rockwell controller and the CU fan-out board can be summarized with the plots shown in Figure 6.4 and Figure 6.5. We note that the system gain varies between the Gaussian fitting method and the standard variance method for the upper third of the chip. Systematic errors introduced by the detector itself could skew the distribution from an expected Gaussian curve for the mean counts, probably from manufacturing defects in the Engineering grade chip. The system gain estimated by the standard variance method is more consistent across different sections of the chip and we used this value to compute the read noise. For the rest of the study the gain value obtained from the standard variance method will be used to convert the corresponding read noise into units of e^-. The read noise values obtained for the corresponding sections of the chip are shown on the right column of Figure 6.4 and Figure 6.5. We computed the average gain for all six regions across the chip (using the standard variance method) and applied this towards obtaining the average read noise. **Thus, using the Rockwell controller, we determined the average gain and readnoise for the engineering grade chip using the above six regions as 6.43 e^-/ADU and 67 e^- respectively.**

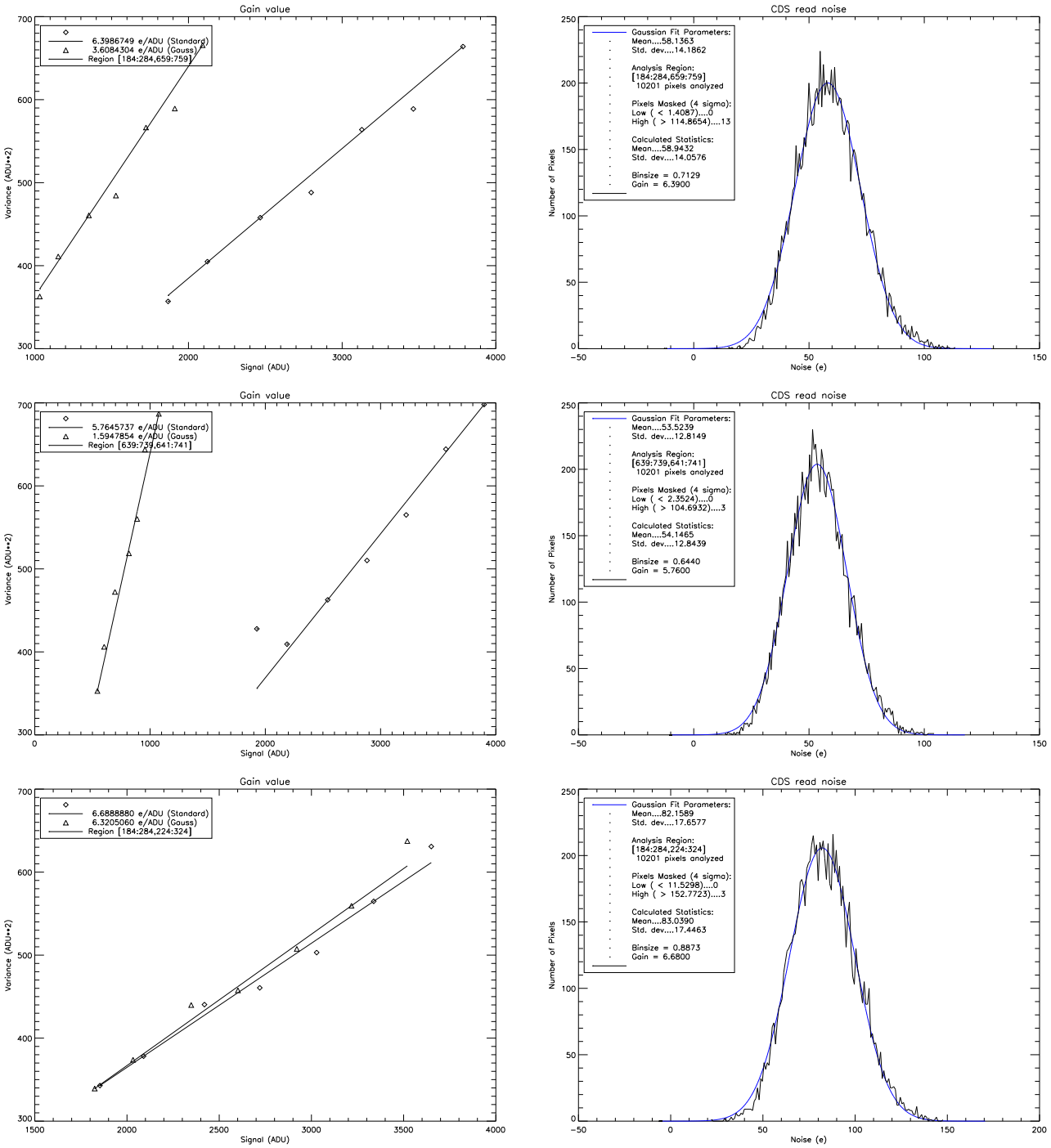

Figure 6.4: Gain and read noise measurements with the Rockwell controller and using the CU fan-out board for different sections on the array.

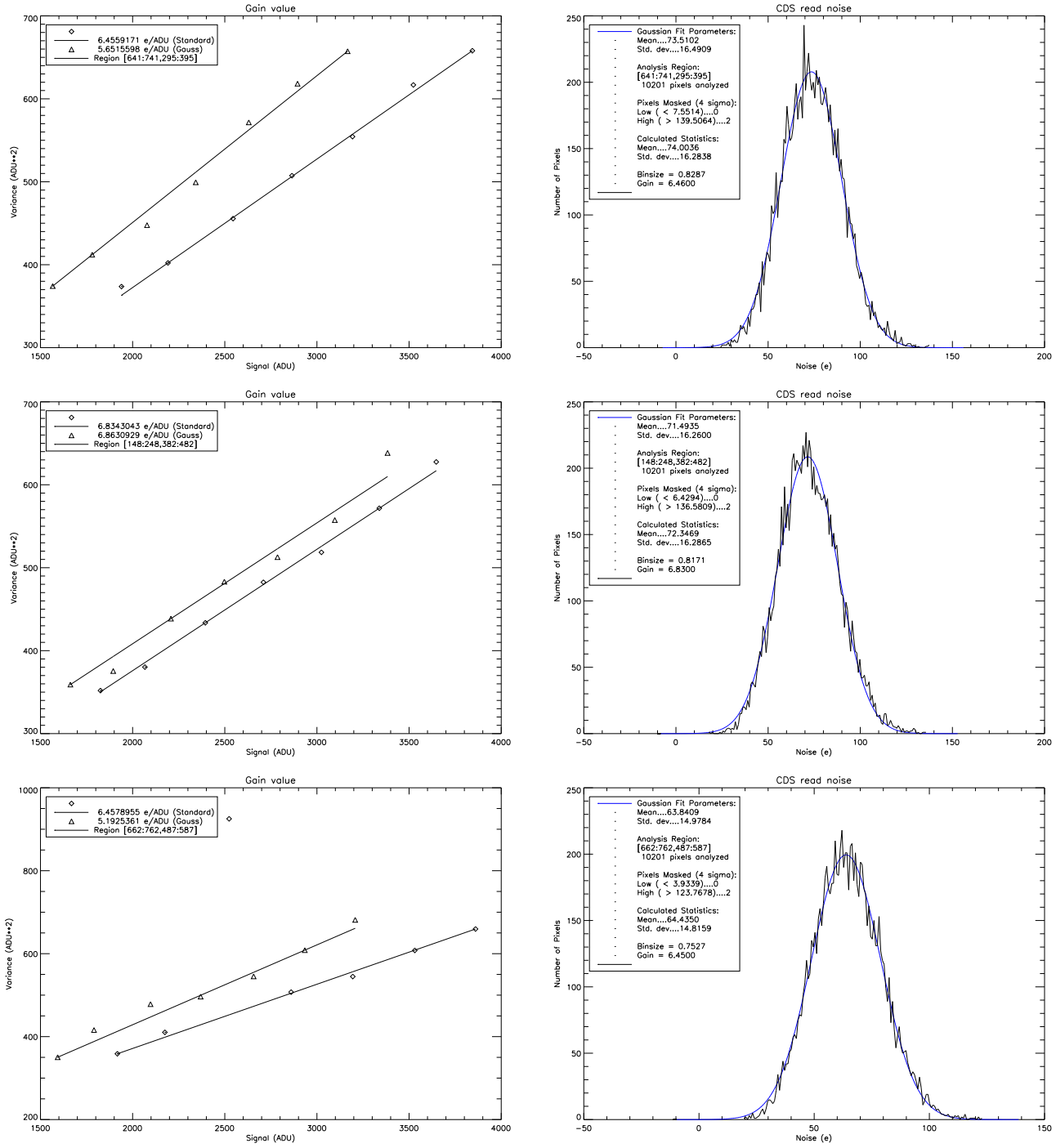

Figure 6.5: Gain and read noise measurements with the Rockwell controller and using the CU fan-out board for different sections on the array.

6.8 Measurements done with the Rockwell controller and UVA fan-out board

For a consistency check, we first populated the bare UVA fan-out board in a manner so as to resemble the CU fan-out board exactly. Then we ran our gain and read noise tests to detect any difference in the results for the two identical looking fan-out boards with better shielding for one than the other. To conduct the tests with the UVA board, we first let the LN2 in the Dewar to evaporate and the temperature inside the Dewar to increase. Then we replaced the CU board with the UVA board, put the Dewar in the pump overnight until pressure dropped to $\sim 10^{-6}$ Torr, and finally cooled it back down by employing the method described in Section 6.6. The entire process took up to $\sim$8 hours for completion. We expected to find the same results as in Section 6.7.2. The linear range of the array using the UVA fan-out board was determined by passing a current of 6μA for increasing exposure times.

Once again we find the array to be linear up to an exposure time of 40 seconds beyond which it starts deviating from this behavior with saturation occurring near 75 seconds. The linearity behavior of the array is shown in Figure 6.6. An interesting comparison with Figure 6.3 shows that while the range of exposure time for which the array shows linearity is comparable in both cases, there is a sharp difference in the level of counts at which the array reaches saturation. It is not understood at this time why both tests done under the exactly similar conditions (the UVA fan-out board was modified to resemble the CU board) should give this difference in counts.

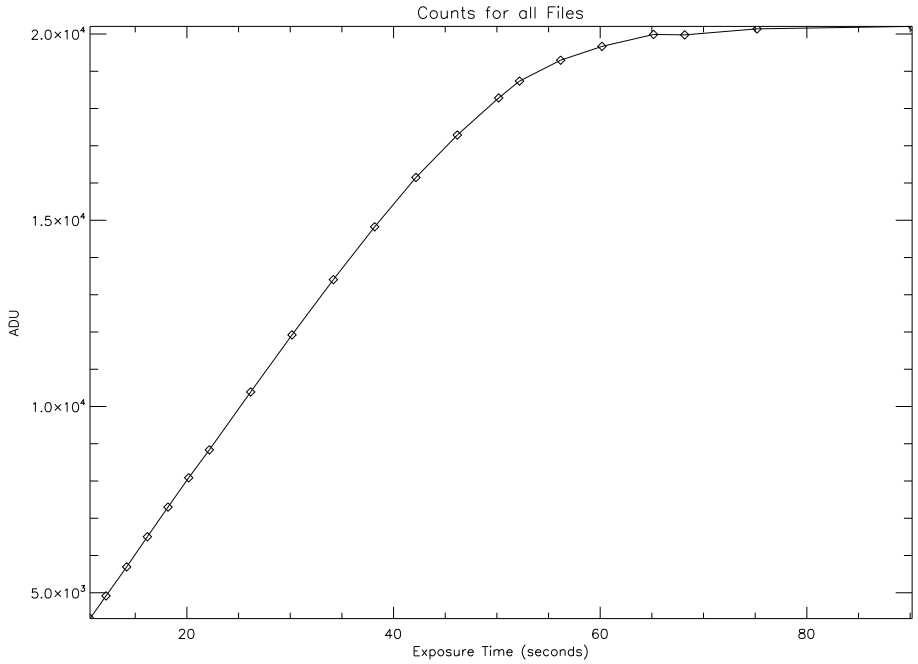

Figure 6.6: Plot showing the dynamic range for which the array is linear when operated with the Rockwell controller and the UVA fan-out board.

6.8.1 Read noise and gain results

Keeping the detector well within the linear regime, we conducted the gain and read noise tests as described before and obtained the results shown in Figure 6.7 and Figure 6.8. Once again we noticed some discrepancy in the gain calculated using the Gauss fitting method. We calculated the average gain using the results obtained from the standard variance method and used this to convert the read noise into units of e^-. **The average gain and readnoise using the six regions on the chip were determined as 7.42 e^-/ADU and 81.4 e^- respectively, using the Rockwell controller and the UVA-fan-out board.** The better shielded UVA fan-out board was designed to produce a lower overall read noise than the CU board. However, we obtained a higher read noise using the UVA board populated in a manner to exactly duplicate the CU board. We do not understand the reason for this discrepancy at this time.

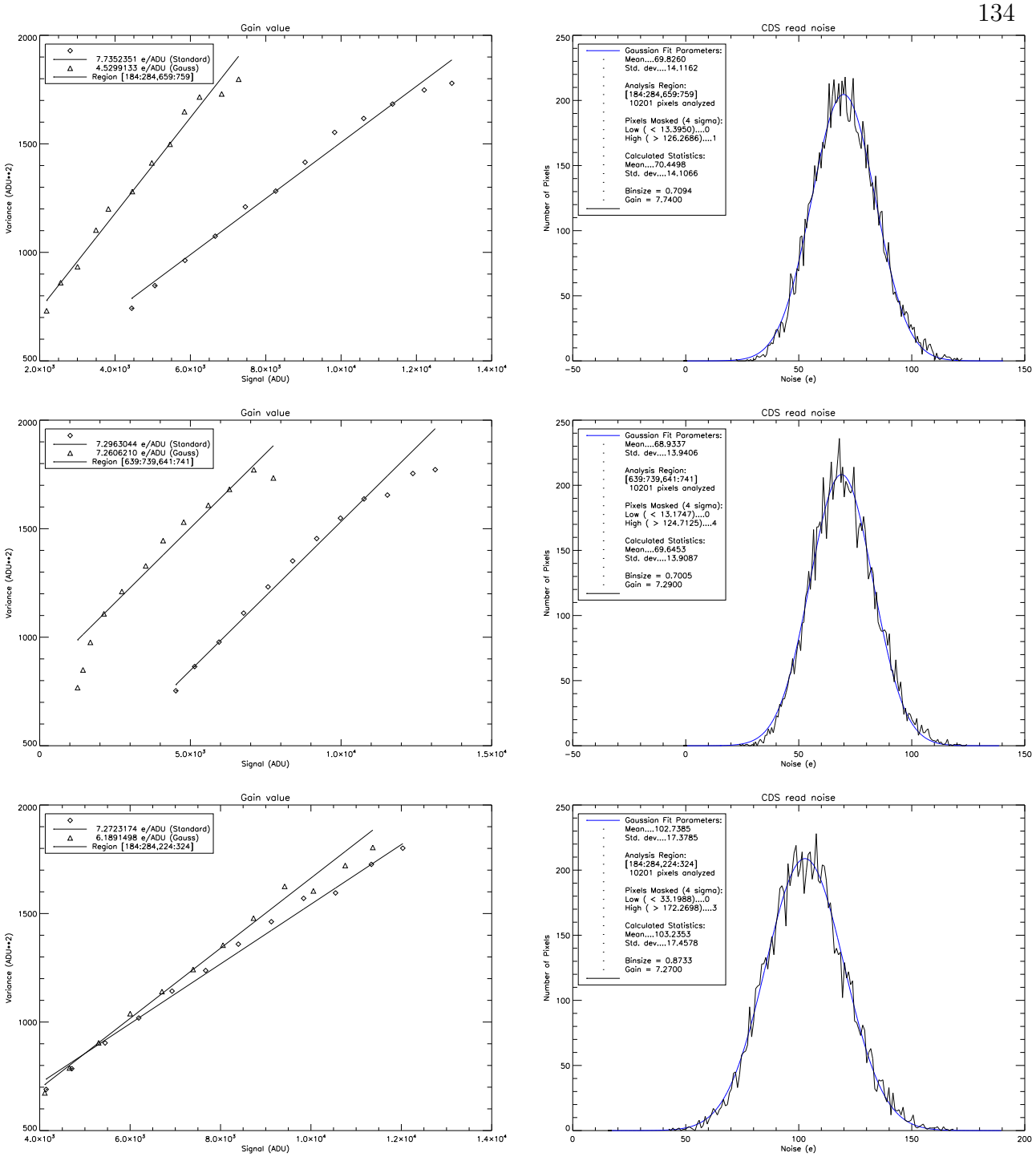

Figure 6.7: Gain and read noise measurements for different sections of the array taken with the Rockwell controller and the UVA fan-out board.

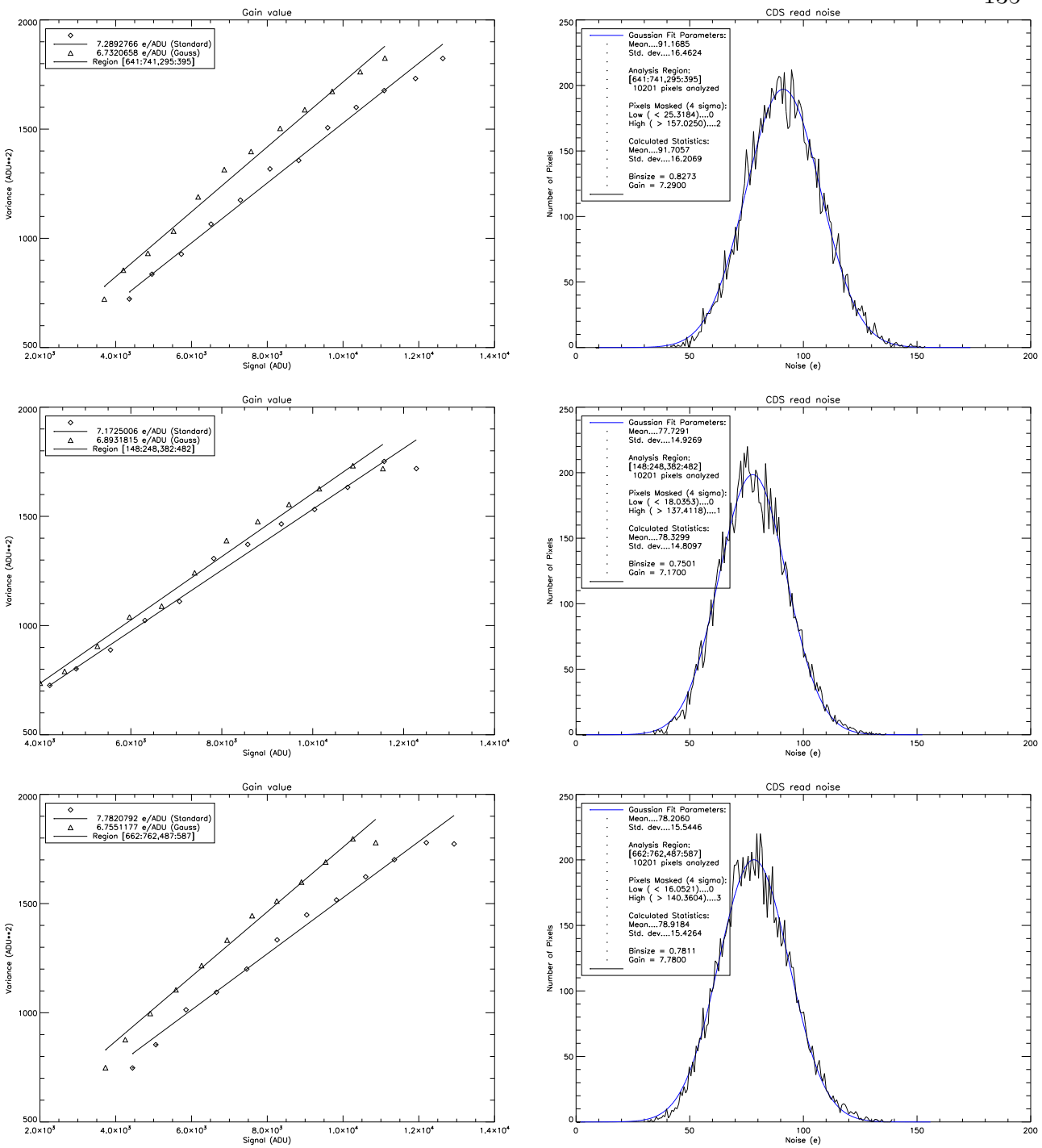

Figure 6.8: Gain and read noise measurements for different sections of the array taken with the Rockwell controller and using the UVA fan-out board.

At this point, we decided to put the CU fan-out board back in the Dewar and run a set of tests to determine the noise arising out of the different components in the experimental set-up namely the Rockwell controller, the fan-out board and the cables. Once we correctly determined these values, we could proceed to conduct the same tests with the Leach controller and observe the difference. Then, we would repeat the same tests by including the UVA fan-out board in the system. Each time we conducted a new test that required replacing any hardware component inside the Dewar, the entire cooling cycle associated with it was repeated so as to keep the FPA operating below thermal infrared high background temperatures.

6.8.2 Noise associated with the Rockwell controller

To measure the noise contributed by the Rockwell controller, we used a spare CU fan-out board to connect to the H1RG array. The output lines from the array on the fan-out board were then manually cut with an x-acto knife to create a break in the circuit. Then, one of the incoming reference voltages was rerouted back into the previous array outputs. In this way we could measure the read noise using a reference voltage instead of the actual detector output. Since we were operating the array in the 2-channel read out mode, we sent the reference voltage (VBIASPOWER, in our case) to the output channels 7 and 15 and a different reference voltage (GND) to the complements. (A detailed explanation of the purposes of the various voltages used in the operation of the H1RG array can be found in the *The Hawaii-1RG Technical Documentation* by Rockwell Scientific). In another set up, we bypassed the fan-out board completely by connecting wires that went to and from the connector of the fan-out board. This was done to detect any observable difference in the noise calculation when the fan-out board was left out from the set-up. This was the way to confirm that connecting the array with/without the fan-out board in the entire setup did not have any effect on the controller noise. With these tests we found a readnoise of $\approx$5.5

DN coming from the Rockwell controller. Noise measurements from four different sections of the array are shown in Figure 6.9. We also found that the noise contribution from the Rockwell controller was not affected by including the cables that ran from the Dewar to the controller. This just implies that the fan-out board or the cables introduced insignificant noise in the experimental set-up.

If we used an average gain of 6.43 e^-/ADU (gain obtained with the CU fan-out board), the noise contribution from the controller is 55.9 e^-. This implies a readnoise contribution of 36.9 e^- from the chip itself.

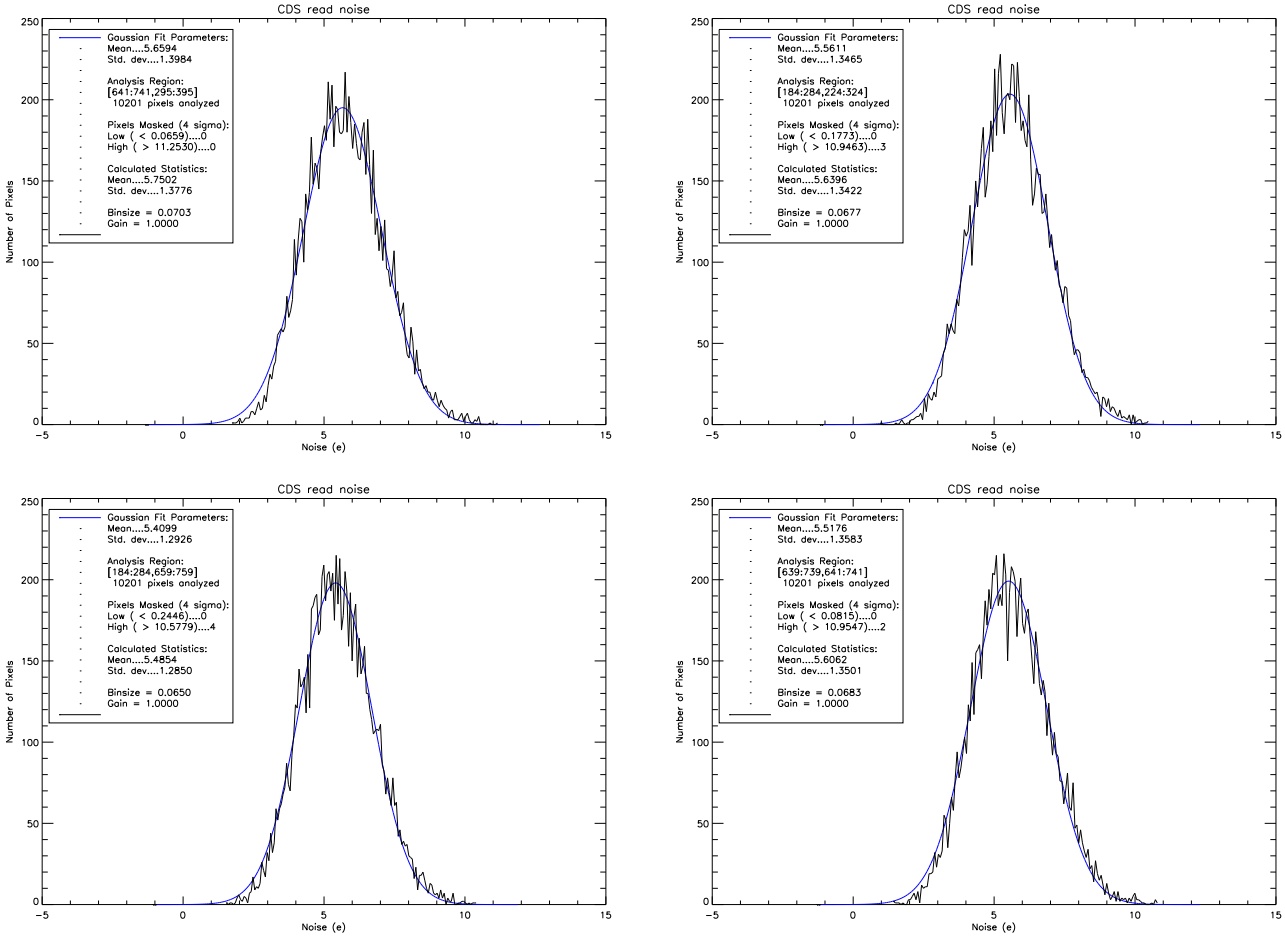

Figure 6.9: Noise contributed by the Rockwell controller, measured using reference voltages instead of actual detector output.

6.9 Measurements done with the Leach controller and CU fan-out board

Since the start of our tests, one persistent issue with the Leach controller has been inconsistency of results. For example, the gain and read noise numbers varied wildly with no pattern thereby making it extremely challenging to characterize the array using this controller. We measured the various power supply voltages, bias voltages as well as the output voltages used by the H1RG array and compared them against the recommended values in the H1RG manual. These voltages are listed in Table 6.9 along with our measurements and the recommended values in columns 2 and 4. We found that the values of the voltages B07, DRAIN, DSUB, COMP7 and COMP15 disagreed with the recommended values; some of these voltages gave negative values. Another issue with the exposures taken with the Leach controller consisted of: wildly varying counts for the images taken with the same amount of current being passed through the LED. At another time, the array would not display any difference in the number of counts for an image taken by passing a current of 2 mA for an exposure time of 500 seconds versus a current of 6 μA taken for an exposure time of 20 seconds! We perceived the inconsistent behavior to be an artifact of the voltage issue and sent the Leach controller to Astronomical Research Cameras Inc. requesting them to look into this problem. The clock driver and timing boards passed all of their tests. However, they detected one of the jumpers in the video board to be in the wrong location and rectified it. They also found that the waveforms that were brought on the timing board were delayed by a few nanoseconds; they corrected this issue as well. Once again, we measured the voltages after the Leach controller was shipped back to us and found the values to agree quite closely with the recommended values in the H1RG users manual. Column 3 in Table 6.9 shows the voltages measured for the various input/output signal requirements of the H1RG array after the Leach controller was repaired.

After the voltage issue was resolved, we obtained dark images as well as uniformly illuminated flat fields and found the images to behave in an explicable manner. As before,

we determined the linear range of the array using the Leach controller by passing a current of 6 μA through the LED for increasing exposure times using the CU fan-out board. The linearity plot is shown in Figure 6.10. We noted that the array was linear up to exposure times of $\sim$28 seconds but deviated from the linear behavior by >5% beyond that. We also found that the counts at which the array reached saturation was around 30 K; this value was lower by about 5 K counts for the tests conducted with the Rockwell controller and the CU fan-out board in Section 6.7. For the gain and read noise measurements, we operated the array within the linear regime. After the array was cooled down to thermally operable temperatures, we obtained the initial dark and flat frames and obtained surprisingly high read noise values ($\sim$ 200 – 500 e^-). After much investigation and voltage tweaking, it was found that adjusting the voltage level of B07 (bias voltage used for the complement inputs) to match that of the recommended output voltage (OUT 7, 15) reduced the read noise by >150 e^-.

Voltages	Before repair (V)	After repair (V)	Recommended values (V)
VDD	3.26	3.25	3.30±5%
VDDA	3.26	3.26	3.30 ±5%
CELLDRAIN	0.00	0.00	≥0.00
DRAIN	-0.584	-0.001	≥0.00
VBIASPOWER	3.21	3.26	≤3.30
DSUB	-0.53	0.35	<1.70
B07	-0.51	0.00	∼0.00
COMP 15	-0.51	0.00	∼0.00
OUT 15	3.23	3.24	≤3.30
COMP 7	-0.51	0.00	∼0.00
OUT 7	3.23	3.24	≤3.30

Table 6.1: Table listing the voltages used by the H1RG Engineering Grade chip along with the measured values before and after the Leach controller was repaired. The last column shows recommended voltage values.

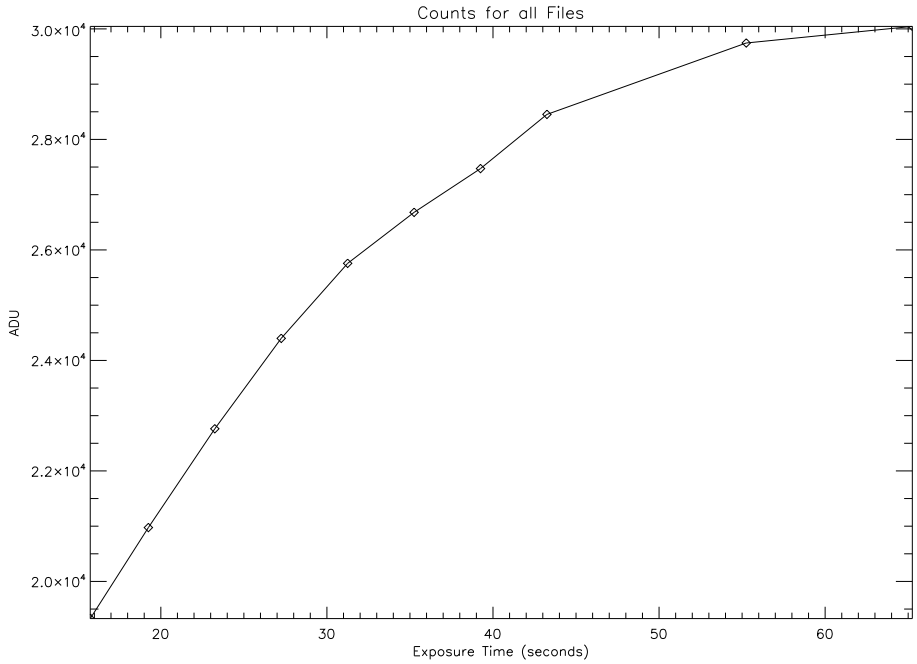

Figure 6.10: Plot showing the dynamic range for which the array is linear when operated with the Leach controller and the CU fan-out board.

6.9.1 Read noise and gain results

For measuring the gain of the H1RG array using the Leach controller, we passed a current of 6μA through the LED for obtaining uniformly illuminated images. The current was chosen such that it was consistent with all the previous tests. We also used the same exposure times as we used for the tests done with the Rockwell controller so as to have a one-on-one comparison of the results. Our gain and read noise measurements obtained with the Leach controller and the CU fan-out board are shown in Figure 6.11 and Figure 6.12 .

As mentioned before, the H1RG array is operated in the 2-channel read out mode. From Figure 6.11 and Figure 6.12, it is apparent that the output channels 7 and 15 have very different gain values. If we consider the two channels separately, then the average gain (using the standard variance method) and readnoise in channel 7 are 3.88e^-/ADU and 70.9e^- and the corresponding numbers in channel 15 are 1.55e^-/ADU and 38.6e^- respectively. It

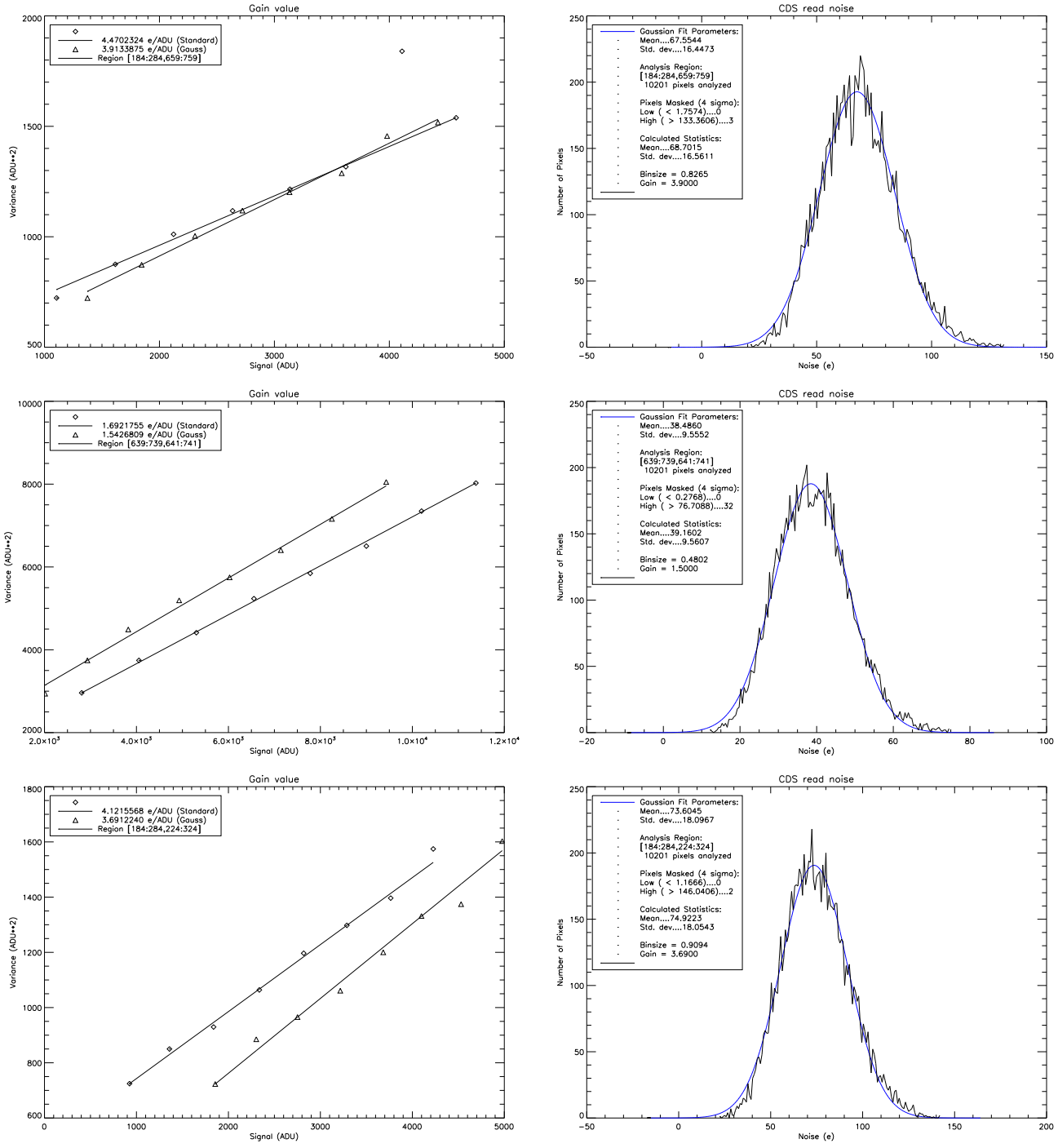

Figure 6.11: Gain and read noise measurements for the array using the Leach controller and the CU fan-out board.

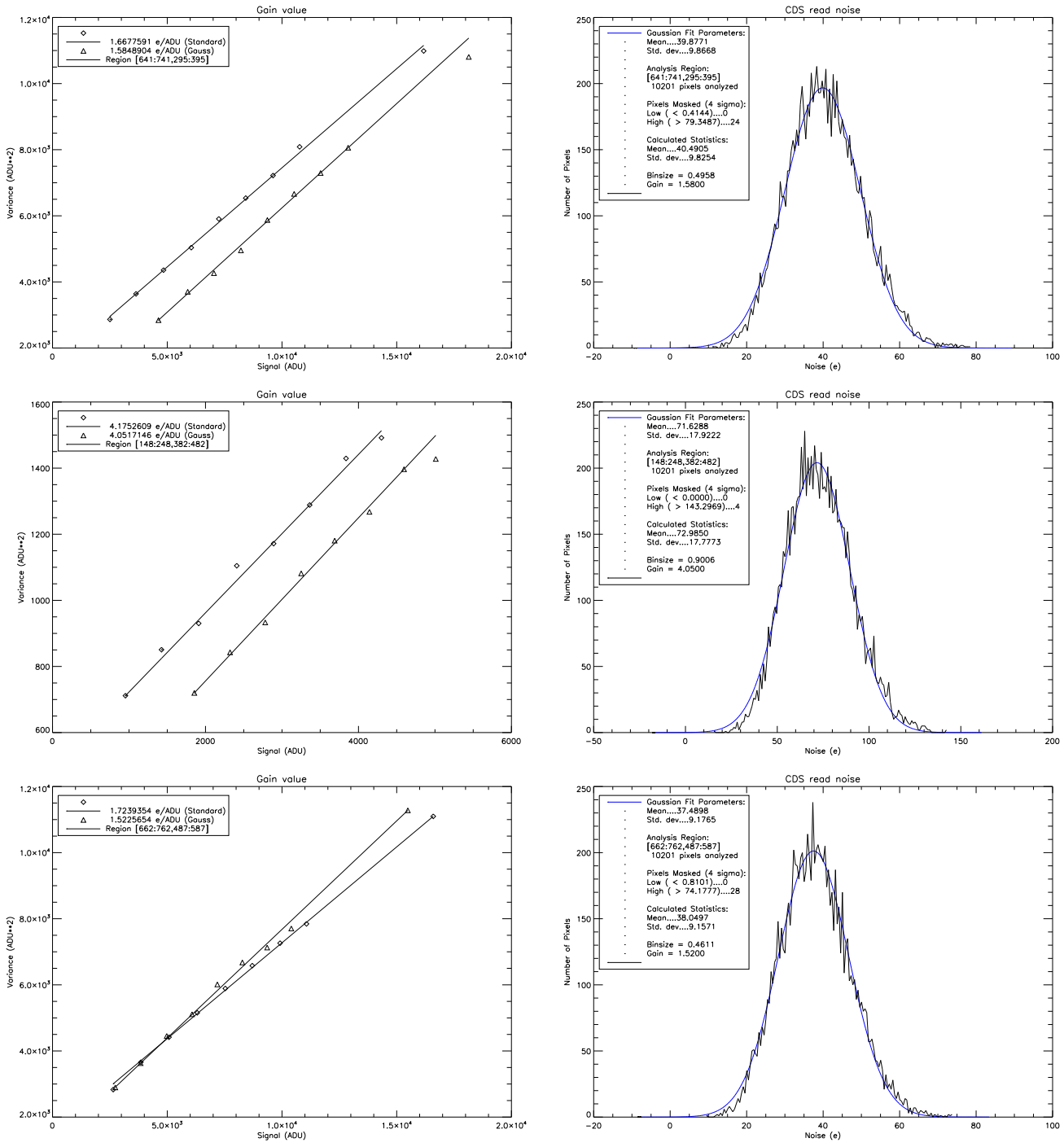

Figure 6.12: Gain and read noise measurements for the array using the Leach controller and the CU fan-out board.

is worth noting that the gain values are lower than those obtained for the array with the Rockwell controller using both CU and UVA fan-out boards for the exact same tests. **The average gain and read noise for the entire array is reported as the average of the values obtained for channels 7 and 15. Thus, when operated with the Leach controller and the CU fan-out board, we obtain the average gain of the array as 2.7e^-/ADU and the read noise as 54.8e^-.**

6.9.2 Noise associated with the Leach controller

We next wanted to measure the noise coming from the Leach controller alone by following the same procedure as described in Section 6.8.2 for the Rockwell controller. We fed VBIASPOWER to the output channels, and B07 to the complements and took another set of read noise measurements. The results of these measurements are plotted in Figure 6.13. We obtained a value of 5.4e^- for the noise coming from the Leach controller alone (using the average gain of 2.7e^-/ADU). This was the same whether we included the chip, fan-out board and the cables in the set up or not. **This translates to an average read noise of 54.5 e^- coming from the chip alone.** The results do not agree with read noise obtained with the tests done with the Rockwell controller (37 e^-).

To address the issue with the different gain values in the channels 7 and 15, we performed another test that used the video card in the Leach controller. We changed the value of VBIASPOWER as our simulated output signal from 2.90 V to 3.20 V in steps of 0.02 V. We picked reference pixels from both sides of the chip to see whether DNs vs voltage plot behaved differently for the two channels. We found that the two plots closely followed each other suggesting that the videocard was not contributing to the difference in the gains in the two channels. This is depicted in Figure 6.14

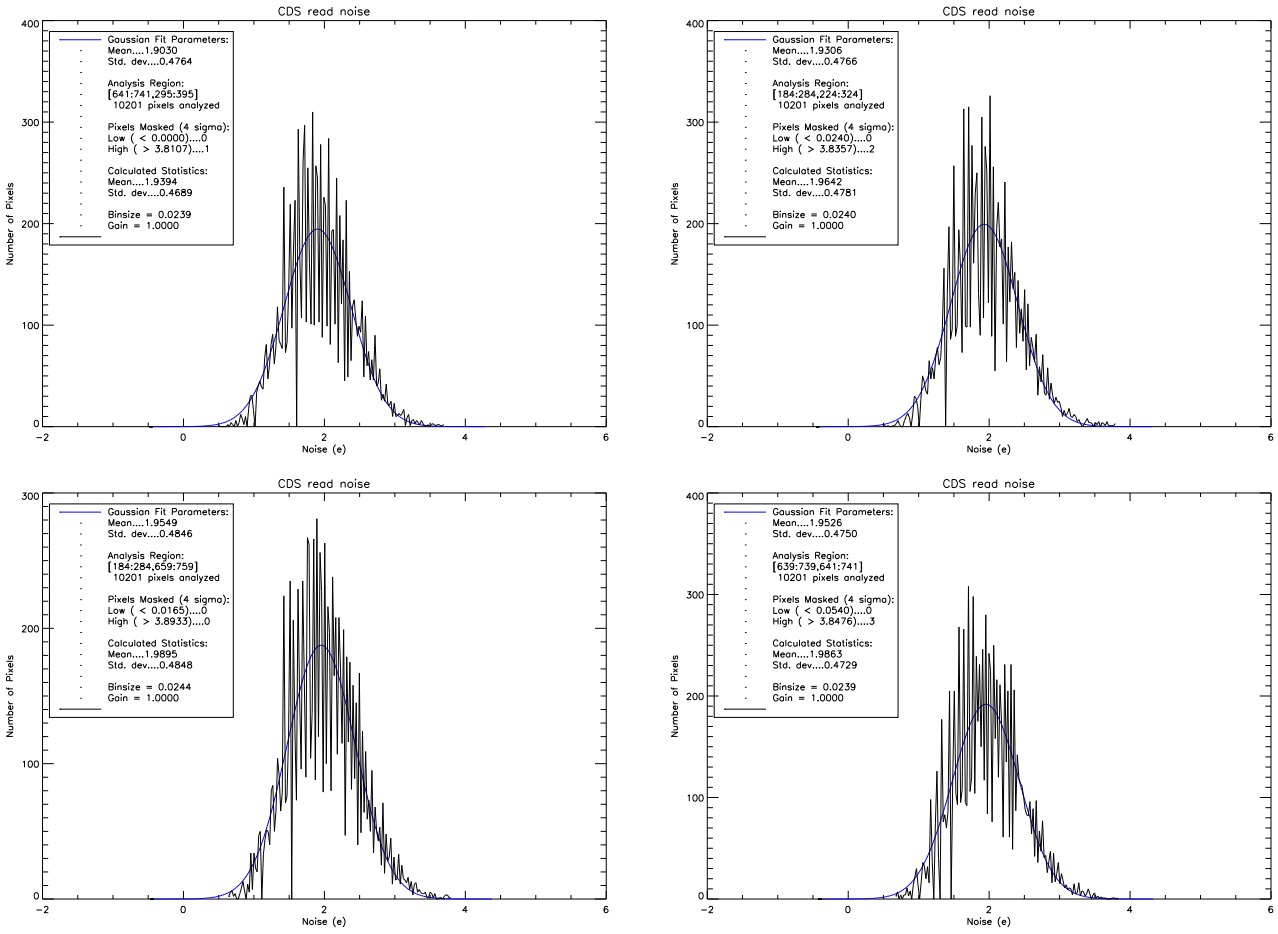

Figure 6.13: Noise contributed by the Leach controller, measured using reference voltages instead of actual detector output.

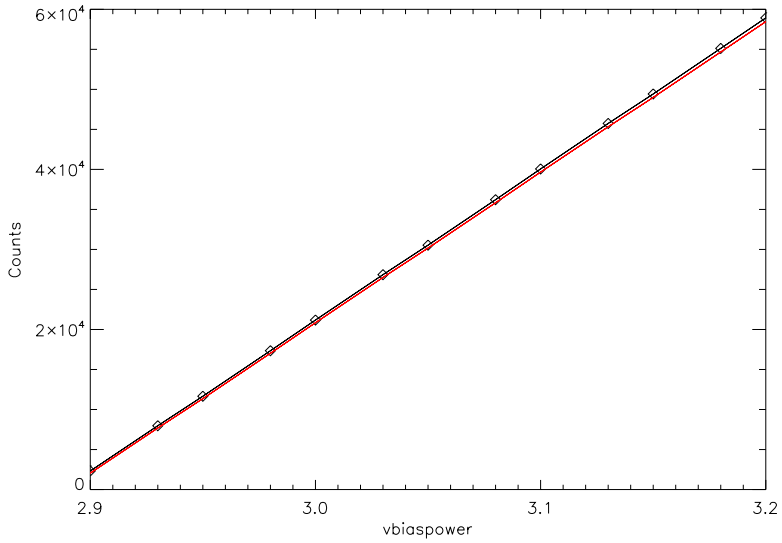

Figure 6.14: Gain measured for increasing simulated output voltage values. The black line shows gain from channel 7 and the red line shows gain from channel 15.

6.10 Conclusion

We characterized the gain and read noise of the Hawaii-1RG Engineering grade array using a variety of tests performed with two different controllers and two different fan-out boards. However, many issues remain unaddressed at this point. Some of the important issues concerning the behavior of the array are: the high read noise of the array when operated with the UVA fan-out board as compared to the CU fan-out board; the difference in the saturation counts for the array when operated with two different controllers and two different fan-out boards; the difference in gain noticed in the two output channels when the array is operated with the Leach controller; and, the difference in gain when the array is operated with the two different controllers.With these constraints, the read noise of the Hawaii-1RG engineering grade chip can be broadly constrained as 37 – 55 e^-.

The primary reason for characterizing the engineering grade chip was to proceed to use this device as a test bed for lowering the read noise in NICFPS using the UVA fan-out board.

The intrinsically noisy engineering grade chip will prevent us from observing the effect of adding filters on the UVA fan-out board. Therefore, it was proposed that we optimize the added filters on the UVA fan-out board with the science grade chip at APO in the test Dewar (used for our tests at ARL) by trying out various combinations of filters on the fan-out board. Each new iteration will involve warming up, removing the fanout board, making the changes, re-installing, pumping, cooling and measuring the resulting read noise. Conducting one of these iterations on the test Dewar could be accomplished in one day as opposed to four days with NICFPS (i.e. if we conducted these tests in NICFPS without removing the science chip). Then, once we find the optimum (lowest) read noise inside the test dewar, we can move the modified fanout board back in NICFPS with the science grade chip. We believed this proposed method to be the fastest and most efficient way to focus on our primary goal, i.e. reducing the read noise in NICFPS. However, concerns about possible damage done to the science chip when operating it in the test Dewar as well as conflicts with the NICFPS observing schedule delayed the tests until the summer of 2011, after my participation in the project had ended. At that time, the UVA fan-out board with the add-on filters was tested with the science chip and the science Leach controller at ARL by Stéphane Béland. The read noise of NICFPS is now at 20.9 e^- in the CDS mode and 16-channel readout mode; this is a significant improvement from $\sim$100 e^- measured after the upgrade to the 16-channel mode.

Chapter 7

Conclusion and Future Work

Since 2007, my collaborators and I have used NIR spectroscopy and photometry to determine precise masses of compact objects in several X-ray binaries. Even though the donor star is assumed to dominate the light from these sources in quiescence at NIR wavelengths, it has been shown in several systems that this assumption is not valid. Not only may other non-stellar sources contribute significantly at these wavelengths but their contribution also varies even when the system is still in quiescence (Cantrell et al. 2008, 2010). We corrected for the previously obtained compact object masses in three LMXBs – V404 Cyg, Cen X-4 and XTE J1118+480 by properly accounting for the NIR flux contributed by non-stellar sources of light (e.g. the accretion disk and/or a jet). In V404 Cyg, we found the contribution from non-stellar sources to be very small ($f = 0.97 \pm .09$ in the K-band) and determined the mass of the black hole in this system as $9.0^{+.2}_{-.6}$ $M_{\odot}$; our black hole mass estimates are consistent with the previous result of Sanwal et al. (1996). In the case of Cen X-4, we obtained lower S/N spectral data compared to V404 Cyg (S/N$\sim$ 25 – 30 in the H-band) which made it challenging to obtain a precise accretion disk contribution. From our data, we estimated the accretion disk contribution as $0.94 \pm .14$ in the H-band which led to the mass of the neutron star of $1.5^{+.1}_{-.4}$ $M_{\odot}$. Our result is consistent with, but more precise (by $\sim 25\%$) than, recent estimates by D'Avanzo et al. (2005). These mass estimates should however be viewed with some degree of caution. The time gap between the acquisition of the spectral data and light curve data for both V404 Cyg and Cen X-4 is $\sim$ 10 years. Even though both systems

remained in quiescence during the entire period of ten years, one can argue based on the work by Cantrell et al. (2008, 2010), that meaningful mass estimates can be obtained only when non-stellar NIR flux obtained from spectroscopy during quiescence is supplemented with contemporaneous light curve data. Motivated by this, we obtained contemporaneous light curve and spectral data for the black hole LMXB XTE J1118+480, to determine an accurate mass of its compact accretor. XTE J1118+480 is about ~ 6 times fainter than Cen X-4 and therefore we used the Gemini 8-m class telescope to obtain moderate S/N spectral data. With 5.5 hours of on-source time, we obtained a S/N $\sim$17 in the H-band, allowing us to broadly constrain the non-stellar contribution to the near-infrared light of $f = 0.50 \pm 0.32$. We then modeled the light curve data, obtained contemporaneously with the spectral data, to obtain the mass of the black hole as $6.9 < (M_{BH}/M_{\odot}) \leq 8.2$. By accounting for the non-stellar light at the time of acquisition of light curve data, we were able to show that the black hole mass in XTE J1118+480 is $\sim$10% lower than past estimates by Gelino et al. (2006). We noted in the case of XTE J1118+480 that the light curve morphology may change also, even when the system was in quiescence; this agrees with the study done by Cantrell et al. (2010) on the LMXB, A0620-00. Our H-band light curve displayed asymmetric features that were adequately fit by a model containing a donor star and an accretion disk with a bright spot; this asymmetry was not seen in the quiescent light curves obtained by Gelino et al. (2006). Therefore, one can conclude that accurate mass estimates can only be obtained by modeling quiescent light curves of LMXBs while simultaneously accounting for other non-stellar sources of flux obtained from spectroscopy. Currently 15 low mass X-ray binaries and 5 high mass X-ray binaries are known with measured compact object masses. A statistical analysis of the mass distribution of the compact objects in this sample shows strong evidence of a gap between the maximum neutron star mass and the lower bound on the black hole masses (between 2 – 4.5 $M_{\odot}$) (Farr et al. 2011; Özel et al. 2010). However, previously estimated masses based on the assumptions of negligible non-stellar contribution and consistent light curve morphology at NIR wavelengths during quiescence could be biased to higher values,

giving the appearance of a top-heavy distribution for compact object masses. These mass estimates need to be revisited. In the future, my collaborators and I plan to continue to obtain precise mass estimates of compact accretors in LMXBs, extending my study to include fainter systems as well as systems that are only accessible from the southern hemisphere. These investigations will rely on NOAO observations with Gemini-North, Gemini-South, Keck, and the SOAR 4-m telescope. Additionally, I will continue to use the the 3.5-m telescope at APO along with my collaborators from the University of Colorado. Specifically, I intend to explore the systems whose minimum mass function $f(M)$, lies close to the observed mass gap since determining if their masses are lower than than the previous measurements will have important consequences for the observed mass gap. To that end, we have proposed to observe the black hole LMXB GRO J0422+32 on Gemini-North. The minimum mass of the BH in this system has been determined as $1.13 \pm 0.09\ M_{\odot}$ (Harlaftis et al. 1999), placing it in the crucial mass gap in the black hole mass distribution, but its mass has been under debate (see Gelino and Harrison 2003 and Reynolds et al. 2007). If rewarded observing time for this system, we will provide accurate mass for what could possibly be the lowest mass black hole ever measured.

My work on the binary milli-second pulsar PSR J1903+0327 has provided the unique information on an astrophysical system that challenges currently favored models of MSP formation and evolution. PSR J1903+0327 is the only MSP in the Galactic disk found so far that is in orbit around a main-sequence star in a highly eccentric orbit. The discovery of this system has led to questions about the accuracy of previously established models of MSP formation mechanisms. We confirmed the association of the MSP with the main-sequence star using a spectrum of the Ca- triplet obtained using GMOS on Gemini-North. We have also broadly constrained the rotational velocity of the main-sequence star (< 66 km s^{-1}). With the present rotational velocity estimate, it will be challenging to perform a test for general relativity at the present time, but will be possible in future with large telescopes such as TMT. Radio pulsar timing can lead to better constraints on General Relativity in com-

parison to scalar tensor theories and should be pursued over the next few years. Our study also showed that the evolutionary scenario for the formation and evolution of this unique pulsar system is best described by the recent numerical simulations of Portegies Zwart et al. (2011), wherein an initial stable hierarchical triple system consisting of an inner LMXB and outer main-sequence star leads to the formation of a system like PSR J1903+0327.

Finally, my study on the performance characteristics of the HgCdTe IR detector has helped to broadly constrain the read noise of this detector. However, several issues associated with our tests still remain, including varying behavior (regarding read noise and gain) of the detector when operated with different fan-out boards and with different controllers. With the current unresolved issues, this detector is not recommended to be used for science data acquisition. In the future, I would like to integrate my knowledge of IR detectors in overcoming the challenges of infrared astronomical observations.

Appendix A

Determination of error in the donor fraction calculation

Due to its low SNR, the donor fraction obtained from the spectrum of XTE J1118+480 in Section 3.1.1 is only meaningful, if accompanied by reliable error estimates. In order to adequately account for the noise in the spectrum, we obtained the Fourier transform of the normalized spectrum in each of J-, H- and K-bands. The Fourier transformed spectra gives a complex valued array , $X(k) = \sum_{n=1}^{N} x(n)e^{(-2\pi i/N)(n-1)k}$, where N represents the total data points, k represents the individual Fourier transformed frequency components, and x(n) represents the normalized flux values. The amplitude of the Fourier transform is given by $A(k) = \sqrt{Re[X(k)]^2 + Im[X(k)]^2}$ and the phase is given by $\phi(k) = \tan^{-1}(-\frac{Im(X(k))}{Re(X(k))})$. To estimate the noise in our spectral data, we 'scrambled' the phase of the Fourier transformed spectrum by adding a different random number between 0 and 2π to the original phase at each k while retaining the the original power spectrum $|X_k|^2$. We used the `rand` function in MATLAB that generates uniformly distributed random numbers between 0 and 1. We then reconstructed the spectrum by calculating the inverse Fourier transform of the 'phase scrambled' Fourier transformed spectrum. In Figure A.1, we depict an example of calculating the donor fraction when an M0.5 V star was compared to the reconstructed 'phase scrambled' spectrum of XTE J1118+480 in the H-band. Any fit done to the 'phase scrambled' spectrum will be spurious since we are fitting signal to pure noise which allows us to place uncertainties on our fits to the original spectrum. We fitted the spectra of field stars with K5 V, K7 V, M0/M0.5 V and M1 V spectral types to each of the phase scrambled spectra and calculated

the donor fraction for each wavelength region under investigation listed in Table 4.2. For each field star and each wavelength region under investigation, we repeated this process for 50 randomly generated phase scrambled spectra and examined the variance of the donor fractions. The square root of the variance is then a robust indication of the uncertainty in the donor star fraction. The errors listed with the donor fractions in Table 4.3 was obtained from this analysis. Finally, these errors were propagated through the remainder of the steps leading up to the average donor fractions in the J-, H- and K-bands.

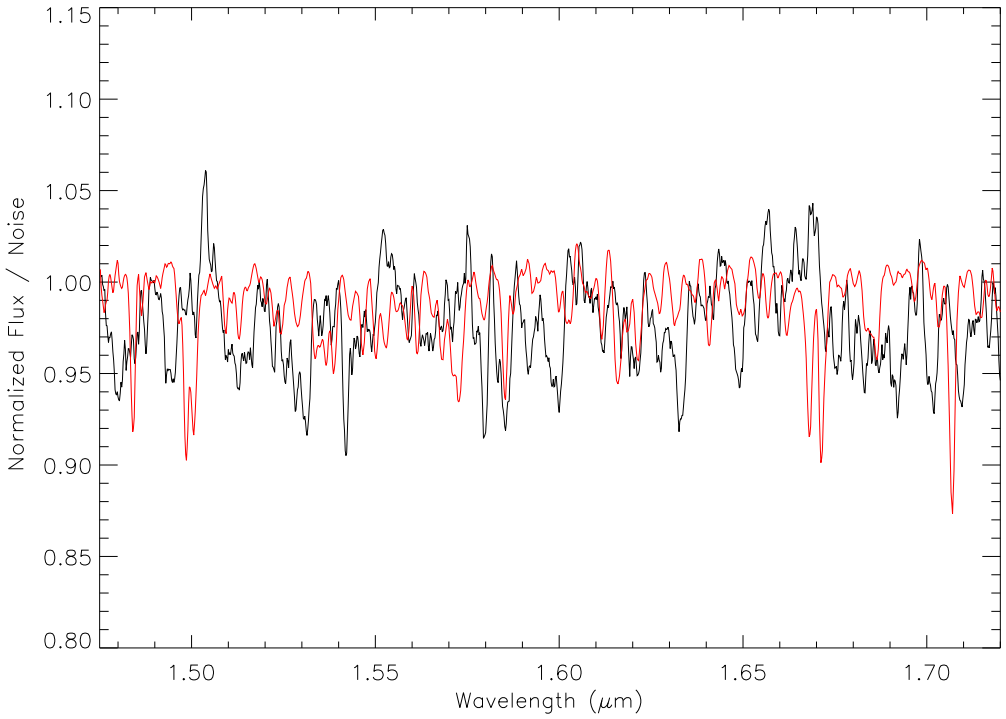

Figure A.1: An example of fitting an M0.5 V star to the inverse 'phase scrambled' Fourier transformed spectrum of XTE J1118+480. The donor fraction variance obtained from fitting many such randomly phase-scrambled spectra were used to place a robust estimate on the donor fraction in XTE J1118+480.

Bibliography

B. Ali, J. S. Carr, D. L. Depoy, J. A. Frogel, and K. Sellgren. Medium-Resolution Near-Infrared (2.15-2.35 micron) Spectroscopy of Late-Type Main-Sequence Stars. AJ , 110: 2415, 1995.

C. A. L. Bailer-Jones. Spectroscopic rotation velocities of L dwarfs from VLT/UVES and their comparison with periods from photometric monitoring. A&A , 419:703–712, May 2004.

C. D. Bailyn, R. K. Jain, P. Coppi, and J. A. Orosz. The Mass Distribution of Stellar Black Holes. ApJ , 499:367, 1998.

K. Belczynski, G. Wiktorowicz, C. Fryer, D. Holz, and V. Kalogera. Missing Black Holes Unveil The Supernova Explosion Mechanism. ArXiv e-prints, 2011.

S. V. Berdyugina and I. S. Savanov. New surface-gravity calibration for G-K giants and subgiants. Astronomy Letters, 20:755–758, November 1994.

N. D. R. Bhat, M. Bailes, and J. P. W. Verbiest. Gravitational-radiation losses from the pulsar white-dwarf binary PSR J1141 6545. Physical Review D, 77(12):124017, June 2008.

D. Bhattacharya. Millisecond pulsars. In W. H. G. Lewin, J. van Paradijs, & E. P. J. van den Heuvel, editor, X-ray Binaries, pages 233–251, 1995.

D. Bhattacharya and E. P. J. van den Heuvel. Formation and evolution of binary and millisecond radio pulsars. Physics Reports, 203:1–124, 1991.

W. P. Blair, J. C. Raymond, A. K. Dupree, C.-C. Wu, A. V. Holm, and J. H. Swank. IUE observations of Centaurus X-4 during the 1979 May outburst. ApJ , 278:270–277, March 1984.

R. D. Blandford and R. L. Znajek. Electromagnetic extraction of energy from Kerr black holes. MNRAS, 179:433–456, May 1977.

M. S. Bothwell, M. A. P. Torres, M. R. Garcia, and P. A. Charles. Spectroscopic observations of the quiescent neutron star system 4U 2129+47 (=V1727 Cygni). A&A , 485:773–775, July 2008.

A. L. Broadfoot and K. R. Kendall. The Airglow Spectrum, 3100-10,000 A. Journal of Geophysical Research, 73:426, 1968.

E. F. Brown, L. Bildsten, and R. E. Rutledge. Crustal Heating and Quiescent Emission from Transiently Accreting Neutron Stars. ApJL , 504:L95, 1998.

D. A. H. Buckley, D. O'Donoghue, D. Kilkenny, R. S. Stobie, and R. A. Remillard. EC 19314 - 5915 - A bright, eclipsing cataclysmic variable from the Edinburgh-Cape Blue Object Survey. MNRAS, 258:285–295, 1992.

D. E. Calvelo, S. D. Vrtilek, D. Steeghs, M. A. P. Torres, J. Neilsen, A. V. Filippenko, and J. I. González Hernández. Doppler and modulation tomography of XTEJ1118+480 in quiescence. MNRAS, 399:539–549, 2009.

C. R. Canizares, J. E. McClintock, and J. E. Grindlay. Discovery of the optical counterpart of the transient X-ray burster Centaurus X-4. ApJL , 236:L55–L59, 1980.

A. G. Cantrell, C. D. Bailyn, J. E. McClintock, and J. A. Orosz. Optical State Changes in the X-Ray-quiescent Black Hole A0620-00. ApJL , 673:L159–L162, 2008.

A. G. Cantrell, C. D. Bailyn, J. A. Orosz, J. E. McClintock, R. A. Remillard, C. S. Froning, J. Neilsen, D. M. Gelino, and L. Gou. The Inclination of the Soft X-Ray Transient A0620-00 and the Mass of its Black Hole. ApJ , 710:1127–1141, 2010.

J. Casares. The Mass Spectrum of X-Ray Binaries. In J. C. Del Toro Iniesta, E. J. Alfaro, J. G. Gorgas, E. Salvador-Sole, and H. Butcher, editors, The Many Scales in the Universe: JENAM 2004 Astrophysics Reviews, page 145, 2006.

J. Casares and P. A. Charles. Optical studies of V404 Cyg, the X-ray transient GS 2023+338. IV. The rotation speed of the companion star. MNRAS, 271:L5–L9, 1994.

J. Casares, P. A. Charles, and T. Naylor. A 6.5-day periodicity in the recurrent nova V404 Cygni implying the presence of a black hole. Nature , 355:614–617, 1992.

J. Casares, P. A. Charles, T. Naylor, and E. P. Pavlenko. Optical Studies of V:404-CYGNI the X-Ray Transient GS:2023+338 - Part Three - the Secondary Star and Accretion Disc. MNRAS, 265:834, 1993.

J. Casares, P. A. Charles, and E. Kuulkers. The Mass of the Neutron Star in Cygnus X-2 (V1341 Cygni). ApJL , 493:L39, 1998.

J. Casares, P. Bonifacio, J. I. González Hernández, P. Molaro, and M. Zoccali. The isotopic ˆ6Li/ˆ7Li ratio in Centaurus X-4 and the origin of Li in X-ray binaries. A&A , 470: 1033–1041, 2007.

G. Cayrel de Strobel, C. Bentolila, B. Hauck, and A. Curchod. A catalogue of /Fe/H/ determinations. A&AS, 41:405–419, 1980.

A. J. Cenarro, N. Cardiel, J. Gorgas, R. F. Peletier, A. Vazdekis, and F. Prada. Empirical calibration of the near-infrared Ca ii triplet - I. The stellar library and index definition. MNRAS, 326:959–980, 2001.

A. J. Cenarro, J. Gorgas, N. Cardiel, A. Vazdekis, and R. F. Peletier. Empirical calibration of the near-infrared Ca II triplet - III. Fitting functions. MNRAS, 329:863–876, 2002.

D. J. Champion, S. M. Ransom, P. Lazarus, F. Camilo, C. Bassa, V. M. Kaspi, D. J. Nice, P. C. C. Freire, I. H. Stairs, J. van Leeuwen, B. W. Stappers, J. M. Cordes, J. W. T. Hessels, D. R. Lorimer, Z. Arzoumanian, D. C. Backer, N. D. R. Bhat, S. Chatterjee,

I. Cognard, J. S. Deneva, C.-A. Faucher-Giguère, B. M. Gaensler, J. Han, F. A. Jenet, L. Kasian, V. I. Kondratiev, M. Kramer, J. Lazio, M. A. McLaughlin, A. Venkataraman, and W. Vlemmings. An Eccentric Binary Millisecond Pulsar in the Galactic Plane. Science, 320:1309–, 2008.

P. A. Charles and M. J. Coe. Optical, ultraviolet and infrared observations of X-ray binaries. In Compact stellar X-ray sources, pages 215–265. Cambridge, UK: Cambridge University, 2006.

C. Chevalier, S. A. Ilovaisky, J. van Paradijs, H. Pedersen, and M. van der Klis. Optical studies of transient low-mass X-ray binaries in quiescence. I - Centaurus X-4: Orbital period, light curve, spectrum and models for the system. A&A , 210:114–126, 1989.

A. Claret, J. Diaz-Cordoves, and A. Gimenez. Linear and non-linear limb-darkening coefficients for the photometric bands R I J H K. A&AS, 114:247, 1995.

J. Clarke. Interface Protocol for the Rockwell Scientific AstroCam. Technical report, , 2004.

J. P. Conner, W. D. Evans, and R. D. Belian. The Recent Appearance of a New X-Ray Source in the Southern Sky. ApJL , 157:L157, 1969.

J. M. Cordes and T. J. W. Lazio. NE2001.I. A New Model for the Galactic Distribution of Free Electrons and its Fluctuations. ArXiv Astrophysics e-prints, 2002.

J. M. Cordes, P. C. C. Freire, D. R. Lorimer, F. Camilo, D. J. Champion, D. J. Nice, R. Ramachandran, J. W. T. Hessels, W. Vlemmings, J. van Leeuwen, S. M. Ransom, N. D. R. Bhat, Z. Arzoumanian, M. A. McLaughlin, V. M. Kaspi, L. Kasian, J. S. Deneva, B. Reid, S. Chatterjee, J. L. Han, D. C. Backer, I. H. Stairs, A. A. Deshpande, and C.-A. Faucher-Giguère. Arecibo Pulsar Survey Using ALFA. I. Survey Strategy and First Discoveries. ApJ , 637:446–455, 2006.

A. P. Cowley, D. Crampton, and J. B. Hutchings. GX 339-4 - Black hole or neutron star X-ray binary? AJ , 93:195–199, 1987.

M. C. Cushing, W. D. Vacca, and J. T. Rayner. Spextool: A Spectral Extraction Package for SpeX, a 0.8-5.5 Micron Cross-Dispersed Spectrograph. PASP , 116:362–376, 2004.

M. C. Cushing, J. T. Rayner, and W. D. Vacca. An Infrared Spectroscopic Sequence of M, L, and T Dwarfs. ApJ , 623:1115–1140, 2005.

J. Dabringhausen, P. Kroupa, J. Pflamm-Altenburg, and S. Mieske. Low-mass X-Ray Binaries Indicate a Top-heavy Stellar Initial Mass Function in Ultracompact Dwarf Galaxies. ApJ , 747:72, 2012.

P. D'Avanzo, S. Campana, J. Casares, G. L. Israel, S. Covino, P. A. Charles, and L. Stella. Doppler tomography of the transient X-ray binary Centaurus X-4 in quiescence. A&A , 444:905–912, 2005.

P. B. Demorest, T. Pennucci, S. M. Ransom, M. S. E. Roberts, and J. W. T. Hessels. A two-solar-mass neutron star measured using Shapiro delay. Nature , 467:1081–1083, 2010.

A. I. Diaz, E. Terlevich, and R. Terlevich. Near-IR features in late type stars - Their relation with stellar atmosphere parameters. MNRAS, 239:325–345, 1989.

C. Done and M. Gierliński. Scaling variability from stellar to supermassive black holes. MNRAS, 364:208–216, 2005.

P. P. Eggleton. Approximations to the radii of Roche lobes. ApJ , 268:368, 1983.

H. Falcke and P. L. Biermann. The jet-disk symbiosis. I. Radio to X-ray emission models for quasars. A&A , 293:665–682, 1995.

H. Falcke, E. Körding, and S. Markoff. A scheme to unify low-power accreting black holes. Jet-dominated accretion flows and the radio/X-ray correlation. A&A , 414:895–903, 2004.

W. M. Farr, N. Sravan, A. Cantrell, L. Kreidberg, C. D. Bailyn, I. Mandel, and V. Kalogera. The Mass Distribution of Stellar-mass Black Holes. ApJ , 741:103, 2011.

R. P. Fender, E. Gallo, and D. Russell. No evidence for black hole spin powering of jets in X-ray binaries. MNRAS, 406:1425–1434, 2010.

J. B. Fitzgerald and J. A. Orosz. Extensive Optical Studies of the Black Hole Binary XTE J1118+480. In American Astronomical Society Meeting Abstracts #202, volume 202 of Bulletin of the American Astronomical Society, page 601, 2003.

N. M. Förster Schreiber. Moderate-Resolution Near-Infrared Spectroscopy of Cool Stars: A New K-Band Library. AJ , 120:2089–2100, 2000.

A. M. Fowler and I. Gatley. Demonstration of an algorithm for read-noise reduction in infrared arrays. ApJL , 353:L33, 1990.

A. M. Fowler and I. Gatley. Noise reduction strategy for hybrid IR focal-plane arrays. In T. S. J. Jayadev, editor, Society of Photo-Optical Instrumentation Engineers (SPIE) Conference Series, volume 1541 of Society of Photo-Optical Instrumentation Engineers (SPIE) Conference Series, pages 127–133, 1991.

T. Fragos, B. Willems, V. Kalogera, N. Ivanova, G. Rockefeller, C. L. Fryer, and P. A. Young. Understanding Compact Object Formation and Natal Kicks. II. The Case of XTE J1118 + 480. ApJ , 697:1057–1070, 2009.

J. Frank, A. R. King, and D. J. Raine. Accretion Power in Astrophysics. Cambridge : Cambridge University Press, 2nd edition, 1992.

P. C. C. Freire. Eccentric Binary Millisecond Pulsars. ArXiv e-prints, 2009.

P. C. C. Freire, C. G. Bassa, N. Wex, I. H. Stairs, D. J. Champion, S. M. Ransom, P. Lazarus, V. M. Kaspi, J. W. T. Hessels, M. Kramer, J. M. Cordes, J. P. W. Verbiest, P. Podsiadlowski, D. J. Nice, J. S. Deneva, D. R. Lorimer, B. W. Stappers, M. A. McLaughlin, and F. Camilo. On the nature and evolution of the unique binary pulsar J1903+0327. MNRAS, 412:2763–2780, 2011.

J. L. Friedman and J. R. Ipser. On the maximum mass of a uniformly rotating neutron star. ApJ , 314:594–597, 1987.

J. L. Friedman, L. Parker, and J. R. Ipser. Rapidly rotating neutron star models. ApJ , 304: 115–139, 1986.

C. S. Froning and E. L. Robinson. Near-Infrared Light Curves of the Black Hole Binary A0620-00. AJ , 121:2212–2218, 2001.

C. S. Froning, E. L. Robinson, W. F. Welsh, and J. H. Wood. The Quiescent Accretion Disk in IP Pegasi at Near-Infrared Wavelengths. ApJ , 523:399–408, 1999.

C. S. Froning, E. L. Robinson, and M. A. Bitner. Near-Infrared Spectra of the Black Hole X-Ray Binary A0620-00. ApJ , 663:1215–1224, 2007.

F. Frontera, A. A. Zdziarski, L. Amati, J. Mikołajewska, T. Belloni, S. Del Sordo, F. Haardt, E. Kuulkers, N. Masetti, M. Orlandini, E. Palazzi, A. N. Parmar, R. A. Remillard, A. Santangelo, and L. Stella. A Measurement of the Broadband Spectrum of XTE J1118+480 with BeppoSAX and Its Astrophysical Implications. ApJ , 561:1006–1015, 2001.

C. L. Fryer and V. Kalogera. Theoretical Black Hole Mass Distributions. ApJ , 554:548–560, 2001.

M. R. Garcia. The possible X ray triple 4U2129+47 (=V1727 Cygni). In J. Hunt and B. Battrick, editors, Two Topics in X-Ray Astronomy, Volume 1: X Ray Binaries. Volume 2: AGN and the X Ray Background, volume 296 of ESA Special Publication, pages 151–156, 1989.

M. L. Garcia-Vargas, M. Molla, and A. Bressan. Calcium triplet synthesis. A&AS, 130: 513–526, 1998.

T. N. Gautier, III, U. Fink, H. P. Larson, and R. I. Thompson. A lower limit on the surface C-12/C-13 ratio in Alpha Orionis. ApJ , 205:841–847, 1976.

D. M. Gelino and T. E. Harrison. GRO J0422+32: The Lowest Mass Black Hole? ApJ , 599:1254–1259, 2003.

D. M. Gelino, T. E. Harrison, and J. A. Orosz. A Multiwavelength, Multiepoch Study of the Soft X-Ray Transient Prototype, V616 Monocerotis (A0620-00). AJ , 122:2668–2678, 2001.

D. M. Gelino, Ş. Balman, Ü. Kızıloğlu, A. Yılmaz, E. Kalemci, and J. A. Tomsick. The Inclination Angle and Mass of the Black Hole in XTE J1118+480. ApJ , 642:438–442, 2006.

D. R. Gies and C. T. Bolton. The optical spectrum of HDE 226868 = Cygnus X-1. II Spectrophotometry and mass estimates. ApJ , 304:371–393, 1986.

N. Ginestet, J. M. Carquillat, M. Jaschek, and C. Jaschek. Spectral classifications in the near infrared of stars with composite spectra. I. The study of MK standards. A&AS, 108: 359–375, 1994.

J. I. González Hernández, R. Rebolo, G. Israelian, J. Casares, K. Maeda, P. Bonifacio, and P. Molaro. Chemical Abundances in the Secondary Star of the Neutron Star Binary Centaurus X-4. ApJ , 630:495–505, 2005.

J. I. González Hernández, R. Rebolo, G. Israelian, A. V. Filippenko, R. Chornock, N. Tominaga, H. Umeda, and K. Nomoto. Chemical Abundances of the Secondary Star in the Black Hole X-Ray Binary XTE J1118+480. ApJ , 679:732–745, 2008.

A. Gopakumar, M. Bagchi, and A. Ray. Ruling out Kozai resonance in highly eccentric galactic binary millisecond pulsar PSR J1903+0327. MNRAS, 399:L123–L127, 2009.

D. F. Gray. The observation and analysis of stellar photospheres. New York, Wiley-Interscience, 1976.

J. M. Hameury, A. R. King, and J. P. Lasota. A model for soft X-ray transients. A&A , 162:71–79, 1986.

E. Harlaftis, S. Collier, K. Horne, and A. V. Filippenko. Keck observations of the black-hole candidate GRO J0422+32. A&A , 341:491–498, 1999.

T. E. Harrison, B. J. McNamara, P. Szkody, and R. L. Gilliland. The Spectroscopic and Astrometric Parallaxes of Three Dwarf Novae: The Nature of the Secondary Stars of U Geminorum, SS Aurigae, and SS Cygni. AJ , 120:2649–2660, 2000.

T. E. Harrison, H. L. Osborne, and S. B. Howell. The Detection of ^{13}CO and Other Apparent Abundance Anomalies in the Secondary Stars of Long-Period Cataclysmic Variables. AJ , 127:3493–3507, 2004.

C. A. Haswell, E. L. Robinson, K. Horne, R. F. Stiening, and T. M. C. Abbott. On the mass of the compact object in the black hole binary A0620-00. ApJ , 411:802–812, 1993.

C. A. Haswell, R. I. Hynes, A. R. King, and K. Schenker. The ultraviolet line spectrum of the soft X-ray transient XTE J1118+480: a CNO-processed core exposed. MNRAS, 332: 928–932, 2002.

R. W. Hilditch. An Introduction to Close Binary Stars. Cambridge, UK: Cambridge University Press, 2001.

L. K. Hunt, F. Mannucci, L. Testi, S. Migliorini, R. M. Stanga, C. Baffa, F. Lisi, and L. Vanzi. Northern JHK Standard Stars for Array Detectors. AJ , 115:2594–2603, 1998.

R. I. Hynes. An optimal extraction of spatially blended spectra. A&A , 382:752–757, 2002.

R. I. Hynes. Multiwavelength Observations of Accretion in Low-Mass X-ray Binary Systems. ArXiv e-prints, 2010.

R. I. Hynes. Observations of Low Mass X-ray Transients in Outburst. PhD thesis, The Open University, 1999.

R. I. Hynes, E. L. Robinson, and M. Bitner. Observational Constraints on Cool Disk Material in Quiescent Black Hole Binaries. ApJ , 630:405–412, 2005.

R. I. Hynes, C. K. Bradley, M. Rupen, E. Gallo, R. P. Fender, J. Casares, and C. Zurita. The quiescent spectral energy distribution of V404 Cyg. MNRAS, 399:2239–2248, 2009.

T. P. Idiart, F. Thevenin, and J. A. de Freitas Pacheco. The Infrared Ca II Triplet as a Metallicity Indicator of Stellar Populations. AJ , 113:1066, 1997.

T. Johannsen. Constraints on the size of extra dimensions from the orbital evolution of the black-hole X-ray binary XTE J1118+480. A&A , 507:617–620, 2009.

J. E. Jones, D. M. Alloin, and B. J. T. Jones. The infrared CA II triplet - A luminosity indicator for stellar population synthesis. ApJ , 283:457–465, 1984.

J. Khargharia, C. S. Froning, and E. L. Robinson. Near-infrared Spectroscopy of Low-mass X-ray Binaries: Accretion Disk Contamination and Compact Object Mass Determination in V404 Cyg and Cen X-4. ApJ , 716:1105–1117, 2010.

J. Khargharia, J. T. Stocke, C. S. Froning, A. Gopakumar, and B. C. Joshi. PSR J1903+0327: A Unique Millisecond Pulsar with a Main-sequence Companion Star. ApJ , 744:183, 2012.

T. S. Khruzina, A. M. Cherepashchuk, D. V. Bisikalo, A. A. Boyarchuk, and O. A. Kuznetsov. Interpretation of the light curves of "quiescent" X-ray novae in a model with a noncollisional interaction between the flow and disk. The XTE J1118+480 system. Astronomy Reports, 49:79–88, 2005.

A. R. King. The evolutionary status of the black hole candidate V404 Cygni. MNRAS, 260: L5, 1993.

J. D. Kirkpatrick, D. M. Kelly, G. H. Rieke, J. Liebert, F. Allard, and R. Wehrse. M dwarf spectra from 0.6 to 1.5 micron - A spectral sequence, model atmosphere fitting, and the temperature scale. ApJ , 402:643–654, 1993.

S. G. Kleinmann and D. N. B. Hall. Spectra of late-type standard stars in the region 2.0-2.5 microns. ApJS , 62:501–517, 1986.

C. Koen, D. Kilkenny, F. van Wyk, and F. Marang. UBV(RI)$_C$ JHK observations of Hipparcos-selected nearby stars. MNRAS, 403:1949–1968, 2010.

Y. Kozai. Secular perturbations of asteroids with high inclination and eccentricity. AJ , 67: 591, 1962.

M. Kramer, I. H. Stairs, R. N. Manchester, M. A. McLaughlin, A. G. Lyne, R. D. Ferdman, M. Burgay, D. R. Lorimer, A. Possenti, N. D'Amico, J. M. Sarkissian, G. B. Hobbs, J. E. Reynolds, P. C. C. Freire, and F. Camilo. Tests of General Relativity from Timing the Double Pulsar. Science, 314:97–102, 2006.

R. W. Leach and F. J. Low. CCD and IR array controllers. In Society of Photo-Optical Instrumentation Engineers (SPIE) Conference Series, volume 4008, pages 337–343, 2000.

W. H. G. Lewin and M. van der Klis. Compact stellar X-ray sources. Cambridge : Cambridge University Press, 1st edition, 2006.

W. H. G. Lewin, J. van Paradijs, and R. E. Taam. X-Ray Bursts. Sp Sci Rev, 62:223–389, 1993.

W. H. G. Lewin, J. van Paradijs, and E. P. J. van den Heuvel, editors. X-ray binaries, 1995.

J. Lin, M. A. Nowak, and D. Chakrabarty. A Further Drop into Quiescence by the Eclipsing Neutron Star 4U 2129+47. ApJ , 706:1069–1077, 2009.

J. Lin, S. Rappaport, P. Podsiadlowski, L. Nelson, B. Paxton, and P. Todorov. LMXB and IMXB Evolution: I. The Binary Radio Pulsar PSR J1614-2230. ApJ , 732:70, 2011.

X.-W. Liu and X.-D. Li. A Fallback Disk Accretion Involved Formation Channel to PSR J1903+0327. ApJ , 692:723–728, 2009.

D. R. Lorimer. Binary and Millisecond Pulsars at the New Millennium. Living Reviews in Relativity, 4:5, 2001.

L. B. Lucy. Gravity-Darkening for Stars with Convective Envelopes. Z. Astrophys., 65:89, 1967.

D. Maitra, S. Markoff, C. Brocksopp, M. Noble, M. Nowak, and J. Wilms. Constraining jet/disc geometry and radiative processes in stellar black holes XTE J1118+480 and GX 339-4. MNRAS, 398:1638–1650, 2009.

F. Makino. GS 2023+338. IAU Circulars, 4782:1, 1989.

S. V. Mallik. The CA II triplet lines in cool stars. A&AS, 103:279–291, 1994.

S. Markoff, M. Nowak, A. Young, H. L. Marshall, C. R. Canizares, A. Peck, M. Krips, G. Petitpas, R. Schödel, G. C. Bower, P. Chandra, A. Ray, M. Muno, S. Gallagher, S. Hornstein, and C. C. Cheung. Results from an Extensive Simultaneous Broadband Campaign on the Underluminous Active Nucleus M81*: Further Evidence for Mass-scaling Accretion in Black Holes. ApJ , 681:905–924, 2008.

S. Markoff, M. A. Nowak, J. Nip, F. K. Baganoff, C. S. Froning, A. G. Cantrell, T. J. Maccarone, and E. Gallo. Sgr A*: Quiescent But Not Atypical – A Comparison With A0620-00. In American Astronomical Society Meeting Abstracts, volume 219, page 409.05, 2012.

M. Matsuoka, H. Inoue, K. Koyama, K. Makishima, T. Murakami, M. Oda, Y. Ogawara, T. Ohashi, N. Shibazaki, Y. Tanaka, I. Kondo, S. Hayakawa, H. Kunieda, F. Makino, K. Masai, F. Nagase, Y. Tawara, S. Miyamoto, H. Tsunemi, and K. Yamashita. Discovery of a large X-ray burst from an X-ray nova, Centaurus X-4. ApJL , 240:L137–L141, 1980.

J. E. McClintock and R. A. Remillard. The black hole binary A0620-00. ApJ , 308:110–122, 1986.

J. E. McClintock and R. A. Remillard. The X-ray nova Centaurus X-4 - Comparisons with A0620 - 00. ApJ , 350:386–394, 1990.

J. E. McClintock, M. R. Garcia, N. Caldwell, E. E. Falco, P. M. Garnavich, and P. Zhao. A Black Hole Greater Than 6 M_{solar} in the X-Ray Nova XTE J1118+480. ApJL , 551: L147–L150, 2001.

J. E. McClintock, R. Shafee, R. Narayan, R. A. Remillard, S. W. Davis, and L.-X. Li. The Spin of the Near-Extreme Kerr Black Hole GRS 1915+105. ApJ , 652:518–539, 2006.

J. E. McClintock, R. Narayan, S. W. Davis, L. Gou, A. Kulkarni, J. A. Orosz, R. F. Penna, R. A. Remillard, and J. F. Steiner. Measuring the spins of accreting black holes. Classical and Quantum Gravity, 28(11):114009, 2011.

I. S. McLean. Infrared Instrumentation. In A. Mampaso, M. Prieto, & F. Sanchez, editor, Infrared Astronomy, page 335, 1993.

I. S. McLean. Electronic Imaging in Astronomy: Detectors and Instrumentation. Praxis Publishing, 2008.

C. H. F. Melo, L. Pasquini, and J. R. De Medeiros. Accurate Vsini measurements in M 67: The angular momentum evolution of 1.2 M_{sun} stars. A&A , 375:851–862, 2001.

A. Merloni, S. Heinz, and T. di Matteo. A Fundamental Plane of black hole activity. MNRAS, 345:1057–1076, 2003.

M. R. Meyer, S. Edwards, K. H. Hinkle, and S. E. Strom. Near-Infrared Classification Spectroscopy: H-Band Spectra of Fundamental MK Standards. ApJ , 508:397–409, 1998.

J. Mikołajewska, A. Rutkowski, D. R. Gonçalves, and A. Szostek. The first near-infrared detection of XTEJ1118 + 480 in quiescence. MNRAS, 362:L13–L15, 2005.

J. C. A. Miller-Jones, P. G. Jonker, V. Dhawan, W. Brisken, M. P. Rupen, G. Nelemans, and E. Gallo. The First Accurate Parallax Distance to a Black Hole. ApJL , 706:L230–L234, 2009.

I. F. Mirabel and L. F. Rodríguez. Sources of Relativistic Jets in the Galaxy. ARAA , 37: 409–443, 1999.

R. Narayan and J. E. McClintock. Observational evidence for a correlation between jet power and black hole spin. MNRAS, 419:L69–L73, 2012.

G. Nelemans and E. P. J. van den Heuvel. The formation of black hole low-mass X-ray binaries: Through case B or case C mass transfer? A&A , 376:950–954, 2001.

D. J. Nice, I. H. Stairs, and L. E. Kasian. Masses of Neutron Stars in Binary Pulsar Systems. In 40 Years of Pulsars: Millisecond Pulsars, Magnetars and More, volume 983 of American Institute of Physics Conference Series, pages 453–458, 2008.

D. E. Osterbrock, J. P. Fulbright, A. R. Martel, M. J. Keane, S. C. Trager, and G. Basri. Night-Sky High-Resolution Spectral Atlas of OH and O2 Emission Lines for Echelle Spectrograph Wavelength Calibration. PASP , 108:277, 1996.

F. Özel, D. Psaltis, R. Narayan, and J. E. McClintock. The Black Hole Mass Distribution in the Galaxy. ApJ , 725:1918–1927, 2010.

E. S. Phinney. Pulsars as Probes of Newtonian Dynamical Systems. Royal Society of London Philosophical Transactions Series A, 341:39–75, 1992.

P. Podsiadlowski. Irradiation-driven mass transfer low-mass X-ray binaries. Nature , 350: 136–138, 1991.

S. Portegies Zwart, E. P. J. van den Heuvel, J. van Leeuwen, and G. Nelemans. The Formation of the Eccentric-orbit Millisecond Pulsar J1903+0327 and the Origin of Single Millisecond Pulsars. ApJ , 734:55, 2011.

K. A. Postnov and A. M. Cherepashchuk. Masses of Stellar Black Holes and Testing Theories of Gravitation. Astronomy Reports, 47:989–999, 2003.

D. Psaltis. Accreting neutron stars and black holes: a decade of discoveries, pages 1–38. Cambridge : Cambridge University Press, 2006.

D. Queloz, S. Allain, J.-C. Mermilliod, J. Bouvier, and M. Mayor. The rotational velocity of low-mass stars in the Pleiades cluster. A&A , 335:183–198, 1998.

J. T. Rayner, D. W. Toomey, P. M. Onaka, A. J. Denault, W. E. Stahlberger, W. D. Vacca, M. C. Cushing, and S. Wang. SpeX: A Medium-Resolution 0.8-5.5 Micron Spectrograph and Imager for the NASA Infrared Telescope Facility. PASP , 115:362–382, 2003.

J. T. Rayner, M. C. Cushing, and W. D. Vacca. The Infrared Telescope Facility (IRTF) Spectral Library: Cool Stars. ApJS , 185:289–432, 2009.

G. H. Reike. Infrared Detector Arrays for Astronomy. ARAA , 45(77-115), 2007.

M. Revnivtsev, R. Sunyaev, and K. Borozdin. Discovery of a 0.08 Hz QPO in the power spectrum of black hole candidate XTE J1118+480. A&A , 361:L37–L39, 2000.

M. T. Reynolds, P. J. Callanan, and A. V. Filippenko. Keck infrared observations of GRO J0422+32 in quiescence. MNRAS, 374:657–663, 2007.

M. T. Reynolds, P. J. Callanan, E. L. Robinson, and C. S. Froning. Infrared contamination in Galactic X-ray novae. MNRAS, 387:788–796, 2008.

C. E. Rhoades and R. Ruffini. Maximum Mass of a Neutron Star. Physical Review Letters, 32:324–327, 1974.

Rockwell Scientific. Hawaii-1RG Technical Documentation. Technical report, Rockwell Scientific Company, 2002.

D. Sanwal, E. L. Robinson, E. Zhang, C. Colome, P. M. Harvey, T. F. Ramseyer, C. Hellier, and J. H. Wood. An Upper Limit to the Mass of the Black Hole in V404 Cygni. ApJ , 460:437, 1996.

M. J. Sarna. Gravity-darkening for stars with a Roche lobe filling convective envelopes in close binary systems. A&A , 224:98–100, 1989.

R. Shafee, J. E. McClintock, R. Narayan, S. W. Davis, L.-X. Li, and R. A. Remillard. Estimating the Spin of Stellar-Mass Black Holes by Spectral Fitting of the X-Ray Continuum. ApJL , 636:L113–L116, 2006.

T. Shahbaz, T. Naylor, and P. A. Charles. An Ellipsoidal Study of Centaurus-X-4. MNRAS, 265:655, 1993.

T. Shahbaz, F. A. Ringwald, J. C. Bunn, T. Naylor, P. A. Charles, and J. Casares. The mass of the black hole in V404 Cygni. MNRAS, 271:L10–L14, 1994.

T. Shahbaz, R. Bandyopadhyay, P. A. Charles, and T. Naylor. Infrared spectroscopy of V404 Cygni: limits on the accretion disc contamination. MNRAS, 282:977–981, 1996.

G. Smith and J. J. Drake. The wings of the calcium infrared triplet lines in solar-type stars. A&A , 181:103–111, 1987.

I. H. Stairs. Testing General Relativity with Pulsar Timing. Living Reviews in Relativity, 6:5, 2003.

I. H. Stairs. Pulsars in Binary Systems: Probing Binary Stellar Evolution and General Relativity. Science, 304:547–552, 2004.

J. F. Steiner, J. E. McClintock, R. A. Remillard, R. Narayan, and L. Gou. Measuring Black Hole Spin Via the X-Ray Continuum-Fitting Method: Beyond the Thermal Dominant State. ApJL , 701:L83–L86, 2009.

P. Szkody. Infrared photometry of dwarf novae and possibly related objects. ApJ , 217: 140–150, 1977.

J.-L. Tassoul. Stellar Rotation. Cambridge : Cambridge University Press, 2007.

T. M. Tauris and E. P. J. van den Heuvel. Formation and evolution of compact stellar X-ray sources. In Compact stellar X-ray sources, pages 623–665. Cambridge, UK: Cambridge University, 2006.

A. Tchekhovskoy, R. Narayan, and J. C. McKinney. Efficient generation of jets from magnetically arrested accretion on a rapidly spinning black hole. MNRAS, 418:L79–L83, 2011.

J. Tonry and M. Davis. A survey of galaxy redshifts. I - Data reduction techniques. AJ , 84: 1511–1525, 1979.

M. A. P. Torres, J. Casares, I. G. Martínez-Pais, and P. A. Charles. Rotational broadening and Doppler tomography of the quiescent X-ray nova Centaurus X-4. MNRAS, 334:233–240, 2002.

M. A. P. Torres, P. J. Callanan, M. R. Garcia, P. Zhao, S. Laycock, and A. K. H. Kong. MMT Observations of the Black Hole Candidate XTE J1118+480 near and in Quiescence. ApJ , 612:1026–1033, 2004.

M. Uemura, T. Kato, K. Matsumoto, H. Yamaoka, K. Takamizawa, Y. Sano, K. Haseda, L. M. Cook, D. Buczynski, and G. Masi. Discovery and Photometric Observation of the Optical Counterpart of a Possible Galactic Halo X-Ray Transient, XTE J1118+480. PASJ, 52:L15–L20, 2000.

W. D. Vacca, M. C. Cushing, and J. T. Rayner. A Method of Correcting Near-Infrared Spectra for Telluric Absorption. PASP , 115:389–409, 2003.

J. van Paradijs and J. E. McClintock. Optical and ultraviolet observations of X-ray binaries. In W. H. G. Lewin, J. van Paradijs, & E. P. J. van den Heuvel, editor, X-ray Binaries, pages 58–125, 1995.

J. van Paradijs, F. Verbunt, R. A. Shafer, and K. A. Arnaud. Soft X-ray transients in quiescence - Observations of AQL X-1 and CEN X-4. A&A , 182:47–50, 1987.

F. Verbunt and E. P. J. van den Heuvel. Formation and evolution of neutron stars and black holes in binaries. In W. H. G. Lewin, J. van Paradijs, & E. P. J. van den Heuvel, editor, X-ray Binaries, pages 457–494, 1995.

H. von Zeipel. The radiative equilibrium of a rotating system of gaseous masses. MNRAS, 84:665–683, 1924.

R. A. Wade and K. Horne. The radial velocity curve and peculiar TiO distribution of the red secondary star in Z Chamaeleontis. ApJ , 324:411–430, 1988.

R. M. Wagner, S. G. Starrfield, A. Cassatella, G. M. Hurst, M. Mobberley, and B. G. Marsden. V404 Cygni = GS 2023+338. IAU Circulars, 4783:1, 1989.

R. M. Wagner, T. J. Kreidl, S. B. Howell, and S. G. Starrfield. Periodic photometric variability of the black hole binary V404 Cygni. ApJL , 401:L97–L100, 1992.

R. M. Wagner, C. B. Foltz, T. Shahbaz, J. Casares, P. A. Charles, S. G. Starrfield, and P. Hewett. The Halo Black Hole X-Ray Transient XTE J1118+480. ApJ , 556:42–46, 2001.

L. Wallace and K. Hinkle. Medium-Resolution Spectra of Normal Stars in the K Band. ApJS , 111:445, 1997.

L. Wallace, M. R. Meyer, K. Hinkle, and S. Edwards. Near-Infrared Classification Spectroscopy: J-Band Spectra of Fundamental MK Standards. ApJ , 535:325–337, 2000.

N. Wex. A timing formula for main-sequence star binary pulsars. MNRAS, 298:67–77, 1998.

S. Wolff and T. Simon. The Angular Momentum of Main Sequence Stars and Its Relation to Stellar Activity. PASP , 109:759–775, 1997.

K. S. Wood, P. S. Ray, R. M. Bandyopadhyay, M. T. Wolff, G. Fritz, P. Hertz, M. P. Kowalski, M. N. Lovellette, D. Yentis, E. D. Bloom, B. Giebels, G. Godfrey, K. Reilly, P. Saz Parkinson, G. Shabad, and J. Scargle. USA Experiment and RXTE Observations of a Variable Low-Frequency Quasi-periodic Oscillation in XTE J1118+480. ApJL , 544: L45–L48, 2000.

G. Worthey and H.-c. Lee. An Empirical UBV RI JHK Color-Temperature Calibration for Stars. ApJS , 193:1, 2011.

J. Wren, C. Akerlof, R. Balsano, J. Bloch, K. Borozdin, D. Casperson, G. Gisler, R. Kehoe, B. C. Lee, S. Marshall, T. McKay, W. Priedhorsky, E. Rykoff, D. Smith, S. Trudolyubov, and W. T. Vestrand. Observations of the Optical Counterpart to XTE J1118+480 during Outburst by the Robotic Optical Transient Search Experiment I Telescope. ApJL , 557: L97–L100, 2001.

F. Yuan, W. Cui, and R. Narayan. An Accretion-Jet Model for Black Hole Binaries: Interpreting the Spectral and Timing Features of XTE J1118+480. ApJ , 620:905–914, 2005.

J. A. Zensus. Parsec-Scale Jets in Extragalactic Radio Sources. ARAA , 35:607–636, 1997.

E.-H. Zhang, E. L. Robinson, and R. E. Nather. The eclipses of cataclysmic variables. I - HT Cassiopeiae. ApJ , 305:740–758, 1986.

C. Zurita, J. Casares, T. Shahbaz, R. M. Wagner, C. B. Foltz, P. Rodríguez-Gil, R. I. Hynes, P. A. Charles, E. Ryan, G. Schwarz, and S. G. Starrfield. Detection of superhumps in XTE J1118+480 approaching quiescence. MNRAS, 333:791–799, 2002.